Comenius University in Bratislava
Faculty of Mathematics, Physics and Informatics

Tensor Networks: Phase Transition Phenomena on Hyperbolic and Fractal Geometries

PhD Thesis

Mgr. Jozef Genzor

2016

Comenius University in Bratislava

Faculty of Mathematics, Physics and Informatics

Tensor Networks:
Phase Transition Phenomena on Hyperbolic and Fractal Geometries

PhD Thesis

Study programme:	Theoretical Physics and Mathematical Physics
Study field:	4.1.2 General Physics and Mathematical Physics
Educational institution:	Research Center for Quantum Information Institute of Physics, Slovak Academy of Sciences
Supervisor:	Mgr. Andrej Gendiar, PhD.

Bratislava 2016 Mgr. Jozef Genzor

Comenius University in Bratislava
Faculty of Mathematics, Physics and Informatics

THESIS ASSIGNMENT

Name and Surname:	Mgr. Jozef Genzor
Study programme:	General Physics and Mathematical Physics (Single degree study, Ph.D. III. deg., full time form)
Field of Study:	General Physics And Mathematical Physics
Type of Thesis:	Dissertation thesis
Language of Thesis:	English
Secondary language:	Slovak

Title: Tensor Networks: Phase Transition Phenomena on Hyperbolic and Fractal Geometries

Literature:
[1] R. J. Baxter, Exactly Solved Models in Statistical Mechanics (Academic Press, London, 1982)
[2] S. R. White, Phys. Rev. Lett. 69, 2863 (1992)
[3] T. Nishino and K. Okunishi, J. Phys. Soc. Jpn. 65, 891 (1996)
[4] U. Schollwoeck, Rev. Mod. Phys. 77, 259 (2005)
[5] Z. Y. Xie, et al., Phys. Rev. B 86, 045139 (2012)
[6] R. Orus, Annals of Physics, 349, 117-158 (2014), arXiv:1306.2164

Aim: Development of tensor-network-based algorithms in order to classify phase transitions in interacting spin systems on non-Euclidean geometries.

Annotation: A fast-evolving progress of tensor network studies has been opening promising perspectives in treatment of non-trivial quantum and classical strongly interacting systems in higher dimensions. First, the solid-state physics and quantum information theory have been influenced. However, recent achievements in the tensor networks have been successfully applied to quantum chemistry and high-energy physics. Nowadays, there is a challenging task to attack systems seemingly hard feasible, such as neural networks and even the general theory of relativity, which is the current study devoted to.
* The first aim is to understand the two types of Tensor Product State Ansatz: Corner Transfer Matrix Renormalization Group and Higher-Order Tensor Renormalization Group by coding own algorithms in C++ programming language.
* The second aim is to generalize the two algorithms to study spin Hamiltonians exhibiting such network structures of spin interactions, which enable us to treat both the negatively curved geometries and the fractal structures.
* The third aim is to classify the first/second order phase transitions of the systems on infinitely large networks of interacting spins.

Keywords: Phase Transitions and Universality Classification, Quantum and Classical Lattice Systems, Tensor Networks, Matrix Product States, Density Matrix Renormalization Group, Corner Transfer Matrix, Singular Value Decomposition

Tutor:	Mgr. Andrej Gendiar, PhD.
Department:	FMFI.KTFDF - Department of Theoretical Physics and Didactics of Physics

Comenius University in Bratislava
Faculty of Mathematics, Physics and Informatics

Head of department: doc. RNDr. Tomáš Blažek, PhD.

Assigned: 01.09.2012

Approved: 18.07.2012 prof. RNDr. Melánia Babincová, CSc.
Guarantor of Study Programme

.....
Student

.....
Tutor

Univerzita Komenského v Bratislave
Fakulta matematiky, fyziky a informatiky

51832218

ZADANIE ZÁVEREČNEJ PRÁCE

Meno a priezvisko študenta: Mgr. Jozef Genzor
Študijný program: všeobecná fyzika a matematická fyzika (Jednoodborové štúdium, doktorandské III. st., denná forma)
Študijný odbor: všeobecná fyzika a matematická fyzika
Typ záverečnej práce: dizertačná
Jazyk záverečnej práce: anglický
Sekundárny jazyk: slovenský

Názov: Tensor Networks: Phase Transition Phenomena on Hyperbolic and Fractal Geometries
Tenzorove siete: Fázove prechody na hyperbolických a fraktálnych geometriách

Literatúra:
[1] R. J. Baxter, Exactly Solved Models in Statistical Mechanics (Academic Press, London, 1982)
[2] S. R. White, Phys. Rev. Lett. 69, 2863 (1992)
[3] T. Nishino and K. Okunishi, J. Phys. Soc. Jpn. 65, 891 (1996)
[4] U. Schollwoeck, Rev. Mod. Phys. 77, 259 (2005)
[5] Z. Y. Xie, et al., Phys. Rev. B 86, 045139 (2012)
[6] R. Orus, Annals of Physics, 349, 117-158 (2014), arXiv:1306.2164

Cieľ: Vývoj algoritmov zaožených na princípoch tenzorových sietí za účelom klasifikácie fázových prechodov v interagujúcich spinových systémov na neeuklidovských geometriách.

Anotácia: Rýchly progres štúdií tenzorových sietí otvára nové perspektívy, akým spôsobom je možné analyzovať netriviálne kvantové a klasické silnointeragujúce systémy vo vyšších dimenziách. Ako prvé boli tenzorové siete aplikované do oblasti fyziky tuhých látok a teórie kvantovej informácie. Avšak nedávne úspešné aplikácie tenzorových sietí začali ovplyvňovať nové oblasti, akými sú kvantová chémia a časticová fyzika vysokých energií. V súčasnosti sa otvárajú ďalšie výzvy, ako popisovať zdanlivo neriešiteľné systémy neurónových sietí či dokonca problémy vo všeobecnej teórii relativity, ktorej sa bude venovať táto štúdia.
* Prvým cieľom práce je porozumieť dvom typom tenzorových súčinových stavov, ktorými sú metódy: Corner Transfer Matrix Renormalization Group a Higher-Order Tensor Renormalization Group. Tieto metódy budú následne študentom naprogramované v jazyku C++.
* Druhý cieľ zahŕňa zovšeobecnenie týchto dvoch algoritmov na štúdium spinových hamiltoniánov, ktoré vykazujú také sieťové štruktúry spinových interakcií, ktoré nám umožnia vyšetrovať geometrie so zápornou krivosťou, resp. s fraktálnou štruktúrou.
* Tretím cieľom je klasifikácia fázových prechodov prvého a druhého rádu na nekonečne veľkých sieťach interagujúcich spinov.

Kľúčové slová: Fázové prechody a triedy univerzality, Kvantové a klasické mriežkové systémy, Tenzorové siete, Maticové súčinové stavy, Renormalizačná grupa matíc hustoty, Rohové transfer matice, Dekompozícia na singulárne hodnoty

Univerzita Komenského v Bratislave
Fakulta matematiky, fyziky a informatiky

Školiteľ: Mgr. Andrej Gendiar, PhD.
Katedra: FMFI.KTFDF - Katedra teoretickej fyziky a didaktiky fyziky
Vedúci katedry: doc. RNDr. Tomáš Blažek, PhD.

Spôsob sprístupnenia elektronickej verzie práce:
bez obmedzenia

Dátum zadania: 01.09.2012

Dátum schválenia: 18.07.2012

prof. RNDr. Melánia Babincová, CSc.
garant študijného programu

.....
študent

.....
školiteľ

Abstrakt

Jedným z dôležitých problémov fyziky kondenzovaných látok je pochopiť, čo sa odohráva na pozadí mechanizmov kvantových mnohočasticových systémoch. Keďže existuje iba niekoľko úplných analytických riešení pre tieto systémy, v posledných rokoch bolo navrhnutých niekoľko numerických simulačných metód. Spomedzi nich začínajú byť populárne práve tie algoritmy, ktoré sú založené na princípoch tenzorových sietí, a to najmä vďaka ich aplikovateľnosti na simulácie silno korelovaných systémov. Predkladaná práca sa sústreďuje na zovšeobecnenie takýchto algoritmov, ktoré využívajú algoritmus tenzorových sietí a zároveň sú dostatočne robustné na to, aby popísali kritické javy a fázove prechody multispinových Hamiltoniánov v termodynamickej limite. Na to je však nevyhnutné zaoberať sa so systémami s nekonečne veľkým množstvom interagujúcich častíc. Pre tento účel sme si zvolili dva algoritmy, ktoré sú vhodné pre spinové systémy: Corner Transfer Matrix Renormalization Group a Higher-Order Tensor Renormalization Group. V oboch algoritmoch je základný stav multistavového spinového systému konštruovaný v tvare tenzorového súčinového stavu. Cieľom tejto práce je zovšeobecniť tieto dva algoritmy tak, aby bolo nimi možné počítať termodynamické vlastnosti neeuklidovských geometrií. Osobitne budú analyzované tenzorové súčinové stavy na hyperbolických geometriách so zápornou Gaussovou krivosťou, ale aj na fraktálnych systémoch. Následne budú vykonané rozsiahle numerické simulácie multistavových spinových modelov. Tieto spinové systémy boli zvolené pre ich vhodnosť správne modelovať základné vlastnosti zložitejších systémov, akými sú sociálne správanie, neurónové siete, holografický princíp, vrátane teórie korešpondecie medzi anti-de Sitterovým priestorom a konformnou teóriou poľa v kvantovej gravitácii. Táto práca obsahuje nové postupy aplikácie tenzorových sietí a umožňuje pochopiť fázové prechody a kvantovú previazanosť interagujúcich systémov na neeuklidovských geometriách. Budeme sa preto bližšie venovať nasledujúcim trom tematickým oblastiam. (1) Navrhneme nový termodynamický model sociálneho vplyvu, v ktorom budeme vyšetrovať fázové prechody. (2) Na nekonečnej množine geometrií so zápornou krivosťou klasifikujeme a analyzujeme fázové prechody pomocou voľnej energie. Zároveň bude stanovený vzťah, ktorý dáva do súvisu voľnú energiu a Gaussov polomer krivosti. (3) Navrhneme nový algoritmus založený na tenzorových sieťach, ktorý umožní študovať fázové prechody na nekonečne veľkých fraktálnych štruktúrach.

Kľúčové slová:
Klasifikácia fázových prechodov, Kvantové a klasické spinové mriežkové modely, Tenzorové súčinové stavy, Tenzorové siete, Renormalizácia matice hustoty

Abstract

One of the challenging problems in the condensed matter physics is to understand the quantum many-body systems, especially, physical mechanisms behind. Since there are only a few complete analytical solutions of these systems, several numerical simulation methods have been proposed in recent years. Amongst all of them, the *Tensor Network* algorithms have become increasingly popular in recent years, especially for their adaptability to simulate strongly correlated systems. The current work focuses on the generalization of such Tensor-Network-based algorithms, which are sufficiently robust to describe critical phenomena and phase transitions of multistate spin Hamiltonians in the thermodynamic limit. Therefore, one has to deal with systems of infinitely many interacting spin particles. For this purpose we have chosen two algorithms: the Corner Transfer Matrix Renormalization Group and the Higher-Order Tensor Renormalization Group. The ground state of those multistate spin systems in the thermodynamic equilibrium is constructed in terms of a tensor product state ansatz in both of the algorithms. The main aim of this work is to generalize the idea behind these two algorithms in order to be able to calculate the thermodynamic properties of non-Euclidean geometries. In particular, the tensor product state algorithms of hyperbolic geometries with negative Gaussian curvatures as well as fractal geometries will be theoretically analyzed followed by extensive numerical simulations of the multistate spin models. These spin systems were chosen for their applicability to mimic the intrinsic properties of much more complex systems of social behavior, neural network, the holographic principle, including the correspondence between the anti-de Sitter and conformal field theory in quantum gravity. This work contains novel approaches in tensor networks and opens the door for the understanding of phase transition and entanglement of the interacting systems on the non-Euclidean geometries. The following three topics are investigated by means of the tensor-based algorithms. (1) A new thermodynamic model of social influence is proposed, and its phase transition phenomena are studied. (2) The phase transitions are classified and analyzed by the free energy on an infinite set of the negatively curved geometries. A relation between the free energy and the Gaussian radius of the curvature is conjectured. (3) A unique tensor-based algorithm is proposed, which enables to treat the phase transition on infinitely large fractal structures.

Keywords:
Phase Transition Phenomena, Quantum and Classical Spin Lattice Models,
Tensor Product States, Tensor Networks, Density Matrix Renormalization

Contents

Preface

This work consists of the results and the knowledge gathered during my PhD study. Chapters 1 and 2 introduce all the basic concepts of the phase transitions and tensor networks, respectively, which are heavily used throughout the following chapters. The next chapters 3–5 refer to those concepts, extending and generalizing the theoretical explanations along the way. These three chapters contain my research contributions with novel results which are in sections entitled as Results or Numerical results. They can be read independently of each other. Chapter 4 is specific in that it firstly provides a broader context of an area of application of the statistical-physics tools in the first Section followed by my contribution in the second Section. The reason for such a structure is that the typical reader is not expected to be familiar with the studies of models of social behavior. The content of the chapters 3–5 is based on my work published in Refs. [Serina et al., 2016, Genzor et al., 2015, Genzor et al., 2016].

Here, I would like to thank my supervisor Andrej Gendiar. Thanks for his humor, enthusiasm, and contagious interest in the research, it has always been fun to work together. He taught me everything about CTMRG and encouraged me to write my code. This work would never be possible without his support. The work concerning the fractal lattice was done in collaboration with Tomotoshi Nishino, who came up with an idea of a particular lattice structure in the first place. This collaboration proved to be fruitful and new results will be published soon [Genzor et al.,].

Finally, I am also grateful to my colleagues Yoju Lee and Roman Krcmar for the interesting and helpful discussions. Last but not least, I thank all the people who have supported me in any way during my four-year PhD study.

Introduction

The mathematical treatment of the collective behavior of many-body systems is a highly nontrivial task. Even knowing the underlying laws of microscopic interactions does not guarantee that we can say anything specific about the large-scale behavior of the studied system. The application of the laws might lead to equations which are too complex to be solved. Even worse, the difficulty is usually one level deeper, the Hilbert space is far too large. Imagine having N particles with spin one-half. To describe a state of such a system, it would require knowing 2^N complex amplitudes. For realistic systems (like a piece of a magnet), the number of particles is $N \sim 10^{23}$, which makes the number of basis states larger than the number of all particles in the observable universe.

Fortunately, not all states are created equal. It seems that Nature prefers systems with local interactions (i.e., the nearest or the second nearest neighbors interact only). Consequently, the Hilbert space for realistic systems is significantly reduced. Low-energy states of such systems with gapped Hamiltonians constitute only a tiny corner of all the possible states. Those states satisfy the so-called *area law* for the entanglement entropy, i.e., the entanglement entropy S scales as the surface of a subsystem A, i.e., $S \sim \partial A$ (note that the entropy does not scale with the volume of A).

Therefore, having a tool which efficiently represents that tiny corner of area-law states would be of great advantage. This is probably the main reason why there is such an interest in tensor networks, which can also go beyond and treat systems where the area law does not apply, for instance, at phase transitions. The tensor network formalism aims to represent efficiently the entanglement structure of the system based on its underlying geometry. Tensor networks formalism in connection with the renormalization group allows us to perform numerical calculations in the thermodynamic limit, $N \to \infty$, efficiently.

The underlying topology of the system plays a crucial role in determining its thermodynamic properties. For example, there is no phase transition at nonzero temperature in the one-dimensional Ising model, whereas, there exists a finite critical temperature at higher dimensions. We intend to be greatly interested in study of the phase transition phenomena on non-Euclidean lattices, in particular,

on hyperbolic surface geometries, which have an infinite effective spatial dimension ($d \to \infty$) and a constant negative curvature, as well as on fractal geometries with fractional dimensions $1 < d < 2$. One of the main purposes for researching the phase transition phenomena of spin systems on the non-Euclidean lattice geometries is the fact that these systems are neither exactly solvable nor numerically feasible by standard methods such as Monte Carlo simulations, exact diagonalization, Density Matrix Renormalization Group, Multi-scale Entanglement Renormalization Ansatz, Projected Entangled Pair States, etc. We proposed generalized numerical algorithms based on Tensor Network ideas, which enabled us to solve the spin systems on hyperbolic and fractal lattices of infinite sizes. The algorithms reach a sufficiently high numerical accuracy so that we can classify the phase transitions by evaluating their critical exponents. We have successfully achieved novel results, which have been missing in the theory of solid state physics, statistical mechanics, quantum information, as well as in the anti-de Sitter space of the general theory of relativity. The results of our studies are published in Refs. [Serina et al., 2016, Genzor et al., 2015, Genzor et al., 2016].

This work is structured in the following. Chapter 1 contains basic definitions and notations of the phase transition theory, including the Suzuki-Trotter mapping. The tensor network theory is explained in Chapter 2. This chapter is more of a tutorial, where we tried to include many practical details and comments related to the numerical calculations with the only aim, so as to be useful for students interested in this area of research. The three conceptually very different numerical methods are explained there: infinite Time-Evolving Block Decimation (iTEBD), Corner Transfer Matrix Renormalization Group (CTMRG), and Higher-Order Tensor Renormalization Group (HOTRG). Purely for demonstrative reasons, this chapter also contains my numerical results. These explanations are also complemented by the source codes which can be found in the online repositories [Genzor, 2016a, Genzor, 2016b, Genzor, 2016c]. We encourage the reader who is experienced in the statistical physics as well as tensor networks to proceed directly to the next chapter(s), where the novel results are presented. Chapter 3 generalizes CTMRG method to hyperbolic geometries and investigates the relationship between the lattice curvature and the free energy. Chapter 4 is concerned with the models of social behavior. We proposed a unique thermodynamic model of social influence, being inspired by a well-known Axelrod model. Again, we have applied the CTMRG method in this study. The phase transitions on fractal geometries are studied in Chapter 5, where a simple fractal lattice is proposed. The HOTRG algorithm is modified and applied to the study of fractals. In addition, we propose two infinite series of fractal lattices converging to either one-dimensional or two-dimensional regular lattices. This work is subject to our ongoing research and will be published elsewhere [Genzor et al.,]. The Chapters 3, 4, and 5 carry the main research results which have been published.

Chapter 1

General introduction and concepts

1.1 Theory of phase transitions

The *phase transition* phenomena has a long history of the study. The term 'phase transition' refers to an abrupt change in properties of a system induced by a change in external parameters like temperature or pressure. The exhibited abrupt change can be described in terms of a non-analyticity of the free energy, i.e., discontinuity in its derivatives. More types of phase transitions are distinguished. The phase transition exhibiting a discontinuity in the first derivative of the free energy is classified as *first-order phase transition*, according to the Ehrenfest classification. One of the examples is solid/liquid/gas transition, see Fig. 1.1. The discontinuity

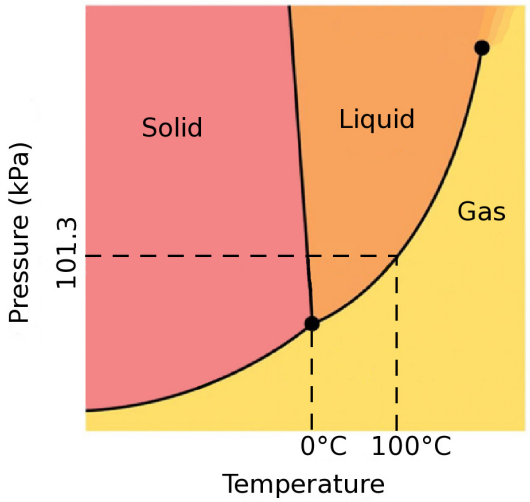

Figure 1.1: The temperature-pressure phase diagram for water.

in the first derivative of the free energy (the internal energy) is associated with the

latent heat, which needs to be exchanged to the transition to occur.

Another type of the phase transition is the *second-order phase transition*, when the first derivative of the free energy is continuous but the second derivative is discontinuous. An important example of the second-order phase transition is a magnetic material, which exhibits nonzero macroscopic spontaneous magnetization, $M_0(T)$, emerging below a specific temperature (the Curie temperature T_{Curie}), cf. Fig. 1.2. If $T < T_{\text{Curie}}$, the spontaneous magnetization can be either positive or negative. The sign of $M_0(T)$ has been determined by symmetry-breaking mechanism initialized by an external magnetic field $h \neq 0$. Hence, the final sign of $M_0(T)$ at zero field obeys the rules

$$\lim_{h\to 0^+} M(h,T) = M_0(T) \quad \text{and} \quad \lim_{h\to 0^-} M(h,T) = -M_0(T), \tag{1.1}$$

where the positive number $M_0(T)$ is called the *spontaneous magnetization*, see Fig. 1.2. However, for temperatures above the Curie temperature $T > T_{\text{Curie}}$, the spontaneous magnetization is strictly zero.

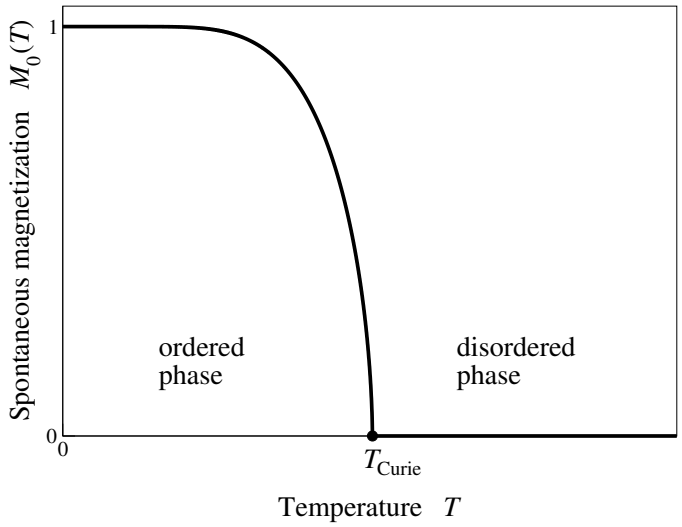

Figure 1.2: The phase diagram for magnetic material. Below the Curie temperature T_{Curie}, the nonzero magnetization $M_0(T)$ emerges, provided that $h \to 0^+$.

1.1.1 Ising model

A simple model of a magnetic material is the Ising model. In this model, the so-called spins are placed on the sites of the lattice. The interaction between spins is limited to the nearest neighbors. A spin variable σ_i at a lattice position

i can assume only two values, either $+1$ or -1. In this simplified model of the ferromagnetic material, the spin Hamiltonian is defined as

$$\mathcal{H}(\sigma) = -\sum_{i \neq j} J_{ij}\sigma_i\sigma_j - \sum_i h_i\sigma_i\,, \tag{1.2}$$

where

$$J_{ij}\begin{cases} > 0 & \text{if } i \text{ and } j \text{ are neighbors}\,, \\ = 0 & \text{otherwise}\,. \end{cases} \tag{1.3}$$

We consider the simplest case of the constant spin interaction $J_{ij} = J$ as well as the constant magnetic field $h_i = h$.

At $T = 0$, the system tends to the minimum energy that is achieved when all the spins are aligned (either in the $+1$ state or in the -1 state). The order parameter is given by the average magnetization.

There is no phase transition in the one-dimensional Ising model; the ordered configuration is obtained only when the temperature is present at $T = h = 0$. The situation is radically different in two dimensions. The phase transitions are rigorously defined only in the thermodynamic limit ($N \to \infty$). At finite but large N, however, a qualitative change in behavior can be observed as the temperature is lowered, see Fig.1.3. At high temperature, the system is in disordered configu-

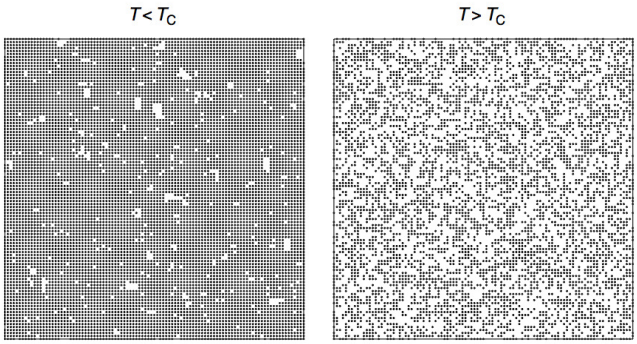

Figure 1.3: Typical snapshots of the Ising system on the square lattice 100×100, below and above critical temperature T_c at $h = 0$. (After [Barrat et al., 2008].)

rations with a globally vanishing magnetization, at low temperature, a symmetry breaking between two possible states $+1$ and -1 takes place. In the thermodynamic limit, a phase transition occurs at critical temperature T_c. Below the critical temperature $T < T_c$, there is an ordered ferromagnetic phase with the spontaneous magnetization $M \neq 0$, whereas above the critical temperature $T > T_c$, a disordered paramagnetic phase with $M = 0$ is present. The two typical analytic solutions for the Ising model exist: on the one-dimensional lattice chain and on the two-dimensional lattice at $h = 0$ [Baxter, 1982].

The Ising model was originally defined in the physical context of magnetism, but the concept of phase transitions is much wider – the Ising model itself lies at the basis of many models of social behavior and opinion dynamics [Barrat et al., 2008].

1.1.2 Equilibrium statistical physics of critical phenomena

Let us start with the definition of the canonical partition function

$$\mathcal{Z} = \sum_{\{\sigma\}} \exp\left(-\frac{\mathcal{H}(\sigma)}{k_{\mathrm{B}}T}\right), \tag{1.4}$$

where $\mathcal{H}(\sigma)$ is the Hamiltonian, the sum is taken over all spin configurations $\{\sigma\}$, and k_{B} is the Boltzmann constant.

The *Helmholtz free energy* F is defined as

$$F = -k_{\mathrm{B}}T \ln(\mathcal{Z}) . \tag{1.5}$$

Taking derivatives of the free energy determines other thermodynamic functions used in the classification of the phase transition. Namely, the first derivative with respect to temperature T results in the *internal energy*

$$U = -T^2 \frac{\partial (F/T)}{\partial T} . \tag{1.6}$$

The consequent derivative of the internal energy with respect to T yields the *specific heat*

$$C = \frac{\partial U}{\partial T} , \tag{1.7}$$

which has a non-analytic (divergent) behavior at a phase transition. Analogously, the first derivative of the free energy with respect to an external field h results in the magnetization

$$M = \left.\frac{\partial F(T,h)}{\partial h}\right|_{h\to 0} , \tag{1.8}$$

and the second derivatives of the free energy with respect to the external magnetic field h specifies the *magnetic susceptibility*

$$\chi = \left.\frac{\partial M}{\partial h}\right|_{h\to 0} . \tag{1.9}$$

The probability for the system to be in a given spin microstate is

$$\mathcal{P}(\sigma) = \frac{1}{\mathcal{Z}} \exp\left[-\frac{\mathcal{H}(\sigma)}{k_{\mathrm{B}}T}\right] . \tag{1.10}$$

An observable (i. e. an averaged thermodynamic function) O at temperature T is given by the formula

$$\langle O \rangle = \sum_{\{\sigma\}} O(\sigma)\mathcal{P}(\sigma) = \frac{1}{\mathcal{Z}} \sum_{\{\sigma\}} O(\sigma) \exp\left[-\frac{\mathcal{H}(\sigma)}{k_{\mathrm{B}}T}\right]. \tag{1.11}$$

Then, equivalently, the internal energy can by expressed as

$$U = \langle \mathcal{H} \rangle = \frac{1}{\mathcal{Z}} \sum_{\{\sigma\}} \mathcal{H}(\sigma) \exp\left(-\frac{\mathcal{H}(\sigma)}{k_{\mathrm{B}}T}\right), \tag{1.12}$$

and, for an example, the magnetization as

$$M = \langle M \rangle = \frac{1}{\mathcal{Z}} \sum_{\{\sigma\}} m(\sigma) \exp\left(-\frac{\mathcal{H}(\sigma)}{k_{\mathrm{B}}T}\right), \tag{1.13}$$

where $M(\sigma)$ is the magnetization per site for a given spin configuration, $m(\sigma) = \left(\sum_{i=1}^{N} \sigma_i\right)/N$.

1.1.3 Correlation function

The correlation function between two spins σ_i and σ_j is defined as

$$g\left(\vec{r_i}, \vec{r_j}\right) = \left\langle \sigma_i \sigma_j \right\rangle - \left\langle \sigma_i \right\rangle \left\langle \sigma_j \right\rangle, \tag{1.14}$$

where $\vec{r_i}$ is the position vector of the lattice site i. Often, the translational invariance is assumed, which leads to $g\left(\vec{r_i}, \vec{r_j}\right) = g\left(r_{ij}\right)$, $r_{ij} = |\vec{r_i} - \vec{r_j}|$. The correlation function $g(r_{ij})$ vanishes for $r_{ij} \to \infty$ at both low and high temperature

$$g(r_{ij}) \propto r_{ij}^{-\tau} \exp(-r_{ij}/\xi), \tag{1.15}$$

where ξ is known as the *correlation length*, and τ is an exponent, which becomes dominant at T_c. At the critical temperature T_c, the correlation length ξ diverges to infinity according to Eq. (1.21) and the correlation function behaves according to Eq. (1.22).

1.1.4 Critical exponents

Here, we briefly recall the definitions of the critical exponents as introduced in [Baxter, 1982]. For convenience, let us define the so-called reduced temperature

$$t = \frac{T - T_c}{T_c}. \tag{1.16}$$

It is expected that for the thermodynamic functions the following expressions hold

$$C(h=0,T) \propto |t|^{-\alpha} \qquad \text{as } t \to 0\,, \tag{1.17}$$

$$M_0(T) \propto (-t)^{\beta} \qquad \text{as } t \to 0^-, \tag{1.18}$$

$$M(h, T=T_c) \propto (h)^{1/\delta} \qquad \text{as } h \to 0\,, \tag{1.19}$$

$$\chi(h=0,T) \propto t^{-\gamma} \qquad \text{as } t \to 0\,, \tag{1.20}$$

$$\xi(h=0,T) \propto t^{-\nu} \qquad \text{as } t \to 0\,, \tag{1.21}$$

$$g(r) \propto r^{-d+2-\eta} \qquad \text{as } t \to 0\,, \tag{1.22}$$

$$s(h=0,T) \propto (-t)^{\mu} \qquad \text{as } t \to 0^-. \tag{1.23}$$

The above relations can be understood as the definitions of the critical exponents. In the Eq. (1.22), the power-law decay of the correlation function depends also on d, which denotes the dimension of the system. The last quantity we have not yet defined is the interfacial tension per unit area s in Eq. (1.23). It is defined only for $h = 0$ and $T < T_c$ and represents the surface free energy due to the interface between the domains.

The critical exponents are not entirely independent on each other. The relations between them are given by various scaling assumptions. For example, by assuming the scaling near the critical temperature T_c

$$\frac{h}{k_{\mathrm{B}} T_c} = M|M|^{\delta-1} g_S\left(t|M|^{-1/\beta}\right), \tag{1.24}$$

for a dimensionless positive monotonic increasing function $g_S(x)$ in the interval $-x_0 < x < \infty$, which vanishes at $-x_0$, one would get the first relation out of the list

$$\gamma = \beta(\delta - 1)\,, \tag{1.25}$$

$$\alpha + 2\beta + \gamma = 2\,, \tag{1.26}$$

$$(2-\eta)\nu = \gamma\,, \tag{1.27}$$

$$\mu + \nu = 2 - \alpha\,, \tag{1.28}$$

$$d\nu = 2 - \alpha\,. \tag{1.29}$$

The last equation, which involves the system dimension d can be derived by making further assumptions, known as *hyperscaling hypothesis*. Knowing just two independent critical exponents, we can find all the other exponents using Eq. (1.25)–Eq. (1.29).

The critical exponents are determined by the dimensionality of the system and the symmetry of the order parameter but do not depend on the detailed form of the microscopic interactions. This concept, known as *universality*, allows to replace a complicated system by a much simpler one of the same dimensionality and

symmetries and obtain the correct critical behavior, e. g., the critical behavior of a fluid system can be the same as that of a ferromagnetic material. The collection of models with the same critical exponents is said to constitute a *universality class*.

1.1.5 Mean-field theory of phase transitions

Here, we recall some notions about the mean-field theory. In mean-field, each spin is considered under the equal influence of all the other spins. Therefore, for energy contribution of one spin σ_i, we can write

$$-\sum_{\text{n.n.}} J\sigma_i\sigma_{\text{n.n.}} \quad \rightarrow \quad -J\sum_{\text{n.n.}} \sigma_i\langle\sigma_{\text{n.n.}}\rangle \quad \rightarrow \quad -qJ\sigma_i M\,, \tag{1.30}$$

where q is the *coordination number*, i. e., the number of the nearest neighbors (n.n.).

In equilibrium, we obtain the selfconsistent equation

$$\begin{aligned} M = \langle\sigma_i\rangle &= \frac{1}{\mathcal{Z}}\sum_{\sigma_i=\pm1}\sigma_i \exp\left(\frac{qJM}{k_{\text{B}}T}\sigma_i\right) \\ &= \frac{\exp\left(\frac{qJ}{k_{\text{B}}T}M\right)-\exp\left(-\frac{qJ}{k_{\text{B}}T}M\right)}{\exp\left(\frac{qJ}{k_{\text{B}}T}M\right)+\exp\left(-\frac{qJ}{k_{\text{B}}T}M\right)} \\ &= \tanh\left(\frac{qJ}{k_{\text{B}}T}M\right). \end{aligned} \tag{1.31}$$

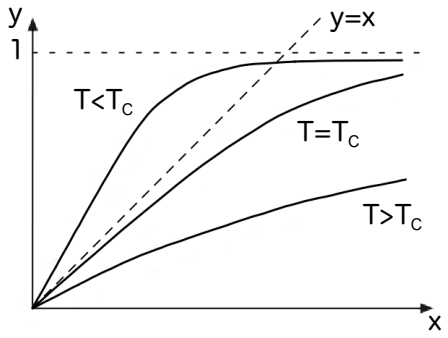

Figure 1.4: Schematic representation of Equation (1.31).

As we can see from Fig.1.4, the solution exists only if

$$\frac{\mathrm{d}}{\mathrm{d}M}\left[\tanh\left(\frac{qJ}{k_{\text{B}}T}M\right)\right]_{M=0} > 1\,. \tag{1.32}$$

This condition is satisfied if and only if $T < T_c$, where $qJ/k_B T_c = 1$. Thus, we obtained the mean-field critical temperature

$$T_c = \frac{qJ}{k_B}. \tag{1.33}$$

It can be shown that the mean-field approximation is valid only above the so-called upper critical Euclidean dimension $d_c = 4$ (for the Ising model) [Yeomans, 1992]. Let us remark that the Ising model on hyperbolic lattices belongs to the mean-field universality class as the Hausdorff dimension of the hyperbolic lattices is infinite. For completeness, the mean-field critical exponents are $\alpha = 0$, $\beta = \frac{1}{2}$, $\gamma = 1$, and $\delta = 3$.

1.2 Transfer matrices for classical systems

1.2.1 The transfer matrix

Here we briefly introduce the important concept known as the *transfer matrix* method. It serves as a prerequisite for the better understanding of the *corner transfer matrix* method, which is discussed subsequently; and, last but not least, the corner transfer matrix method serves as motivation to the CTMRG method, which is employed extensively throughout our study.

It is best to demonstrate the power and the elegance of the transfer matrix method on a simple model; we use the Ising model for this purpose. Therefore, we first consider an analytic solution of the Ising model on a one-dimensional spin chain, and later we briefly generalize the treatment to the two-dimensional case on the square lattice. Let us start with the definition of the Hamiltonian for the one-dimensional Ising model with nearest-neighbors interactions only

$$\mathcal{H} = -J \sum_{i=1}^{N} \sigma_i \sigma_{i+1} - h \sum_{i=1}^{N} \sigma_i, \tag{1.34}$$

where we suppose the ferromagnetic case (i. e., $J > 0$), h is the external field, and N is the system size. Let us also assume the periodic boundary conditions (i. e., $\sigma_{N+1} \equiv \sigma_1$), which lead to the translational invariance of the system. The statistical sum (according to Eq. (1.4)) is then

$$\mathcal{Z} = \sum_{\{\sigma\}} \exp\left(K \sum_{j=1}^{N} \sigma_j \sigma_{j+1} + \Gamma \sum_{j=1}^{N} \sigma_j \right), \tag{1.35}$$

where we introduced the notation $K = J/k_B T$ and $\Gamma = h/k_B T$.

The calculation of the statistical sum can be simplified by the factorization

$$\mathcal{Z} = \sum_{\{\sigma\}} V(\sigma_1,\sigma_2)\, V(\sigma_2,\sigma_3) \ldots V(\sigma_{N-1},\sigma_N)\, V(\sigma_N,\sigma_1)\,, \tag{1.36}$$

where we consider a symmetric structure of the terms

$$V\left(\sigma_i,\sigma_{i+1}\right) = \exp\left[K\sigma_i\sigma_{i+1} + \frac{\Gamma}{2}(\sigma_i+\sigma_{i+1})\right]. \tag{1.37}$$

It is convenient to regard each $V(\sigma_i,\sigma_{i+1})$ as a matrix with row and column indices to be σ_i and σ_{i+1}, respectively,

$$V\left(\sigma_i,\sigma_{i+1}\right) = \begin{pmatrix} V(+1,+1) & V(+1,-1) \\ V(-1,+1) & V(-1,-1) \end{pmatrix} = \begin{pmatrix} e^{K+\Gamma} & e^{-K} \\ e^{-K} & e^{K-\Gamma} \end{pmatrix}. \tag{1.38}$$

The matrix V is called the transfer matrix. Treating the summation $\sum_{\{\sigma\ \neq\sigma_1\}}$ as a matrix multiplication and $\sum_{\{\sigma_1\}}$ as a trace, one obtains

$$\mathcal{Z} = \mathrm{Tr}\left(V^N\right). \tag{1.39}$$

The diagonalization of the matrix V yields

$$V = P\begin{pmatrix} \lambda_1 & 0 \\ 0 & \lambda_2 \end{pmatrix} P^{-1}, \tag{1.40}$$

where P is a matrix with the eigenvectors as its columns, and the two eigenvalues are

$$\lambda_{1,2} = e^K \cosh\Gamma \pm \left(e^{2K}\sinh^2\Gamma + e^{-2K}\right)^{1/2}. \tag{1.41}$$

Using the fact that the trace is invariant under cyclic permutations, we can rewrite the statistical sum as follows

$$\mathcal{Z} = \mathrm{Tr}\left\{\begin{pmatrix} \lambda_1 & 0 \\ 0 & \lambda_2 \end{pmatrix}^N\right\} = \mathrm{Tr}\begin{pmatrix} \lambda_1^N & 0 \\ 0 & \lambda_2^N \end{pmatrix} = \lambda_1^N + \lambda_2^N. \tag{1.42}$$

Now, we would like to express the free energy per site. Then, for the logarithm of the statistical sum, we have

$$\ln\mathcal{Z} = N\ln\lambda_1 + \ln\left[1 + \left(\frac{\lambda_2}{\lambda_1}\right)^N\right] \tag{1.43}$$

Suppose that $|\lambda_2/\lambda_1| < 1$, which is justified for $T > 0$. In the thermodynamic limit (i. e., $N \to \infty$), the free energy per site is simply

$$f = \lim_{N\to\infty} -\frac{k_\mathrm{B}T}{N}\ln\mathcal{Z} = -k_\mathrm{B}T\ln\lambda_1\,. \tag{1.44}$$

Note that the free energy per site is an analytic function for positive T and real h. The phase transition occurs only at $T = 0$ and $h = 0$, as $\lim_{T\to 0^+} \lambda_2/\lambda_2 = 1$ where the correlation length $\xi = [\ln(\lambda_1/\lambda_2)]^{-1}$ diverges.

Let us now discuss the square-lattice case. We consider the Ising model on a regular N by M lattice with the Hamiltonian

$$\mathcal{H} = -J \sum_{i=1}^{N} \sum_{j=1}^{M} \left(\sigma_{i,j}\sigma_{i+1,j} + \sigma_{i,j}\sigma_{i,j+1} \right) - h \sum_{i=1}^{N} \sum_{j=1}^{M} \sigma_{i,j}\,, \tag{1.45}$$

where a spin $\sigma_{i,j}$ is located at row i and column j of the lattice, see Fig. 1.5. Likewise in the one-dimensional case, we suppose the periodic boundary conditions. Again, the statistical sum can be factorized in terms of the transfer matrices T,

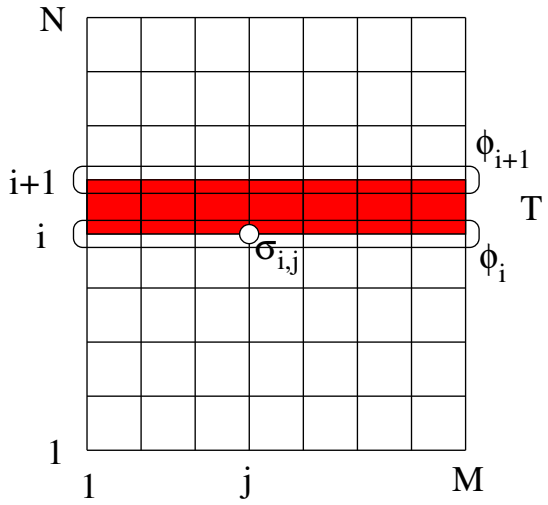

Figure 1.5: Graphical representation of the transfer matrix $T(\phi_i, \phi_{i+1})$ on the square lattice $M \times N$.

this time, it is a large $2^M \times 2^M$ matrix.

Using the similar trick as in the one-dimensional case, we can express the

statistical sum as a trace of the matrix product [1]

$$\mathcal{Z} = \sum_{\{\phi\}} T(\phi_1,\phi_2)\,T(\phi_2,\phi_3)\ldots T(\phi_{N-1},\phi_N)\,T(\phi_N,\phi_1) = \mathrm{Tr}\left(T^N\right), \tag{1.46}$$

where the spin configuration at a row i is denoted as

$$\phi_i = \{\sigma_{i,1}\sigma_{i,2}\ldots\sigma_{i,M}\}\,. \tag{1.47}$$

The free energy per site can be written as

$$f = -\frac{k_\mathrm{B}T}{NM}\ln\left(T^N\right) = -\frac{k_\mathrm{B}T}{NM}\ln\sum_{i=1}^{2^M}\lambda_i^N = \tag{1.48}$$
$$-\frac{k_\mathrm{B}T}{M}\left\{\ln\lambda_1 + \frac{1}{N}\ln\left[1+\sum_{i=2}^{2^M}\left(\frac{\lambda_i}{\lambda_1}\right)^N\right]\right\},$$

We suppose the decreasing ordering of the eigenvalues, in particular, $\lambda_1 > \lambda_2 \geq \cdots \geq \lambda_{(2^M)}$. As approaching the limit $N \to \infty$, the terms $(\lambda_i/\lambda_1)^N$ vanish, and we have a simple formula for the free energy per site

$$f = -\frac{k_\mathrm{B}T}{M}\ln\lambda_1\,. \tag{1.49}$$

It means that to calculate the free energy per site, we just need to know only the largest eigenvalue λ_1, which is usually much easier to obtain than the full spectrum of the $2^M \times 2^M$ transfer matrix.

[1] For convenience, let us first introduce the Boltzmann weight of a basic lattice cell of the square shape

$$\begin{aligned}
&\mathcal{W}_\mathrm{B}\left(\sigma_{i,j},\sigma_{i,j+1},\sigma_{i+1,j},\sigma_{i+1,j+1}\right) = \\
&= \exp\left[\frac{J}{2k_\mathrm{B}T}\left(\sigma_{i,j}\sigma_{i,j+1}+\sigma_{i,j+1}\sigma_{i+1,j+1}+\sigma_{i+1,j+1}\sigma_{i+1,j}+\sigma_{i+1,j}\sigma_{i,j}\right)+\right.\\
&+ \left.\frac{h}{4k_\mathrm{B}T}\left(\sigma_{i,j}+\sigma_{i,j+1}+\sigma_{i+1,j}+\sigma_{i+1,j+1}\right)\right].
\end{aligned}$$

The Boltzmann weight represents the contribution of the corresponding spin-spin and spin-field interactions to the total Hamiltonian of the system. The factor $1/2$ before the spin-spin terms is necessary to avoid the double counting of the J coupling as every side is shared by two Boltzmann weights. Similarly, each site is shared by four Boltzmann weights, hence the factor $1/4$ before the spin-field terms. Now, we can express the transfer matrix in terms of the above defined Boltzmann weights as

$$T(\phi_i,\phi_{i+1}) = \prod_{j=1}^{M}\mathcal{W}_\mathrm{B}\left(\sigma_{i,j},\sigma_{i,j+1},\sigma_{i+1,j},\sigma_{i+1,j+1}\right).$$

1.2.2 The corner transfer matrix

Here, we introduce the concept of the corner transfer matrix C. Consider the two-dimensional Ising model with open boundary conditions (not periodic boundary conditions). Let us divide the system into four identical quadrants, see Fig. 1.6a. The aim of this approach is to express the statistical sum as a product of four corner transfer matrices

$$\mathcal{Z} = \mathrm{Tr}\left(C^4\right). \tag{1.50}$$

For brevity and tutorial purposes, we consider the case without any external field, i. e., when $h = 0$. Let us define the corner transfer matrix as

$$C\left(\sigma\ \xi\ \middle|\sigma\ \xi'\right) = \sum_{\{\sigma\}}{}' \prod_{\langle ij\rangle} \exp\left(\frac{J}{k_\mathrm{B}T}\sigma_i\sigma_j\right) \prod_{\{kl\}} \exp\left(\frac{J}{2k_\mathrm{B}T}\sigma_k\sigma_l\right), \tag{1.51}$$

where the sum $\sum_{\{\sigma\}}{}'$ is taken over all possible spin configurations inside the quadrant (the corresponding summed up spins are indicated by the filled circles in Fig. 1.6b), σ is the spin in the middle of the system (it is shared by all four quadrants), and ξ, ξ' denote the multi-spin variables on the boundary of two adjacent quadrants[2]. The first product over $\langle ij\rangle$ in Eq. (1.51) is taken over all links except those that are shared with other corner transfer matrix. In Fig. 1.6b, these links are indicated by thick lines. The shared links (between the spins indicated by the unfilled circles in Fig. 1.6b) are included in the second product taken over $\{kl\}$; notice the factor $1/2$ in the exponent. Graphically, the shared links are indicated by thin lines in Fig. 1.6b.

The statistical sum can be expressed as

$$\mathcal{Z} = \mathrm{Tr}\left[C\left(\sigma\ \xi\ \middle|\sigma\ \xi'\right)C\left(\sigma\ \xi'\middle|\sigma\ \xi''\right)C\left(\sigma\ \xi''\middle|\sigma\ \xi'''\right)C\left(\sigma\ \xi'''\middle|\sigma\ \xi\ \right)\right], \tag{1.54}$$

where the summation over the spin variables σ, ξ, ξ', ξ'', ξ''' is carried out. For simplicity, the statistical sum can be also written as Eq. (1.50).

Further in this work, we regard the corner transfer matrix C as a tensor, which

[2] For instance, having the N by M lattice, where N and M are both even numbers, the spin in the middle is $\sigma = \sigma_{N/2,M/2}$, and the multi-spin variables ξ and ξ' of upper-right corner transfer matrix are

$$\xi = \{\sigma_{N/2,(M/2+1)}\sigma_{N/2,(M/2+2)}\ldots\sigma_{N/2,M}\}, \tag{1.52}$$

$$\xi' = \{\sigma_{(N/2+1),M/2}\sigma_{(N/2+2),M/2}\ldots\sigma_{N,M/2}\}. \tag{1.53}$$

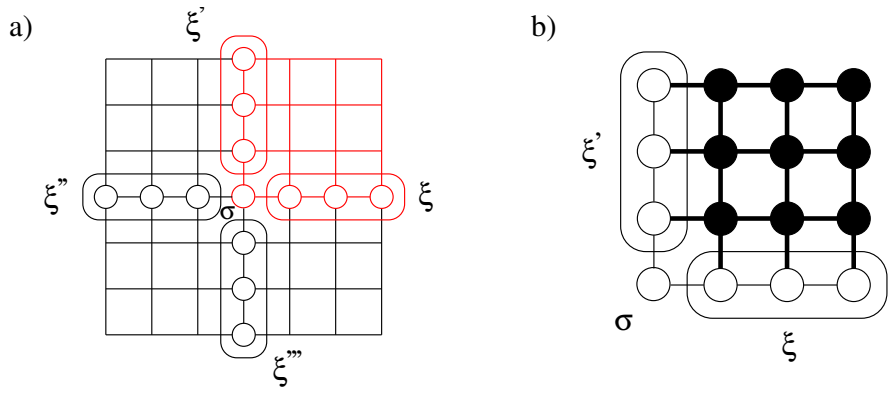

Figure 1.6: Graphical representation of the corner transfer matrix on the square latice: a) The division of the lattice into the four identical quadrants. The spin σ positioned in the middle of the system is shared by the four quadrants, whereas ξ, ξ', ξ'', ξ''' denote the multi-spin variables on the boundaries shared by the two adjacent quadrants. In red color, one of the quadrants (upper-right) is highlighted. b) The upper-right corner transfer matrix $C\left(\sigma\ \xi\ \middle|\sigma\ \xi'\right)$ (or alternatively, the upper-right corner transfer tensor $C_{\sigma\ \xi\ \xi'}$, see Eq. (1.56)). The thick lines represent the terms from the first product in Eq. (1.51), whereas the thin lines represent the terms from the second product (with the factor $1/2$). The sum is taken over the spin configurations of the spins inside the quadrant, which are indicated by the filled circles.

we call the corner transfer tensor; in particular[3]

$$C_{\sigma\ \xi\ \xi'} \equiv C\left(\sigma\ \xi\ \middle|\sigma\ \xi'\right). \tag{1.56}$$

The advantage of the corner transfer matrix approach is that the whole system is being represented by just four matrices. This approach introduced by Baxter [Baxter, 1982] was implemented into the CTMRG algorithm, which is described in Section 2.2.

1.3 Suzuki-Trotter mapping

Here we derive the correspondence between the one-dimensional quantum Ising model in transverse magnetic field h and the two-dimensional classical Ising model

[3] In the tensor language, the statistical sum can be expressed as

$$\mathcal{Z} = \sum_{\sigma\ \xi\ \xi'\xi''\xi'''} C_{\sigma\ \xi\ \xi'} C_{\sigma\ \xi'\xi''} C_{\sigma\ \xi''\xi'''} C_{\sigma\ \xi'''\xi}\ . \tag{1.55}$$

on a square lattice. One can also generalize the correspondence between d-dimensional quantum spin models and $(d+1)$-dimensional classical spin models.

Let us begin with the definition of the Hamiltonian for the one-dimensional transverse-field Ising model

$$\mathcal{H} = -J \sum_{i=1}^{N} \hat{\sigma}_z^{[i]} \hat{\sigma}_z^{[i+1]} - h \sum_{i=1}^{N} \hat{\sigma}_x^{[i]}, \tag{1.57}$$

where the indices in the square brackets label the spin position on a chain with N sites and we impose the periodic boundary conditions, i.e., $[N+1] \equiv [1]$. The Pauli matrices are denoted as

$$\hat{\sigma}_x = \begin{pmatrix} 0 & 1 \\ 1 & 0 \end{pmatrix}, \tag{1.58}$$

$$\hat{\sigma}_y = \begin{pmatrix} 0 & -i \\ i & 0 \end{pmatrix}, \tag{1.59}$$

$$\hat{\sigma}_z = \begin{pmatrix} 1 & 0 \\ 0 & -1 \end{pmatrix}, \tag{1.60}$$

and we denote the identity in what follows as

$$I = \begin{pmatrix} 1 & 0 \\ 0 & 1 \end{pmatrix}. \tag{1.61}$$

The partition function for the system can be written as

$$\mathcal{Z} = \mathrm{Tr}\, \exp(-\mathcal{H}/T) = \mathrm{Tr}\left[\exp(-\Delta\tau \mathcal{H})\right]^{M_\tau}, \tag{1.62}$$

where $1/T = M_\tau \Delta\tau$ is fixed and we are interested in the limits $\Delta\tau \to 0$ and $M_\tau \to \infty$. This can be understood as a system with M_τ rows in τ direction (which can be thought of as an imaginary time evolution).

Using the Suzuki-Trotter expansion, the exponential operators can be expressed as

$$\exp(-\Delta\tau \mathcal{H}) = T_1 T_2 + O\left(\Delta\tau^2\right), \tag{1.63}$$

where we defined the two transfer matrices

$$T_1 = \exp\left(\Delta\tau h \sum_{i}^{N} \hat{\sigma}_x^{[i]}\right), \tag{1.64}$$

$$T_2 = \exp\left(\Delta\tau J \sum_{i}^{N} \hat{\sigma}_z^{[i]} \hat{\sigma}_z^{[i+1]}\right). \tag{1.65}$$

Denoting the eigenstates of all the $\hat{\sigma}_z^{[i]}$ as $|\{S_z^i\}\rangle$, where $S_z^i = \pm 1$ are eigenvalues of $\hat{\sigma}_z$, we can immediately see that T_2 is diagonal with respect to that basis

$$T_2 |\{S_z^i\}\rangle = e^{\Delta\tau J \sum_{i=1}^N S_z^i S_z^{i+1}} |\{S_z^i\}\rangle . \tag{1.66}$$

Inserting the complete basis set M_τ times into $\mathcal{Z}$, we obtain

$$\mathcal{Z} = \sum_{\{S_z^i(\ell)\}} \prod_{\ell=1}^{M_\tau} \langle \{S_z^i(\ell)\}| T_1 T_2 |\{S_z^i(\ell+1)\}\rangle , \tag{1.67}$$

where ℓ labels the imaginary time step. Using Eq. (1.66), we can write

$$\langle \{S_z^i(\ell)\}| T_1 T_2 |\{S_z^i(\ell+1)\}\rangle = e^{\Delta\tau J \sum_{i=1}^N S_z^{i,\ell} S_z^{i+1,\ell}} \langle \{S_z^i(\ell)\}| T_1 |\{S_z^i(\ell+1)\}\rangle . \tag{1.68}$$

Now, we need to find the elements of the transfermatrix T_1.

From the Taylor expansion, we have

$$e^{\Delta\tau h \hat{\sigma}_x} = I \cosh(\Delta\tau h) + \hat{\sigma}_x \sinh(\Delta\tau h) . \tag{1.69}$$

Assuming the following form of the matrix elements

$$\langle S_z | e^{\Delta\tau \hat{\sigma}_x} | S_z' \rangle =: A e^{B S_z S_z'} , \tag{1.70}$$

where $S_z, S_z' = \pm 1$, and using Eq. (1.69), we obtain

$$\langle S_z | e^{\Delta\tau \hat{\sigma}_x} | S_z \rangle = \cosh(\Delta\tau h) = A e^{B} , \tag{1.71}$$

$$\langle -S_z | e^{\Delta\tau \hat{\sigma}_x} | S_z \rangle = \sinh(\Delta\tau h) = A e^{-B} , \tag{1.72}$$

and thus

$$A^2 = \sinh(\Delta\tau h)\cosh(\Delta\tau h) \qquad B = -\frac{1}{2} \ln\left[\tanh(\Delta\tau h)\right] . \tag{1.73}$$

Now, we can rewrite the statistical sum as follows

$$\mathcal{Z} = A^{N M_\tau} \sum_{\{S^{i,l} = \pm 1\}} \exp\left(\Delta\tau J \sum_{i=1}^{N} \sum_{\ell=1}^{M_\tau} S^{i,\ell} S^{i+1,\ell} + B \sum_{i=1}^{N} \sum_{\ell=1}^{M_\tau} S^{i,\ell} S^{i,\ell+1} \right) . \tag{1.74}$$

This statistical sum is identical to the two-dimensional classical Ising model with the Hamiltonian (defined on a rectangular N by M_τ lattice)

$$\mathcal{H} = -K_1 \sum_{i=1}^{N} \sum_{\ell=1}^{M_\tau} S^{i,\ell} S^{i+1,\ell} - K_2 \sum_{i=1}^{N} \sum_{\ell=1}^{M_\tau} S^{i,\ell} S^{i,\ell+1} , \tag{1.75}$$

where $K_1 = T_{\text{cl.}} \Delta\tau J$ and $K_2 = T_{\text{cl.}} B$ with $T_{\text{cl.}}$ being the thermodynamic temperature.

Chapter 2

Tensor network states

2.1 TEBD: MPS for ground states

This Section provides a description of the iTEBD algorithm introduced in [Vidal, 2007]. This algorithm is used for an efficient simulation of one-dimensional quantum lattice systems. Here, we focus on the computation of the ground state by evolution in the imaginary time; however, it is straightforward to consider the time evolution as well. This Section also demonstrates the application of the algorithm on the quantum Ising and Heisenberg models in simple, practical terms.

Let us consider an infinite one-dimensional lattice with each lattice site having d degrees of freedom (possible states), i. e., the physical dimension of each lattice site is d. For instance, a spin-$\frac{1}{2}$ lattice model has $d = 2$ such as the Ising or Heisenberg models. Let us also assume that only the nearest neighbors interact. Thus, the interactions are given by the translational invariant Hamiltonian

$$\mathcal{H} = \sum_{r=-\infty}^{\infty} \mathcal{H}_{\text{loc}}^{[r,r+1]}, \tag{2.1}$$

where r denotes the location of a site. As the lattice size is infinite, the translational invariance of the state is assumed. In imaginary time τ, an initial pure state $|\Psi_0\rangle$ evolves as

$$|\Psi_\tau\rangle = \frac{\exp(-\mathcal{H}\tau)|\Psi_0\rangle}{\|\exp(-\mathcal{H}\tau)\,|\Psi_0\rangle\|}. \tag{2.2}$$

MPS expansion Any pure state $|\Psi\rangle$ can be represented as a Matrix Product State (MPS) by a series of Schmidt decompositions. By dividing the lattice into two sublattices $\{-\infty, ..., r\}$ and $\{(r+1), ..., \infty\}$, we obtain

$$|\Psi\rangle = \sum_{\alpha=1}^{\chi} \lambda_\alpha^{[r]} |\Phi_\alpha^{[\triangleleft r]}\rangle |\Phi_\alpha^{[r+1\triangleright]}\rangle, \tag{2.3}$$

where λ_α are the Schmidt coefficients (with the properties: $\sum_{\alpha=1}^{\chi} \lambda_\alpha^2 = 1$, $\lambda_1 \leq \lambda_2 \leq \ldots \leq \lambda_\chi \leq 0$), χ is the Schmidt rank, and $|\Phi_\alpha^{[\lhd r]}\rangle$ and $|\Phi_\alpha^{[r+1\rhd]}\rangle$ are the orthonormal basis vectors of the left and right sublattice, respectively. To express the state $|\Psi\rangle$ with respect to the local basis $|i^{[r]}\rangle$ and $|i^{[r+1]}\rangle$ of sites r and $(r+1)$, respectively, we use the following decompositions

$$|\Psi_\alpha^{[\lhd r]}\rangle = \sum_{\beta=1}^{\chi} \sum_{i=1}^{d} \lambda_\beta^{[r-1]} \Gamma_{i\beta\alpha}^{[r]} |\Phi_\beta^{[\lhd r-1]}\rangle |i^{[r]}\rangle, \tag{2.4}$$

$$|\Psi_\alpha^{[r+1\rhd]}\rangle = \sum_{\beta=1}^{\chi} \sum_{i=1}^{d} \Gamma_{i\beta\alpha}^{[r+1]} \lambda_\beta^{[r+1]} |i^{[r+1]}\rangle |\Phi_\beta^{[r+2\rhd]}\rangle, \tag{2.5}$$

where Γ's are three-index tensors of the respective dimensions d by χ by χ. Notice that i and j are the physical indices (with d possible states, which is the physical dimension of each individual site), whereas α, β, and γ are the bond or ancillary indices with χ possible values, which is called the bond dimension. The bond dimension χ is infinite in principle; however, in numerical calculations, a cut-off is necessary and the maximal allowed Schmidt rank is denoted by D. The insertion of Eq. (2.4) and Eq. (2.5) into Eq. (2.3) yields the expansion of $|\Psi\rangle$ for sites $\{r, r+1\}$

$$|\Psi\rangle = \sum_{\alpha,\beta,\gamma=1}^{\chi} \sum_{i,j=1}^{d} \lambda_\alpha^{[r-1]} \Gamma_{i\alpha\beta}^{[r]} \lambda_\beta^{[r]} \Gamma_{j\beta\gamma}^{[r+1]} \lambda_\gamma^{[r+1]} |\Phi_\alpha^{[\lhd r-1]}\rangle |i^{[r]}\rangle |j^{[r+1]}\rangle |\Phi_\gamma^{[r+2\rhd]}\rangle. \tag{2.6}$$

The pure state $|\Psi\rangle$ can be represented as a single tensor given by the coefficients

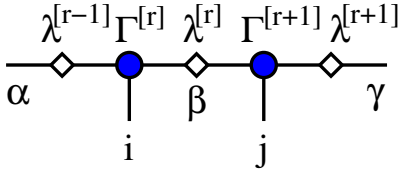

Figure 2.1: Graphical representation of the expansion of a pure state $|\Psi\rangle$ with respect to the sites $\{r, r+1\}$ as a single tensor $\Psi_{\alpha i j \gamma}$.

of the above expansion (see Fig. 2.1)

$$\Psi_{\alpha i j \gamma} = \sum_{\beta=1}^{\chi} \lambda_\alpha^{[r-1]} \Gamma_{i\alpha\beta}^{[r]} \lambda_\beta^{[r]} \Gamma_{j\beta\gamma}^{[r+1]} \lambda_\gamma^{[r+1]}. \tag{2.7}$$

The non-unitary evolution operator acting in Eq. (2.2) can be expanded by Suzuki-Trotter decomposition into a sequence of two-site gates

$$V^{[r,r+1]} \equiv \exp\left(-\mathcal{H}_{\text{loc}}^{[r,r+1]} \delta\tau\right), \quad 0 < \delta\tau \ll 1. \tag{2.8}$$

The two-site gates are arranged into the gates V^{AB} and V^{BA}, which act on the sites $\{2r, 2r+1\}$ and $\{2r+1, 2r+2\}$, respectively; in particular

$$V^{AB} \equiv \bigotimes_r V^{[2r,2r+1]}, \quad V^{BA} \equiv \bigotimes_r V^{[2r+1,2r+2]}. \tag{2.9}$$

This construction breaks the assumed translational symmetry (i. e., independence on r), and is taken into account by the following ansatz of the MPS

$$\Gamma^{[2r]} = \Gamma^A, \quad \lambda^{[2r]} = \lambda^A, \tag{2.10}$$

$$\Gamma^{[2r+1]} = \Gamma^B, \quad \lambda^{[2r+1]} = \lambda^B. \tag{2.11}$$

MPS update For even-odd pair of sites $\{2r, 2r+1\}$, we can write the following state expansion

$$\Psi^{AB}_{\alpha i j \gamma} = \sum_{\beta=1}^{\chi} \lambda^B_\alpha \Gamma^A_{i\alpha\beta} \lambda^A_\beta \Gamma^B_{j\beta\gamma} \lambda^B_\gamma. \tag{2.12}$$

The application of the non-unitary operator V on the state yields (a new tensor)

$$\Theta^{AB}_{\alpha i, j\gamma} = V_{ij,kl} \Psi^{AB}_{\alpha k l \gamma}, \tag{2.13}$$

where we regrouped the indices to obtain a matrix $\Theta^{AB}_{\{\alpha i\},\{j\gamma\}}$. Notice that for the matrix $V_{\{ij\},\{kl\}}$, the grouped indices $\{ij\}$ and $\{kl\}$ are understood as $\{ij\} = (di + j)$ and $\{kl\} = (dk + l)$, respectively. Then, we perform the Singular Value Decomposition (SVD) of the matrix Θ^{AB}

$$\Theta^{AB}_{\alpha i, j\gamma} = X_{\alpha i, \beta} \tilde{\lambda}^A_\beta Y_{\beta, j\gamma}, \tag{2.14}$$

which gives us the new updated $\tilde{\lambda}^A_\beta$ coefficients.

Notice that now the index β can take $d \cdot \chi$ values. The truncation can be performed in two consecutive steps. First, check if $d \cdot \chi$ is larger than D; if this is the case, truncate the dimension $d \cdot \chi$ down to D, otherwise no truncation is performed. Second, truncate the dimension up to the largest β index for which $\lambda_\beta > \varepsilon$, for a small value of ε. Subsequently, we update the Γ tensors as

$$\tilde{\Gamma}^A_{i\alpha\beta} = X_{\alpha i, \beta} / \lambda^B_\alpha, \quad \tilde{\Gamma}^B_{j\beta\gamma} = Y_{j\beta, \gamma} / \lambda^B_\gamma. \tag{2.15}$$

The reason of the division by λ^B in the last pair of equations lies in the reintroduction of λ^B back into the network. Next, we normalize the updated $\tilde{\lambda}^A_\beta$ coefficients by dividing each coefficient by the norm

$$\sqrt{\sum_\beta \left(\tilde{\lambda}^A_\beta\right)^2}.$$

There is no need for any normalization of the Γ tensors.

Expectation values Here, we demonstrate a technique used for obtaining the expectation values for the state $|\Psi\rangle$. This technique is simple enough to be sufficient to explain it on two specific examples, i. e., the local energy and the magnetization. The energy per one site corresponding to the state can be calculated by simply taking the sum

$$\langle\Psi|\mathcal{H}|\Psi\rangle = \sum_{\alpha,\gamma=1}^{\chi}\sum_{i,j,k,l=1}^{d}\Psi_{\alpha kl\gamma}(\mathcal{H}_{\mathrm{loc}})_{kl,ij}\Psi_{\alpha ij\gamma}, \tag{2.16}$$

where we used the two-site MPS expansion $\Psi_{\alpha ij\gamma}$ defined in Eq. (2.12). The magnetization is just an expectation value of a chosen Pauli matrix σ. As this is a one-site observable, we use a one-site expansion of the state $\Psi_{\alpha i\beta} = \lambda^B_\alpha\Gamma^A_{i\alpha\beta}\lambda^A_\beta$. Hence, the magnetization is

$$\langle\Psi|\sigma|\Psi\rangle = \sum_{\alpha,\beta=1}^{\chi}\sum_{i,k=1}^{d}\lambda^B_\alpha\Gamma^A_{k\alpha\beta}\lambda^A_\beta(\sigma)_{k,i}\lambda^B_\alpha\Gamma^A_{i\alpha\beta}\lambda^A_\beta. \tag{2.17}$$

2.1.1 Ising model

The Hamiltonian of the one-dimensional quantum Ising model with transverse magnetic field h is defined as

$$\mathcal{H} = \sum_{r\in\mathbb{Z}}\left(\hat{\sigma}_x^{[r]}\hat{\sigma}_x^{[r+1]} + h\hat{\sigma}_z^{[r]}\right). \tag{2.18}$$

The Pauli matrices are defined in Eq. (1.58)–(1.60) and for the identity we use the following notation

$$I = \begin{pmatrix}1 & 0\\ 0 & 1\end{pmatrix}. \tag{2.19}$$

Thus, for the local Hamiltonian we have

$$\mathcal{H}_{\mathrm{loc}} = \hat{\sigma}_x\otimes\hat{\sigma}_x + \frac{h}{2}\left(\hat{\sigma}_z\otimes I + I\otimes\hat{\sigma}_z\right). \tag{2.20}$$

The imaginary-time evolution is realized by the application of the non-unitary operator $\exp\left(-\tau\mathcal{H}_{\mathrm{loc}}\right)$

$$\begin{pmatrix}\cosh(\tau s) - \frac{h\sinh(\tau s)}{s} & 0 & 0 & -\frac{\sinh(\tau s)}{s}\\ 0 & \cosh(\tau) & -\sinh(\tau) & 0\\ 0 & -\sinh(\tau) & \cosh(\tau) & 0\\ -\frac{\sinh(\tau s)}{s} & 0 & 0 & \cosh(\tau s) + \frac{h\sinh(\tau s)}{s}\end{pmatrix}, \tag{2.21}$$

where $s = \sqrt{1+h^2}$.

MPS initialization In our experience with the numerical calculations, the following MPS initialization ansatz proved to be appropriate for the Ising model (with the bond dimension being $\chi = 1$ in the initialization)

$$\Gamma^A = [1,0], \quad \Gamma^B = [1,0] \quad \lambda^A = [1], \quad \lambda^B = [1]. \tag{2.22}$$

Numerical results Let us calculate the ground state energy E_0 of the one-dimensional quantum Ising model at the criticality $h = 1$. Two strategies are at hand. The first is to use a fixed imaginary-time step $\delta\tau$ as in Fig. 2.2, the second is to divide $\delta\tau$ by a fixed number (we used two as the divisor) each time the ground state energy $E^{(n)}$ converges with respect to the iterative step n as in Fig. 2.3. In the following numerical calculations, we used the maximal bond dimension

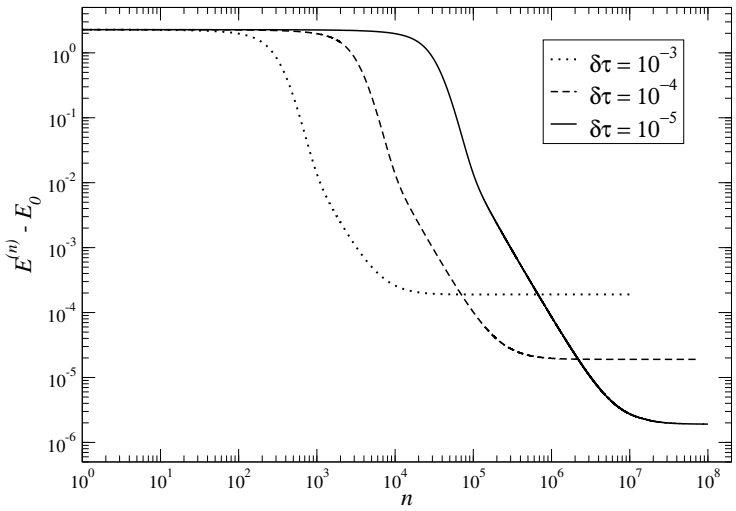

Figure 2.2: Imaginary time evolution for the one-dimensional quantum Ising model with the external field $h = 1$ and the time step $\delta\tau = \{10^{-3}, 10^{-4}, 10^{-5}\}$ (here we use $D = 32$). The energy at the n^{th} time evolution step $E^{(n)}$ converges to the ground state energy $E_0 = -4/\pi$ as n increases depending on the value of the time step $\delta\tau$.

$D = 32$ (and the parameter $\varepsilon = 10^{-32}$ in the MPS extensions). Notice that for smaller $\delta\tau$ it is possible to achieve better accuracy (i.e., smaller absolute error $|E^{(n)} - E_0|$); however it requires more iterative steps to converge. For fixed $\delta\tau = \{10^{-3}, 10^{-4}, 10^{-5}\}$, we achieved the absolute errors $|E^{(n)} - E_0| \sim \{10^{-4}, 10^{-5}, 10^{-6}\}$, respectively (see Fig. 2.2), where the exact value of the ground state energy is $E_0 = -4/\pi = -1.27324...$ [Šamaj, 2010]. Using the adaptive strategy, we achieved the maximal accuracy $|E^{(n)} - E_0| \lesssim 10^{-7}$ (see Fig. 2.3).

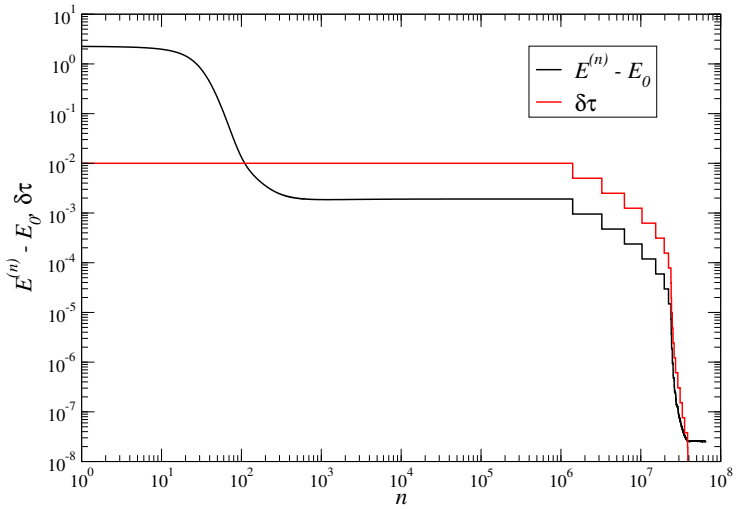

Figure 2.3: Imaginary time evolution for the one-dimensional quantum Ising model with the external field $h = 1$ and the adaptive time step $\delta\tau$ starting with $\delta\tau = 10^{-2}$ ($D = 32$). The time step $\delta\tau$ is divided by a factor of two every time the energy converges. After $\lesssim 10^8$ iterative steps, further divisions of $\delta\tau$ does not decrease the difference $E^{(n)} - E_0$.

2.1.2 Heisenberg model

The Hamiltonian of the one-dimensional quantum Heisenberg model with transverse magnetic field h is defined as

$$\mathcal{H} = \sum_{r\in\mathbb{Z}} \left(\hat{\sigma}_x^{[r]} \hat{\sigma}_x^{[r+1]} + \hat{\sigma}_y^{[r]} \hat{\sigma}_y^{[r+1]} + \hat{\sigma}_z^{[r]} \hat{\sigma}_z^{[r+1]} + h\hat{\sigma}_z^{[r]} \right). \tag{2.23}$$

One can easily find that the local Hamiltonian is

$$\mathcal{H}_{\text{loc}} = \hat{\sigma}_x \otimes \hat{\sigma}_x + \hat{\sigma}_y \otimes \hat{\sigma}_y + \hat{\sigma}_z \otimes \hat{\sigma}_z + \frac{h}{2} \left(\hat{\sigma}_z \otimes I \ + I \ \otimes \hat{\sigma}_z \right). \tag{2.24}$$

By exponentiating the local Hamiltonian, we obtain the following non-unitary (imaginary-time evolution) operator

$$\exp\left(-\tau \mathcal{H}_{\text{loc}}\right) = \begin{pmatrix} e^{-\tau(1+h)} & 0 & 0 & 0 \\ 0 & e^{\tau}\cosh(2\tau) & -e^{\tau}\sinh(2\tau) & 0 \\ 0 & -e^{\tau}\sinh(2\tau) & e^{\tau}\cosh(2\tau) & 0 \\ 0 & 0 & 0 & e^{-\tau(1-h)} \end{pmatrix}. \tag{2.25}$$

MPS initialization For the Heisenberg model, we initialize the MPS (with $\chi = 1$) as

$$\Gamma^A = [1,0], \quad \Gamma^B = [0,1] \quad \lambda^A = [1], \quad \lambda^B = [1]. \tag{2.26}$$

In our experience, this ansatz provides stable solution for the Heisenberg model. On the contrary, the Ising ansatz from Eq. (2.22) is not appropriate in this case and leads to the trivial MPS updates with the constant $\chi = 1$.

Numerical results Likewise for the Ising model, let us now calculate the ground state energy E_0 of the one-dimensional quantum Heisenberg model at the criticality $h = 0$. Again, we used the maximal bond dimension $D = 32$ (and the parameter $\varepsilon = 10^{-32}$ in the MPS extensions). For fixed $\delta\tau = \{10^{-3}, 10^{-4}, 10^{-5}\}$, we achieved the absolute errors $|E^{(n)} - E_0| \sim \{10^{-3}, 10^{-4}, 10^{-5}\}$, respectively (see Fig. 2.4), where the exact value of the ground state energy is $E_0 = 1/4 - \ln(2) = -0.44315...$ [Mattis and Pan, 1988]. Notice that the absolute errors are one order

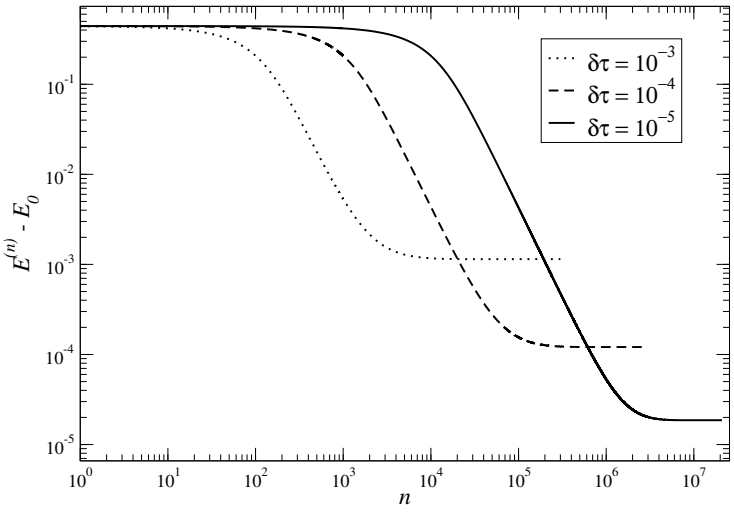

Figure 2.4: Imaginary time evolution for the one-dimensional quantum Heisenberg model with the external field $h = 0$ and the time step $\delta\tau = \{10^{-3}, 10^{-4}, 10^{-5}\}$ (here we use $D = 32$). The energy at the n^{th} time evolution step $E^{(n)}$ converges to the ground state energy $E_0 = 1/4 - \ln(2)$ as n increases depending on the value of the time step $\delta\tau$.

larger that those of the Ising model. By the adaptive strategy, we achieved the maximal accuracy $|E^{(n)} - E_0| \lesssim 10^{-5}$ (see Fig. 2.5), which is roughly two orders larger than the absolute error of the adaptive strategy for the Ising model. Also, the Heisenberg models seems to be less numerically stable than the Ising model, which can be observed in the behavior of the calculated energy $E^{(n)}$ after many iterative steps ($n \sim 10^8$), see the inset of Fig. 2.5. Here, the accumulation of tiny numerical errors leads to the slight increase in the energy $E^{(n)}$, which is otherwise supposed to converge to E_0 in the theory.

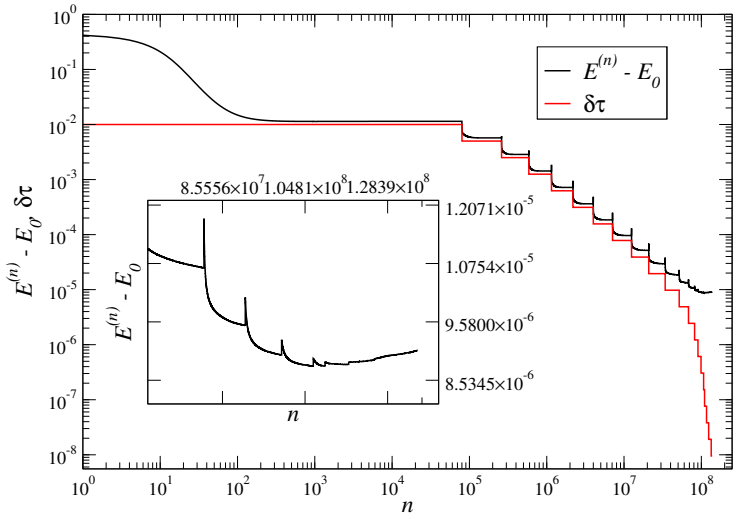

Figure 2.5: Imaginary time evolution for the one-dimensional quantum Heisenberg model with the external field $h = 0$ and the adaptive time step $\delta\tau$ starting with $\delta\tau = 10^{-2}$ ($D = 32$). The time step $\delta\tau$ is divided by a factor of two every time the energy converges. After $\sim 10^8$ iterative steps, further divisions of $\delta\tau$ does not decrease the difference $E^{(n)} - E_0$. The inset captures the behavior of the calculated energy after many iterative steps ($\sim 10^8$).

2.2 CTMRG

We have first encountered the Baxter's concept of the corner transfer matrix on a square lattice in Subsection 1.2.2. This concept was later adapted by Nishino and Okunishi for the numerical renormalization method for two-dimensional classical systems CTMRG [Nishino and Okunishi, 1996, Nishino and Okunishi, 1997]. Here, we provide a step-by-step introduction to the CTMRG method.

Since CTMRG is an iterative numerical algorithm, let integer $k = 1, 2, 3, \ldots$ enumerate the iterative steps. With each iterative step k, the size of the square lattice increases as $(2k+1)\times(2k+1)$. For better understanding, let us explain the CTMRG technique using the Ising model.

Initialization Let us start with the Ising model on the square lattice as small as 3×3 (i.e., $k = 1$); thus, the size of each quadrant is 2×2 only. For the Boltzmann weight $\mathcal{W}_\mathrm{B}$ being the basic lattice cell 2×2 (see Fig. 2.6, left), we have

$$\mathcal{W}_\mathrm{B}\left(\sigma_1,\sigma_2,\sigma_3,\sigma_4\right) = \exp\left[\frac{J}{2k_\mathrm{B}T}\left(\sigma_1\sigma_2+\sigma_2\sigma_3+\sigma_3\sigma_4+\sigma_4\sigma_1\right)+\right.$$
$$\left.+\frac{h}{4k_\mathrm{B}T}\left(\sigma_1+\sigma_2+\sigma_3+\sigma_4\right)\right]. \qquad (2.27)$$

The half-row transfer matrix $\mathcal{T}$ is initialized (see Fig. 2.6, middle) as

$$\mathcal{T}\left(\sigma_1,\sigma_2,\sigma_3,\sigma_4\right) = \exp\left[\frac{J}{2k_{\mathrm{B}}T}\left(\sigma_1\sigma_2 + 2\sigma_2\sigma_3 + \sigma_3\sigma_4 + \sigma_4\sigma_1\right) + \right.$$
$$\left. + \frac{h}{4k_{\mathrm{B}}T}\left(\sigma_1 + 2\sigma_2 + 2\sigma_3 + \sigma_4\right) + \frac{g}{4k_{\mathrm{B}}T}\left(2\sigma_2 + 2\sigma_3\right)\right], \qquad (2.28)$$

where g is an external field imposed on the boundary spins only (used for forcing the symmetry breaking). Notice that the spin-spin interaction term $\sigma_2\sigma_3$ is here with the overall factor of $(2/2) = 1$ (instead of $1/2$) because this interaction is located on the boundary and is not shared with any other. Also, the boundary spins σ_2 and σ_3 have the overall factor of $(2/4) = (1/2)$ to count their energy contribution correctly as they are shared by two lattice cells (instead of four).

The corner transfer matrix C is initialized (see Fig. 2.6, right) as

$$C\left(\sigma_1,\sigma_2,\sigma_4\right) = \sum_{\sigma_3}\exp\left[\frac{J}{2k_{\mathrm{B}}T}\left(\sigma_1\sigma_2 + 2\sigma_2\sigma_3 + 2\sigma_3\sigma_4 + \sigma_4\sigma_1\right) + \right.$$
$$\left. + \frac{h}{4k_{\mathrm{B}}T}\left(\sigma_1 + 2\sigma_2 + 4\sigma_3 + 2\sigma_4\right) + \frac{g}{4k_{\mathrm{B}}T}\left(2\sigma_2 + 4\sigma_3 + 2\sigma_4\right)\right]. \qquad (2.29)$$

Similar to the case of the half-row transfer matrix, the analogous considerations hold in counting the energy contributions of the spins. Notice, that the spin σ_3 appears here with the factor $(4/4) = 1$ as it is in the corner (i. e., it is not shared by any other lattice cell). Also notice, that the sum is taken over degrees of freedom of the spin σ_3.

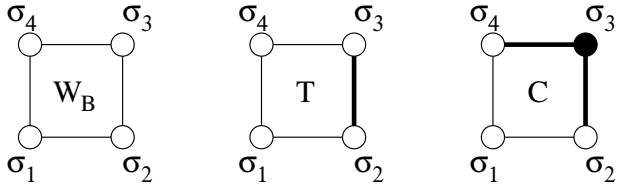

Figure 2.6: Graphical representation of the Boltzmann weight $\mathcal{W}_{\mathrm{B}}$ (left), the half-row transfer matrix $\mathcal{T}$ (middle), and the corner transfer matrix C (right). The thin lines correspond to the shared links (which are accounted for by the overall factor of $1/2$ before the interaction terms in Eq. (2.28) and Eq. (2.29)), whereas the thick lines are on the system boundary. The filled circle in the corner transfer matrix C indicates the summation taken over the spin σ_3.

Density matrix The density matrix is defined as a cut of the lattice system at any step k, see Fig. 2.7. For convenience, let us construct the density matrix in two

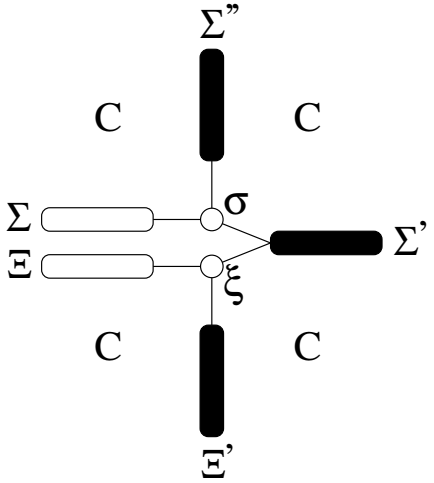

Figure 2.7: Graphical representation of the density matrix $\rho\left(\Sigma\,\sigma\,\middle|\Xi\,\xi\,\right)$. The summation is taken over the filled shapes.

steps. First, one has to calculate a statistical weight A (see Fig. 2.8a) by joining and contracting two corner matrices in the following way

$$A_{\Sigma\,\sigma\,\Sigma'} = \sum_{\Sigma''} C\left(\sigma\,\Sigma'\middle|\sigma\Sigma''\right) C\left(\sigma\,\Sigma''\middle|\sigma\,\Sigma\right), \tag{2.30}$$

where the Greek uppercase letters denote the multi-spin variables with n possible states.

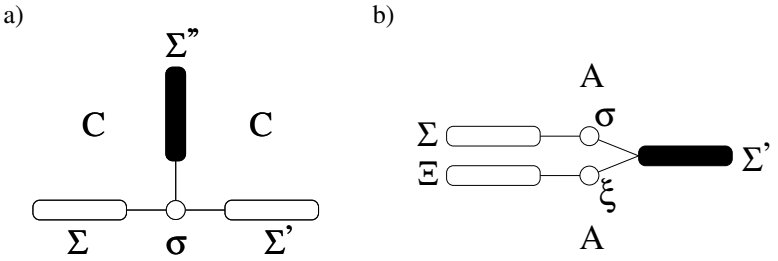

Figure 2.8: Density matrix construction proceeds in two steps: a) Graphical representation of the statistical weight of the upper half of the system $A_{\Sigma\,\sigma\,\Sigma'}$, see Eq. (2.30). The summation is taken over the multispin variable Σ'' (indicated by the filled shape) b) Graphical representation of the construction of the density matrix $\rho\left(\Sigma\,\sigma\,\middle|\Xi\,\xi\,\right)$ according to the Eq. (2.31). The summation is taken over the multispin variable Σ' (indicated by the filled shape).

Second, using the above-defined weight A, the density matrix [1] is (see Fig. 2.8b)

[1] To obtain the genuine density matrix, the weight A is considered in a vector form and nor-

then

$$\rho\Big(\Sigma\ \sigma\ \Big|\Xi\ \xi\ \Big) = \sum_{\Sigma'} A_{\Sigma\ \sigma\ \Sigma'} A_{\Xi\ \xi\ \Sigma'}\,. \tag{2.31}$$

Projection operator The density matrix has the dimension $2n \times 2n$. Denote the maximal number of the spin states in the multi-state variables Σ, Ξ as m. Then, if $2n \le m$, no truncation is performed, and the projection operator P is simply constructed by arranging all the eigenvectors of the density matrix as columns. However, if $2n > m$, we keep only the eigenvectors corresponding to the m largest eigenvalues of the density matrix

$$\left(\begin{array}{cccccc} | & | & \cdots & | & \cdots & | \\ \phi_1 & \phi_2 & \cdots & \phi_{2n-m+1} & \cdots & \phi_{2n} \\ | & | & \cdots & | & \cdots & | \end{array}\right), \tag{2.32}$$

$$\underbrace{\qquad\qquad\qquad\qquad}_{=P}$$

where we assumed that the corresponding eigenvalues of the density matrix ρ are ordered in the increasing order, $d_1 \le d_2 \le \cdots \le d_{2n}$ (as is the usual case in the numerical diagonalization routines).

The transfer matrix extension and renormalization The transfer matrix $\mathcal{T}_k$ constructed in the k^{th} iterative step is extended by an extra Boltzmann weight $\mathcal{W}_{\text{B}}$, see Fig. 2.9. The renormalization of the degrees of freedom is performed by the projection operator P. In particular, the new transfer matrix is obtained as

$$\begin{aligned}\mathcal{T}_{k+1}\left(\sigma'\Sigma'\middle|\xi'\Xi'\right) = \sum_{\sigma,\Sigma,\xi,\Xi} & P(\Xi\ \xi\ ,\Xi')\mathcal{W}_{\text{B}}\left(\sigma'\sigma\ \xi\ \xi'\right) \\ & \mathcal{T}_k\Big(\sigma\ \Sigma\ \Big|\xi\ \Xi\ \Big)P(\Sigma\ \sigma\ ,\Sigma')\,.\end{aligned} \tag{2.33}$$

Note, that in numerical calculations, it is important to consider the order of contractions, as it has a great impact on the program performance.

---

malized as

$$\tilde{A}_{\Sigma\ \sigma\ \Sigma'} = \frac{A_{\Sigma\ \sigma\ \Sigma'}}{\|A_{\Sigma\ \sigma\ \Sigma'}\|}\,,$$

where the norm is

$$\|A_{\Sigma\ \sigma\ \Sigma'}\| = \sqrt{\sum_{\Sigma\ \sigma\ \Sigma'} A^*_{\Sigma\ \sigma\ \Sigma'} A_{\Sigma\ \sigma\ \Sigma'}}\,.$$

The (genuine) density matrix can be then expressed as

$$\rho\Big(\Sigma\ \sigma\ \Big|\Xi\ \xi\ \Big) = \text{Tr}_{\Sigma'}\left[A^*_{\Sigma\ \sigma\ \Sigma'} A_{\Xi\ \xi\ \Sigma'}\right].$$

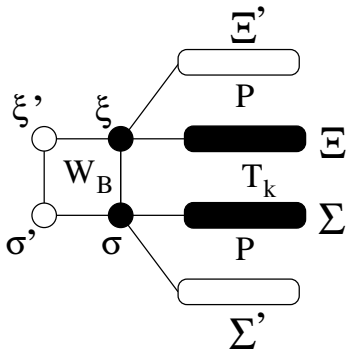

Figure 2.9: Extension and renormalization of the half-row transfer matrix. Here, the new half-row transfer matrix $\mathcal{T}_{k+1}\left(\sigma'\Sigma'\middle|\xi'\Xi'\right)$ is created according to Eq. (2.33).

The new corner transfer matrix is obtained by contracting $\mathcal{W}_{\mathrm{B}}$, C_k and two $\mathcal{T}_k$s (see Fig. 2.10); in particular

$$C_{k+1}\left(\sigma'\Sigma'\middle|\sigma'\Xi'\right) = \sum_{\sigma,\Sigma,\xi,\Xi,\Sigma'',\xi',\Xi''} P\left(\Xi''\xi',\Xi'\right)\mathcal{T}_k\left(\xi\,\Sigma''\middle|\xi'\,\Xi''\right) C_k\left(\xi\,\Xi\,\middle|\xi\,\Sigma''\right)\mathcal{W}_{\mathrm{B}}\left(\sigma'\sigma\,\xi\,\xi'\right) \mathcal{T}_k\left(\sigma\,\Sigma\,\middle|\xi\,\Xi\,\right)P(\Sigma\,\sigma\,,\Sigma')\,. \tag{2.34}$$

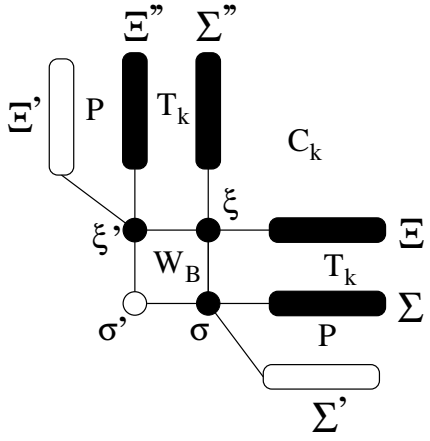

Figure 2.10: Extension and renormalization of the corner transfer matrix. Here, the new corner transfer matrix $C_{k+1}\left(\sigma'\Sigma'|\sigma'\Xi'\right)$ is created according to Eq. (2.34).

The iterative extension procedures in Eqs. (2.33) and (2.34) of $\mathcal{T}_k$ and C_k lead to the divergence of their elements. This has to be addressed by introducing an

appropriate normalization. Division of each element by the norm defined as the absolute value of the largest matrix element proved to be the stable solution. Let us denote the normalization constants of C_k and $\mathcal{T}_k$ as c_k and t_k, respectively. We use the following notation for the normalized tensors

$$\begin{aligned} \widetilde{C}_k &\equiv \frac{C_k}{c_k}, \\ \widetilde{\mathcal{T}}_k &\equiv \frac{\mathcal{T}_k}{t_k}. \end{aligned} \tag{2.35}$$

Free energy calculation Let us denote the number of the spin sites in the k^{th} iterative step on a square lattice as

$$N^{[k]} = (2k+1)^2. \tag{2.36}$$

Thus, the system size extends in the following way: 3×3, 5×5, 7×7, ... The free energy per site is

$$f^{[k]} = -\frac{k_{\mathrm{B}}T}{N^{[k]}} \ln \mathcal{Z}^{[k]} \equiv -\frac{k_{\mathrm{B}}T \ln \mathrm{Tr}\,(C_k)^4}{N^{[k]}}. \tag{2.37}$$

The extension procedure leads to the recurrent relations

$$C_{k+1} = \mathcal{W}_{\mathrm{B}} \mathcal{T}_k^2 C_k, \tag{2.38}$$

$$\mathcal{T}_{k+1} = \mathcal{W}_{\mathrm{B}} \mathcal{T}_k. \tag{2.39}$$

For instance, the explicit expression for the free energy in the third iteration step gives $f^{[3]} = -k_{\mathrm{B}}T \ln \mathrm{Tr}\,(C_3)^4/7^2$, where each of the four central corner tensors C_3 is recursively decomposed into the product of the normalized tensors $\widetilde{C}_2$ and $\widetilde{\mathcal{T}}_2$, which again depend on $\widetilde{C}_1$ and $\widetilde{\mathcal{T}}_1$ according to Eq. (2.38) and Eq. (2.39), respectively. The recurrence relations result in the nested dependence of the normalization factors c_k and t_k. Hence, the decomposition of one of the four normalized corner transfer tensor on the square lattice gives

$$\begin{aligned} \widetilde{C}_3 = \frac{C_3}{c_3} &= \frac{\mathcal{W}_{\mathrm{B}} \widetilde{\mathcal{T}}_2^2 \widetilde{C}_2}{c_3} = \frac{\mathcal{W}_{\mathrm{B}} \mathcal{T}_2^2 C_2}{t_2^2 c_2 c_3} \\ &= \frac{\mathcal{W}_{\mathrm{B}} \left(\mathcal{W}_{\mathrm{B}} \widetilde{\mathcal{T}}_1\right)^2 \left(\mathcal{W}_{\mathrm{B}} \widetilde{\mathcal{T}}_1^2 \widetilde{C}_1\right)}{t_2^2 c_2 c_3} \\ &= \frac{\mathcal{W}_{\mathrm{B}}^4 \mathcal{T}_1^4 C_1}{t_1^4 t_2^2 c_1 c_2 c_3} = \frac{\mathcal{W}_{\mathrm{B}}^9}{t_1^4 t_2^2 t_3^0 c_1^1 c_2^1 c_3^1}, \end{aligned} \tag{2.40}$$

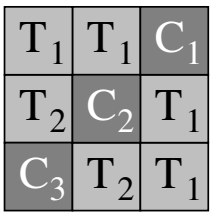

Figure 2.11: Decomposition of the corner transfer matrix C_3, see Eq. (2.40).

and it has the identical graphical representation depicted in Fig. 2.11. Substituting C_3 into Eq. (2.37), we get the explicit expression for the free energy per site when $k = 3$

$$f^{[3]} = -\frac{k_B T}{7^2}\left(\ln \mathrm{Tr}\,\left(\widetilde{C}_3\right)^4 + 4\ln\prod_{j=1}^{3} c_j t_j^{2(3-j)}\right). \tag{2.41}$$

The generalized form of the free energy per site for the arbitrary k, written in terms of the normalization factors of the four central tensors $\widetilde{C}_k$, is

$$f^{[k]} = -k_B T\frac{\ln \mathrm{Tr}\,\left(\widetilde{C}_k\right)^4}{(2k+1)^2} - 4k_B T\frac{\sum_{j=0}^{k-1}\left(\ln c_{k-j} + \ln t_{k-j}^{2j}\right)}{(2k+1)^2}. \tag{2.42}$$

Observables Using the simplified notation, the magnetization in the center of the system can be expressed as

$$M = \langle\sigma_c\rangle = \frac{\mathrm{Tr}\left[\sigma_c C^4\right]}{\mathrm{Tr}\left[C^4\right]}, \tag{2.43}$$

where σ_c is the central spin, see Fig. 2.12a. Equivalently, the magnetization can be evaluated tracing over the density matrix

$$M = \langle\sigma_c\rangle = \sum_{\Sigma\ \sigma_c} \sigma_c\,\rho\left(\Sigma\ \sigma_c\middle|\Sigma\ \sigma_c\right). \tag{2.44}$$

The important technique for obtaining the multi-spin expectation values is the introduction of the additional rows into the system. We demonstrate this technique on s simple case, which is the calculation of the nearest neighbors correlation function $\left\langle\sigma_c\sigma_{c+1}\right\rangle$, see Fig. 2.12b. In the simplified notation, we have

$$\left\langle\sigma_c\sigma_{c+1}\right\rangle = \frac{\mathrm{Tr}\left[\sigma_c\sigma_{c+1}C^4\mathcal{T}^2\right]}{\mathrm{Tr}\left[C^4\mathcal{T}^2\right]}. \tag{2.45}$$

Note, that as the system is infinite, the introduction of the additional row does not change the properties of the system.

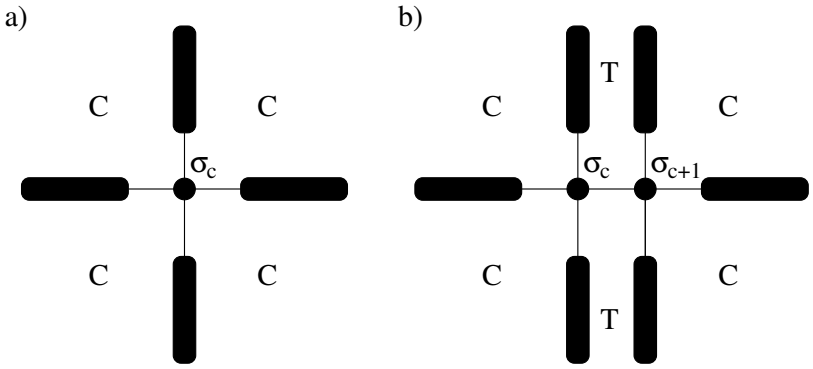

Figure 2.12: Magnetization $\langle\sigma_c\rangle$ and correlation function $\left\langle\sigma_c\sigma_{c+1}\right\rangle$: a) Graphical reprezentation of the calculation of the magnetization $\langle\sigma_c\rangle$ in the center of the system (according to Eq. (2.43)). b) Graphical reprezentation of the calculation of the correlation function $\left\langle\sigma_c\sigma_{c+1}\right\rangle$ (according to Eq. 2.45).

2.3 HOTRG

2.3.1 Tensor-network representation

Tensor-network representation can be employed for any classical statistical system with local (i.e. short-range) interactions. Let us start with the general form of an arbitrary spin Hamiltonian for such a system

$$\mathcal{H} = \sum_{\langle ij\rangle} \mathcal{H}_{\text{local}}\left(\sigma_i, \sigma_j\right), \tag{2.46}$$

where $\langle ij\rangle$ denotes summation over nearest neighbors only, and $\mathcal{H}_{\text{local}}\left(\sigma_i, \sigma_j\right)$ is a local sub-Hamiltonian for (adjacent) spins with states σ_i and σ_j. The partition function can be expressed as

$$\mathcal{Z} = \sum_{\{\sigma\}} \prod_{\langle ij\rangle} \mathcal{W}_{\text{B}}\left(\sigma_i, \sigma_j\right), \tag{2.47}$$

where the sum is taken over all possible spin configurations $\{\sigma\}$, and $\mathcal{W}_{\text{B}}\left(\sigma_i, \sigma_j\right)$ is a Boltzmann weight defined on a bond, i.e., between a corresponding pair of the spins σ_i and σ_j. The Boltzmann weight is defined as

$$\mathcal{W}_{\text{B}}\left(\sigma_i, \sigma_j\right) = \exp\left[-\frac{1}{k_{\text{B}}T}\mathcal{H}_{\text{local}}\left(\sigma_i, \sigma_j\right)\right], \tag{2.48}$$

where k_{B} is the Boltzmann constant and T is the temperature. It is convenient to regard the Boltzmann weight $\mathcal{W}_{\text{B}}$ as a matrix whose row and column indices

are σ_i and σ_j, respectively. Furthermore, as we will demonstrate later on the Ising and Potts models, the bond weight can be re-expressed in terms of a matrix factorization

$$\mathcal{W}_{\mathrm{B}}\left(\sigma_i,\sigma_j\right)=\sum_x W_{\sigma_i x}\ W_{\sigma_j x}\ . \tag{2.49}$$

Finally, this factorization allows us to represent the partition function as a tensor-network state

$$\mathcal{Z}=\mathrm{Tr}\prod_i T_{x_i x_i' y_i y_i'}\,, \tag{2.50}$$

with local tensor T defined at each lattice site as

$$T_{x_i x_i' y_i y_i'}=\sum_\sigma W_{\sigma x_i} W_{\sigma x_i'} W_{\sigma y_i} W_{\sigma y_i'}\,. \tag{2.51}$$

In the following, the tensor-network representations for the Ising and Potts models on a square lattice are introduced. For both the models, symmetric and asymmetric bond factorizations are considered. In this context, the symmetric factorization leads to the local tensors T that are invariant under arbitrary permutations of the indices. The asymmetric factorization is often employed in the tensor network formulations, which do not require any typical symmetry for local weights, as long as the numerical treatment is concerned. In the case of asymmetric factorization, one has to care about the order of the indices in T [2].

Ising model

The Hamiltonian of the Ising model is defined as

$$\mathcal{H}=-J\sum_{\langle ij\rangle}\sigma_i\sigma_j-h\sum_i\sigma_i=-\sum_{\langle ij\rangle}\left[J\sigma_i\sigma_j+\frac{h}{4}\left(\sigma_i+\sigma_j\right)\right], \tag{2.52}$$

where σ takes either $+1$ or -1, $J>0$ represents the ferromagnetic coupling, and h is a constant external magnetic field imposed to each spin. For simplicity, let us consider the case with no external field by setting $h=0$. Accordingly, the local Boltzmann weight (per bond) is given by

$$\mathcal{W}_{\mathrm{B}}\left(\sigma_i,\sigma_j\right)=\exp\left(\frac{J}{k_{\mathrm{B}}T}\sigma_i\sigma_j\right)=e^{K\sigma_i\sigma_j}\,, \tag{2.53}$$

where the parameter $K=J/k_{\mathrm{B}}T$ is introduced.

[2]The symmetry in the local tensors is not always preserved when one performs the renormalization group transformation in the HOTRG method. Thus, for most of the cases, the symmetry is not that important in the numerical calculations.

Symmetric factorization It is possible to factorize the bond weight $e^{K\sigma_i\sigma_j}$ into two parts, by introducing an auxiliary spin $s = \pm 1$, which is often called 'ancilla', and which is located between σ_i and σ_j [Fisher, 1960]. A key relation is

$$e^{K\sigma_i\sigma_j} = \frac{1}{2\left(\cosh 2\overline{K}\right)^{1/2}} \sum_s e^{\overline{K}s(\sigma_i+\sigma_j)}, \tag{2.54}$$

where the right-hand side takes the value $\left(\cosh 2\overline{K}\right)^{1/2}$ when $\sigma_i = \sigma_j$, and $\left(\cosh 2\overline{K}\right)^{-1/2}$ when $\sigma_i \neq \sigma_j$, and where Eq. (2.54) holds under the condition

$$e^K = \left(\cosh 2\overline{K}\right)^{1/2}. \tag{2.55}$$

The new parameter $\overline{K}$ is then expressed as follows

$$e^{\overline{K}} = \sqrt{e^{2K} + \sqrt{e^{4K} - 1}}. \tag{2.56}$$

Thus, we can introduce a factor [3]

$$W_{\sigma s} = \frac{e^{\overline{K}\sigma s}}{\sqrt{2\left(\cosh 2\overline{K}\right)^{1/2}}} \tag{2.57}$$

for each division of a bond, and rewrite the Ising interaction to be of the form of Eq. (2.49).

Asymmetric factorization Instead of using the relation in (2.57), one can introduce an asymmetric decomposition [4]

$$W = \begin{pmatrix} \sqrt{\cosh K}, & \sqrt{\sinh K} \\ \sqrt{\cosh K}, & -\sqrt{\sinh K} \end{pmatrix}. \tag{2.58}$$

[3] In the case with an external field, one can find the factor to be

$$W = \frac{1}{\sqrt{2\left(\cosh 2\overline{K}\right)^{1/2}}} \begin{pmatrix} e^{\Gamma}e^{\overline{K}}, & e^{\Gamma}e^{-\overline{K}} \\ e^{-\Gamma}e^{-\overline{K}}, & -e^{-\Gamma}e^{\overline{K}} \end{pmatrix},$$

where $\Gamma = h/4k_{\mathrm{B}}T$ and we have used the matrix notation for the weight $W_{\sigma s}$.

[4] For a nonzero external magnetic field $h \neq 0$, the factor will change as follows

$$W = \begin{pmatrix} e^{\Gamma}\sqrt{\cosh K}, & e^{\Gamma}\sqrt{\sinh K} \\ e^{-\Gamma}\sqrt{\cosh K}, & -e^{-\Gamma}\sqrt{\sinh K} \end{pmatrix}.$$

Potts model

The Hamiltonian of the Potts model is defined as

$$\begin{aligned}\mathcal{H} &= -J\sum_{\langle ij\rangle}\delta\left(\sigma_i,\sigma_j\right)-h\sum_i\delta\left(\sigma_i,\sigma_h\right) \\ &= -\sum_{\langle ij\rangle}\left\{J\delta\left(\sigma_i,\sigma_j\right)+\frac{h}{4}\left[\delta\left(\sigma_i,\sigma_h\right)+\delta\left(\sigma_j,\sigma_h\right)\right]\right\},\end{aligned} \tag{2.59}$$

where σ takes values $\sigma = 1,2,3,...,q$ for a fixed number q, σ_h is a fixed state chosen for the purpose of a field coupling. Notice also that δ is the Kronecker delta

$$\delta\left(\sigma_i,\sigma_j\right)=\begin{cases}0 & \text{if } \sigma_i \neq \sigma_j\,,\\ 1 & \text{if } \sigma_i = \sigma_j\,.\end{cases} \tag{2.60}$$

For simplicity, let us start with the case with no external field, i.e. when $h = 0$. Thus, we can write for the Boltzmann weight

$$e^{K\delta(\sigma_i,\sigma_j)}=\begin{cases}1 & \text{if } \sigma_i \neq \sigma_j\,,\\ e^K & \text{if } \sigma_i = \sigma_j\,.\end{cases} \tag{2.61}$$

Symmetric factorization By introducing an auxiliary spin $s = 1,2,...q$, we obtain a key relation

$$\sum_s \exp\left[\overline{K}\left\{\delta(\sigma_i,s\,)+\delta(\sigma_i,s\,)\right\}\right]=\begin{cases}q-2+2e^{\overline{K}} & \text{if } \sigma_i \neq \sigma_j\,,\\ q-1+e^{2\overline{K}} & \text{if } \sigma_i = \sigma_j\,.\end{cases} \tag{2.62}$$

In order to make the expression for the Boltzmann weight in Eq. (2.61) consistent with Eq. (2.62), one must impose the condition

$$e^{-K}=\frac{q-2+2e^{\overline{K}}}{q-1+e^{\overline{K}}}\,. \tag{2.63}$$

By inverting the last equation, one obtains the following relation for $\overline{K}$

$$e^{\overline{K}}=e^K+\sqrt{(e^K+q-1)(e^K-1)}\,. \tag{2.64}$$

Thus, the Boltzmann weight can be decomposed in terms of a factor [5]

$$W_{\sigma s} = \frac{e^{\overline{K}\delta(\sigma,s)}}{\sqrt{q-2+2e^{\overline{K}}}}. \tag{2.65}$$

Asymmetric (numerical) factorization In this case, asymmetric factorization can be performed numerically by simple matrix diagonalization

$$\mathcal{W}_{\mathrm{B}} = P\, DP^{-1} = \underbrace{\left(P\sqrt{D}\right)}_{W}\underbrace{\left(P\sqrt{D}\right)^{\mathsf{T}}}_{W^{\mathsf{T}}}, \tag{2.66}$$

in particular,

$$\mathcal{W}_{\mathrm{B}}\left(\sigma_i,\sigma_j\right) = \sum_{xy} P_{\sigma_i x} D_{xy} P^{-1}_{y\sigma_j} = \sum_{x} \underbrace{\left(\sum_{m} P_{\sigma_i m}\sqrt{D_{mx}}\right)}_{W_{\sigma_i x}} \underbrace{\left(\sum_{n}\sqrt{D_{xn}} P_{n\sigma_j}\right)^{\mathsf{T}}}_{W^{\mathsf{T}}_{x\sigma_j}}. \tag{2.67}$$

2.3.2 Coarse-graining procedure

A simple yet powerful iterative way of calculating the partition function is the coarse-graining renormalization procedure [Xie et al., 2012]. The lattice is contracted alternatively along the horizontal (x axis) and vertical (y axis) directions. At each iterative step, a new tensor $T^{(n+1)}$ is created from two preceding tensors $T^{(n)}$, i.e., two tensors $T^{(n)}$ are contracted and renormalized along the y (x) axis. Subsequently, the resulted tensor is contracted and renormalized along the x (y) axis. By each contraction, the lattice size is effectively reduced by a factor of two. This procedure is iterative and is terminated when desired observables have converged, i.e., reached a fixed point. This Subsection contains a step-by-step description of the coarse-graining procedure.

First, by contracting the two tensors $T^{(n)}$ along the y axis, we define

$$M^{(n)}_{xx'yy'} = \sum_{i} T^{(n)}_{x_1 x'_1 y\ i}\ T^{(n)}_{x_2 x'_2 i\ y}\ , \tag{2.68}$$

[5] For a nonzero external magnetic field $h \neq 0$, one can find the factor to be

$$W_{\sigma s} = \frac{e^{\overline{K}\delta(\sigma,s)} e^{\Gamma\delta(\sigma,\sigma_h)}}{\sqrt{q-2+2e^{\overline{K}}}}.$$

Notice that Γ here is not rescaled, whereas the rescaled $\overline{K}$ is used in this formula.

where $x = x_1 \otimes x_2$ and $x' = x'_1 \otimes x'_2$, and the superscript n denotes the n^{th} iteration. To truncate the tensor $M^{(n)}$ by Higher-Order Singular Value Decomposition (HOSVD) [de Lathauwer et al., 2000], two matrix unfoldings are prepared

$$M_{(1)x,x'yy'} = M_{xx'yy'}\,, \tag{2.69}$$

and

$$M_{(2)x',yy'x} = M_{xx'yy'}\,. \tag{2.70}$$

Then, a SVD for this two matrices is performed

$$M_{(1)} = U_{(1)}\Sigma_{(1)}V^{\dagger}_{(1)}\,, \tag{2.71}$$

$$M_{(2)} = U_{(2)}\Sigma_{(2)}V^{\dagger}_{(2)}\,, \tag{2.72}$$

where $U_{(1)}$, $V_{(1)}$, $U_{(2)}$, and $V_{(2)}$ are unitary matrices of respective dimensions, and $\Sigma_{(1)}$ and $\Sigma_{(2)}$ are diagonal matrices with singular values on their diagonals

$$\Sigma_{(.)} = \mathrm{diag}(\sigma_{(.)1}, \sigma_{(.)2}, \dots)\,. \tag{2.73}$$

The singular values are ordered in decreasing order by convention. To obtain the optimal approximation of the tensor $M^{(n)}$, two errors

$$\varepsilon_1 = \sum_{i>D} \sigma^2_{(1)i}\,, \tag{2.74}$$

and

$$\varepsilon_2 = \sum_{i>D} \sigma^2_{(2)i}\,, \tag{2.75}$$

are calculated and compared, whereas D is the maximal truncated tensor dimension. If $\varepsilon_1 < \varepsilon_2$, we truncate the second dimension of $U_{(1)}$ and set $U = U_{(1)}$. Otherwise, we truncate the second dimension of $U_{(2)}$ and set $U = U_{(2)}$.

After the truncation, we can create a new tensor

$$T^{(n+1)}_{xx'yy'} = \sum_{ij} U^{(n)}_{ix} M^{(n)}_{ijyy'} U^{(n)}_{jx'}\,. \tag{2.76}$$

The contraction and renormalization along the x axis are performed in a similar way. By the contraction of the two tensors $T^{(n)}$ along the x axis, we define

$$M^{(n)}_{xx'yy'} = \sum_{i} T^{(n)}_{xiy_1y'_1} T^{(n)}_{ix'y_2y'_2}\,, \tag{2.77}$$

where $y = y_1 \otimes y_2$ and $y' = y'_1 \otimes y'_2$. Next, the following matrix unfoldings are prepared

$$M_{(3)y,y'xx'} = M_{xx'yy'}\,, \tag{2.78}$$

$$M_{(4)y',xx'y} = M_{xx'yy'}\,, \tag{2.79}$$

on which the SVD is performed. As before, the two errors are compared and the chosen unitary matrix is truncated and set to U. Finally, we define a new contracted tensor of the consequent iterative step $(n+1)$ as

$$T^{(n+1)}_{xx'yy'} = \sum_{kl} U^{(n)}_{ky} M^{(n)}_{xx'kl} U^{(n)}_{ly'}\,. \tag{2.80}$$

The identification of the two truncation errors ε_1 and ε_2 is not always necessary. Indeed, for the Ising model, the two errors are equal, i.e., $\varepsilon_1 = \varepsilon_2$ [Ueda et al., 2014]. However, when dealing with models without translational symmetry, e. g. spin glass models [Wang et al., 2013a], then the two errors differ, and because of that, it is important to identify them.

2.3.3 Free energy calculation

In practical calculations, the tensors are renormalized after each coarse-graining step, otherwise the tensor elements become infeasibly large. This can be done in many different ways. In our calculations, we define a norm as the absolute value of the largest element of the tensor and the new renormalized tensor is obtained by dividing each element by the norm. The algorithm is started with an initial tensor $T^{(0)}$; after the first coarse-graining, the norm λ_1 and renormalized tensor $T^{(1)}$ are obtained. In order to calculate the free energy, we need to keep track of all the normalization coefficients $(\lambda_1, \lambda_2, ..., \lambda_n)$, as well as the final renormalized tensor $T^{(n)}$. Thus, after n iteration steps, the partition function can be expressed as

$$\begin{aligned}
\mathcal{Z}_n &= \mathrm{Tr}\{\underbrace{T^{(0)}T^{(0)}T^{(0)}\cdots T^{(0)}}_{N}\} \\
&= \lambda_1^{N/2}\mathrm{Tr}\{\underbrace{T^{(1)}T^{(1)}T^{(1)}\cdots T^{(1)}}_{N/2}\} \\
&\vdots \\
&= \lambda_1^{N/2}\lambda_2^{N/4}\cdots\lambda_n^{N/2^n}\mathrm{Tr}\left\{T^{(n)}\right\},
\end{aligned} \tag{2.81}$$

where $N = 2^n$ is the system size. The notion of the tensor trace depends on the boundary conditions; in our numerical considerations we employed the periodic boundary conditions

$$\mathrm{Tr}\{T^{(n)}\} = \sum_{xy} T^{(n)}_{xxyy}\,. \tag{2.82}$$

Recall that the free energy (per site) is defined as

$$f_n = -\frac{k_\mathrm{B}T}{N}\log\mathcal{Z}_n\,. \tag{2.83}$$

and it can easily be expressed as

$$f_n = -k_B T \left[\sum_{i=1}^{n} \frac{1}{2^i} \log \lambda_i + \frac{\log \mathrm{Tr}\{T^{(n)}\}}{2^n} \right]. \tag{2.84}$$

After sufficient number of iterations (usually around $n \sim 40$), the trace of $T^{(n)}$ converges to a finite number and as the number of sites 2^n increases, the second term in the Eq. (2.84) becomes negligible .

2.3.4 Impurity tensors

Magnetization The spontaneous magnetization per site can be obtained by inserting a σ-dependent local tensor into the system. For the Ising model, we have

$$\tilde{T}_{x_i x_i' y_i y_i'} = \sum_{\sigma} \sigma W_{\sigma x_i} W_{\sigma x_i'} W_{\sigma y_i} W_{\sigma y_i'}, \tag{2.85}$$

whereas for the Potts model we have

$$\tilde{T}^{\sigma_0}_{x_i x_i' y_i y_i'} = \sum_{\sigma} \delta(\sigma_0, \sigma) W_{\sigma x_i} W_{\sigma x_i'} W_{\sigma y_i} W_{\sigma y_i'}. \tag{2.86}$$

Notice that for the Potts model, the magnetization is measured in the direction of a fixed spin state σ_0.

In practical terms, after the impurity tensor initialization (Eqs. (2.85) and (2.86)), the impurity tensors are contracted with the local tensors

$$\begin{aligned} \tilde{T}^{(1)} &= \tilde{T}^{(0)} * T^{(0)}, \\ \tilde{T}^{(2)} &= \tilde{T}^{(1)} * T^{(1)}, \\ &\vdots \\ \tilde{T}^{(n)} &= \tilde{T}^{(n-1)} * T^{(n-1)}. \end{aligned} \tag{2.87}$$

In the contractions, there is no need to perform separate HOSVDs; the unitaries obtained in the process of the creation of the local tensors $T^{(n)}$ are sufficient. The impurity tensors are renormalized at each step by the corresponding norms of the local tensors, i.e., $\tilde{T}^{(1)}$ by λ_1, $\tilde{T}^{(2)}$ by λ_2, etc. Notice also, that the impurity can be kept in the middle of the system by rotating the tensors after each coarse-graining iterative step. This is important since the magnetization can be dependent on the location of the observation site.

The magnetization is calculated as

$$M = \frac{\mathrm{Tr}\left\{\tilde{T}^{(n)}\right\}}{\mathrm{Tr}\left\{T^{(n)}\right\}}. \tag{2.88}$$

For Potts the magnetization is rescaled as

$$M' = \frac{qM - 1}{q - 1}. \tag{2.89}$$

2.3.5 Numerical results

Let us first compare the relative errors of the free energy to the rigorous solution [Onsager, 1944] for the two-dimensional Ising model for $D = \{4, 6, 16\}$, see Fig. 2.13. For $D = 16$, we obtained the relative error of the free energy at the critical temperature T_c of an order of 10^{-6}.

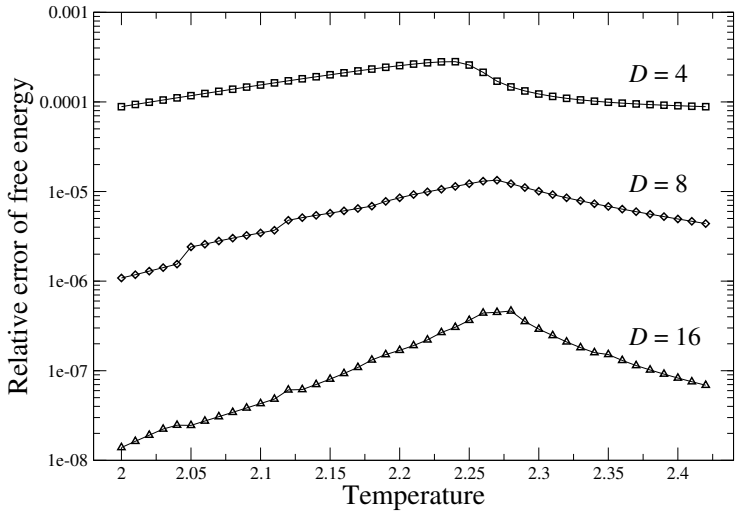

Figure 2.13: Comparison of the relative errors of the free energy with respect to the exact results for the square-lattice Ising model for $D = \{4, 8, 16\}$. The critical temperature is $T_c = 2/\ln\left(1 + \sqrt{2}\right) \approx 2.269$.

The comparison of the spontaneous magnetization obtained numerically (using the impurity tensor) for $D = 16$ with respect to the exact solution [Onsager, 1944] can be found in Fig. 2.14. The relative error of the spontaneous magnetization below the critical temperature T_c is plotted in the inset. The numerical calculations yielded the spontaneous magnetization above the critical temperature T_c of order of 10^{-9} (at $T = 2.270$) which further gradually decreases with increasing temperature T.

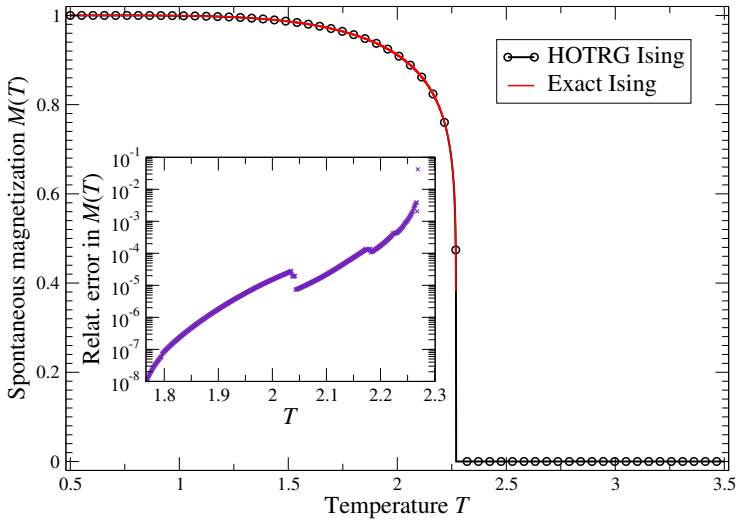

Figure 2.14: Temperature dependence of the spontaneous magnetization for the square-lattice Ising model ($D = 16$). Inset: relative error of the spontaneous magnetization with respect to the rigorous solution below the critical temperature $T_c \approx 2.269$.

Chapter 3

Free energy on hyperbolic geometries

In this Chapter, we investigate relations between spatial properties of the free energy and the radius of Gaussian curvature of the underlying curved lattice geometries. For this purpose we derive recurrence relations for the analysis of the free energy normalized per lattice site of various multi-state spin models in the thermal equilibrium on distinct non-Euclidean surface lattices of the infinite sizes. Whereas the free energy is calculated numerically by means of the CTMRG algorithm (see the introduction to square-lattice CTMRG in the Section 2.2), the radius of curvature has an analytic expression. Two tasks are considered in this work. First, we search for such a lattice geometry, which minimizes the free energy per site. We conjecture that the only Euclidean flat geometry results in the minimal free energy per site regardless of the spin model. Second, the relations among the free energy, the radius of curvature, and the phase transition temperatures are analyzed. We found out that both the free energy and the phase transition temperature inherit the structure of the lattice geometry and reproduce the properties of the Gaussian radius of curvature. It is a unique achievement, which opens new perspectives in the AdS/CFT correspondence theories.

3.1 Introduction

The thermodynamic properties and the phase transition phenomena of various physical systems on two-dimensional non-Euclidean surfaces have attracted the attention of many theorists and experimentalists for a couple of decades. Especially, the studies of the hyperbolic surfaces, i.e. the negatively curved geometry, exhibit the increasing interest in theoretical research of quantum gravity, where the anti-de Sitter (AdS) hyperbolic spatial geometry plays its essential role. Thus, the

mutual interplay among the condensed matter physics, general theory of relativity, and conformal field theory (CFT) enriches the interdisciplinary research [Maldacena, 1998, Maldacena, 1999]. Among them, let us mention experiments on magnetic nanostructures [Yoshikawa et al., 2004, Liang et al., 2006, Cabot et al., 2009], on soft materials of a conical geometry [Moura-Melo et al., 2007], lattice dislocations of the solid-state crystals, quantum gravity [Kazakov, 1986, Holm and Janke, 1996], complex networks [Krioukov et al., 2009, Krioukov et al., 2010], where neural networks with the non-Euclidean geometry belong to as well.

A typical theoretical example of such a hyperbolic surface geometry is a two-dimensional discretized hyperbolic lattice with a constant negative Gaussian curvature. We consider an infinite set of such hyperbolic lattices constructed by the regular tessellation of congruent polygons, which are connected without empty spaces at the lattice sites (the vertices) with a fixed coordination number. The hyperbolic lattices of finite sizes are characteristic for their enormous number of the boundary sites. The number of the boundary sites is always larger than the remaining number of all the inner sites. Or, equivalently, if one gradually increases the size of a hyperbolic lattice by regular adding the outermost layers, the total number of the (boundary) sites increases exponentially with respect to the increasing radius of the lattice. Since we also intend to determine the phase transitions of various multi-spin Hamiltonians on the hyperbolic lattices, an accurate numerical algorithm has to be used, which is also capable of treating the models in the thermodynamic limit, where the perimeter of the lattice (the size) is infinite. Such a condition makes the spin systems extremely difficult to be treated numerically on the hyperbolic lattice geometries (in general, these systems are not integrable). Therefore, neither the transfer matrix diagonalization methods are numerically feasible (due to a non-trivial way of the transfer matrix construction) nor the Monte Carlo simulations are completely reliable (due to the insufficiency of the finite-size scaling near phase transitions).

An RG-based algorithm was proposed [Ueda et al., 2007], which generalizes the CTMRG method [Nishino and Okunishi, 1996, Nishino and Okunishi, 1997]. So far, the method was applied to study Ising-like systems on certain types of the hyperbolic lattices, where either the lattice coordination number was fixed letting the polygons to vary [Krcmar et al., 2008] or the polygons were fixed to be triangles and the coordination number was varied [Gendiar et al., 2012]. In the present work we expand the mentioned studies to multi-state spin Hamiltonians on a much broader set of the hyperbolic lattices so that both the coordination number q and the number of the sides p in the polygons can vary. We describe a unique way of how to derive generalized recurrence relations for such lattices by the CTMRG algorithm, which enable us to study phase transitions of the M-state clock and M-state Potts spin models ($M \geq 2$) on any lattice geometries for arbitrary polygon number $p \geq 4$ and for an independent coordination number $q \geq 4$.

A particular attention is focused on the analytic derivation of the free energy per spin site via the calculation of the normalized partition function by CTMRG. The free energy per site is a well-conditioned thermodynamic function, which does not diverge in the thermodynamic limit. The numerical calculation of the free energy by CTMRG reaches a high accuracy; as it will be evident from singular behavior of the specific heat at a phase transition even after taking the second derivative of the free energy with respect to temperature numerically. (Notice that Monte Carlo simulations are inefficient in evaluating the free energy due to large numerical fluctuations). The free energy analysis has never been considered in any non-Euclidean systems yet.

Hence, the current numerical analysis may serve as an appropriate, accurate, as well as complementary source of information for the non-integrable spin systems. The determination of the phase transition point can be derived, for instance, from the specific heat, which exhibits non-analytic behavior at a phase transition. The free energy naturally contains an important information, which reflects a rich boundary structure of the underlying lattice. In the case of considering the single-site expectation values, such as the spontaneous magnetization (measured in the lattice center only), the boundary effects are always negligibly small, and the results are in full agreement with the known exact solution for the Ising model on the Bethe lattice. As we show later, having considered the boundary effects, the phase transition is completely suppressed and can be restored by an appropriate redefinition of the free energy. The correctness of the present numerical calculations is compared with the exact solutions of the phase transition in the Ising model on various types of Bethe lattices [Baxter, 1982].

One can reverse the order of considerations and put another non-trivial question, which we intend to answer in the current study. The question is associated with a particular interest in the AdS/CFT correspondence, the so-called gauge duality [Maldacena, 1998, Maldacena, 1999]. A highly complicated boundary structure of a finite hyperbolic anti-de Sitter space (locally viewed as a Minkovski-like space) can be regarded as a spacetime for the conformal field theory (being identical to a gravitational theory). Our work is focused on the features of the complex boundary structures only, and no time evolution has been considered. A simple physical model with a spin-spin interaction network can be used to form a regular hyperbolic (AdS) space, which can be analyzed with sufficient accuracy. So far, there has been neither theoretical nor numerical study aimed for the free energy analysis of the AdS spaces. However, we have succeeded and gradually developed a way of the free energy analysis of such non-Euclidean systems. A condensed-matter point of view on the AdS/CFT correspondence can undergo defficulties, one of them being the problem of a prefered coordinate system, i.e. a lattice [Anderson, 2013]. For simplicity, we have chosen an infnite set of two-dimensional curved hyperbolic surfaces (AdS spaces), where the underlying lattice geometry

is not fixed at all, but can vary by changing two integer lattice parameters p and q. We intend to investigate how the (p,q) geometry impacts on the total free energy (including the phase transitions) so that the boundary effects are fully incorporated in the process.

Another question is related to a more concrete physical problem, where we consider an M-state spin Hamiltonian defined on all possible infinite-sized lattice geometries (p,q). The spin network is formed in such a way that we allow each multi-state spin to interact with q nearest-neighboring spins only with a constant interaction coupling set to the unity. It results in hyperbolic geometries of various Gaussian curvatures. The free energy study of the multi-state spin systems for the classical spin system can be also generalized to the ground-state energy study for the quantum spin system, as we mention later. We also answer the question, which of the (p,q) lattice geometries can minimizes the free energy per site.

This Chapter is organized as follows. In Section 3.2 we briefly define the regular (p,q) lattice geometries for the M-state spin clock and Potts Hamiltonians. The recurrence relations for the CTMRG algorithm are derived gradually starting from three simplest cases: $(4,4)$ (already explained in Section 2.2)), $(5,4)$, and $(4,5)$. A detailed graphical representation of the recurrence relations is given. Once the recurrence relations are defined, we check the correctness of the CTMRG algorithm in Section 3.3 by calculating the phase transitions of the simple Ising model on sequences of selected (p,q) lattices. We also approach the asymptotic lattice geometries $(\infty,7)$, $(7,\infty)$, and (∞,∞). The numerical accuracy of the phase transition points is compared with the only exactly solvable model: it is the Ising model on the Bethe lattices. The lowest numerical accuracy of the models occurs at the phase transition temperature with its relative error as small as 10^{-5}. The analytic derivation of the free energy per site for arbitrary (p,q) is given in Section 3.4. The numerical results are studied in Section 3.5, where the phase transitions of the multi-state spin models on the (p,q) lattice geometries are calculated by the free energy per site and the related specific heat. We define the *bulk* free energy to get the correct information on the phase transition, where the boundaries effects are suppressed. The two-dimensional surface profile of the free energy per spin site with respect to the geometry parameters p and q is obtained at the final stage. A unique relation between the surface profile of the free energy per site and the analytical radius of the Gaussian curvature is proposed in the large p,q limit. We conjecture that the free energy per site can reproduce the geometrical structure of spin interactions, which is responsible for the lattice geometry. Moreover, we found out that the phase transition temperatures also copy the underlying lattice geometry.

3.2 Hyperbolic CTMRG

The idea of replacing the standard transfer matrix formulation of classical spin systems by the alternative corner transfer matrix method originates in Baxter's proposal of treating spin Hamiltonians [Baxter, 1982]. The reformulation of Baxter's analytical study into the numerical CTMRG algorithm was first performed by Nishino and Okunishi [Nishino and Okunishi, 1996, Nishino and Okunishi, 1997], who combined the corner transfer matrix formalism with the numerically effective Density Matrix Renormalization Group method [White, 1992]. In 2007, the CTMRG algorithm was generalized and applied to the Ising model on the pentagonal hyperbolic lattice with the constant coordination number four [Ueda et al., 2007].

The essence of the CTMRG algorithm rests in finding the recurrence relations, which are used for the extension of the corner transfer matrices. Before we propose a unified CTMRG algorithm for any classical spin system on the hyperbolic lattice surfaces, we describe the lattice geometry that is gradually built up by polygons. Let the lattice be made by the regular polygonal tessellation with the constant coordination number. Each lattice geometry is characterized by the Schläfli symbol (p,q), where p is associated with the regular polygon of p sides (the p-gon in the following) with the constant coordination number q.

There are three possible scenarios of creating the lattice geometry (p,q) for the integers $p > 2$ and $q > 2$. (1) The condition $(p-2)(q-2) = 4$ gives rise to the two-dimensional Euclidean flat geometry. In this study, we consider only the square lattice $(4,4)$, which satisfies the condition, and the remaining triangular $(3,6)$ and honeycomb $(6,3)$ Euclidean lattices will be studied elsewhere. (2) If $(p-2)(q-2) > 4$, the infinite set of the hyperbolic geometries can satisfy the condition. Although such lattices of infinite size define various two-dimensional curved surfaces, the entire infinite hyperbolic lattice can be spanned in the infinite-dimensional space only; it is commonly associated with the Hausdorff dimension which is infinite. None of the hyperbolic lattices can be endowed in the three-dimensional space. (3) The condition $(p-2)(q-2) < 4$ corresponds to only five finite-sized spherically curved geometries, which are trivial and are not considered in the current study.

The renormalization procedure in square lattice CTMRG described in Section 2.2 can be straightforwardly adapted to the case of the hyperbolic lattices. However, the substantial difference is when the coordination number q is odd. This leads to the asymmetric density matrix

$$\rho = C^q . \tag{3.1}$$

Simply speaking, when q is odd (i.e., $q = 2k+1$, for $k = 1,2,\dots$), we cannot divide the system into two equal parts (with the same number of corners). This can be

solved by introducing the symmetrized density matrix [Schollwöck, 2005, Gendiar et al., 2012]

$$\rho\Big(\Sigma\ \sigma\ \Big|\Xi\ \xi\ \Big)=\frac{1}{2}\sum_{\Sigma'}\Big[A\Big(\sigma\ \Sigma'\Big|\sigma\ \Sigma\ \Big)B\Big(\xi\ \Sigma'\Big|\xi\ \Xi\ \Big)+B\Big(\sigma\ \Sigma'\Big|\sigma\ \Sigma\ \Big)A\Big(\xi\ \Sigma'\Big|\xi\ \Xi\ \Big)\Big]\,. \tag{3.2}$$

where $A = C^k$ represents the statistical weight of the smaller part and $B = C^{k+1}$ represents the statistical weight of the larger part of the system (compare to the Eq. (2.31)).

3.2.1 The Lattice Model

Each vertex of the infinite (p,q) lattice, built up by the p-gons with the fixed coordination number q, represents a classical multi-spin variable σ interacting with the q nearest-neighboring spins. The Hamiltonian $\mathcal{H}_{(p,q)}$ can be decomposed into the sum of identical local Hamiltonians $\mathcal{H}_p$ acting exclusively on the local p-gons, which are considered to be the basic elements in the construction of the entire lattice. In particular, the decomposition of the full Hamiltonian is

$$\mathcal{H}_{(p,q)}\{\sigma\} = \sum_{(p,q)} \mathcal{H}_p[\sigma], \tag{3.3}$$

where the sum is taken through the given lattice geometry (p,q) accordingly. The simplified spin notations $[\sigma]$ and $\{\sigma\}$, respectively, are ascribed to the p spins within each local Hamiltonian $\mathcal{H}_p[\sigma] \equiv \mathcal{H}_p(\sigma_1\sigma_2\cdots\sigma_p)$ and the infinitely many spins $\{\sigma\}$ of the entire system $\mathcal{H}_{(p,q)}\{\sigma\} \equiv \mathcal{H}_{(p,q)}(\sigma_1\sigma_2\cdots\sigma_\infty)$. We consider two types of the multi-state spin models: the M-state clock model with the local Hamiltonian

$$\mathcal{H}_p[\sigma] = -J\sum_{i=1}^{p}\cos\left[\frac{2\pi}{M}(\sigma_i-\sigma_{i+1})\right] \tag{3.4}$$

and the M-state Potts model

$$\mathcal{H}_p[\sigma] = -J\sum_{i=1}^{p}\delta_{\sigma_i,\sigma_{i+1}}\,, \tag{3.5}$$

where $\sigma_{p+1} \equiv \sigma_1$ within the p-gon, and where each M-state spin variables $\sigma = 0,1,2,\ldots,M-1$. (Thus, the Ising model is associated with $M = 2$.) We consider the ferromagnetic interaction $J > 0$ to avoid frustration.

Let the Boltzmann weight $\mathcal{W}_{\mathrm{B}}[\sigma] = \exp(-\mathcal{H}_p[\sigma]/k_{\mathrm{B}}T)$ be defined on the p-gon of the local Hamiltonian, where k_{B} and T correspond to the Boltzmann constant and temperature, respectively. We use the dimensionless units throughout this work and set $J = k_{\mathrm{B}} = 1$.

In general, the Ising model on the hyperbolic lattices (p,q) is not exactly solvable, except for special asymptotic cases, on the Bethe lattices, as discussed later. We employ the CTMRG algorithm as a powerful tool to study the phase transitions numerically on the arbitrary lattice geometries (p,q). We check the correctness and accuracy of the results by comparing the phase transition temperatures with the exactly solvable Ising model on the Bethe lattices [Baxter, 1982].

The CTMRG algorithm is an RG-based iterative numerical method, which enables to evaluate the partition function $\mathcal{Z}$ and the thermodynamic functions within high accuracy [Genzor et al., 2015]. Let each CTMRG iteration steps be enumerated by an integer variable k. At the very beginning of the iterative process, the lattice size with the (p,q) geometry is as small as the size of q p-gons, and is referred to as the first iteration step with $k = 1$. In the second iteration step, $k = 2$, the lattice can expand its size either as a power law (only for the Euclidean square $(4,4)$ lattice) or it grows exponentially (for all the remaining (p,q) hyperbolic cases). The lattice size expands with respect to the number of the Boltzmann weights (or, equivalently, with respect to the total number of the spin sites). Since we are interested in the phase transition studies, the thermodynamic limit requires to take $k \to \infty$, which is equivalent to the case when the iterative process proceeds until all of the thermodynamic functions (normalized to the spin site) converge completely.

3.2.2 Recurrence Relations

The complete expansion (iteration) process is given by recurrence relations as we specify below. For the more instructive understanding, the derivation of the recurrence relations is structured into the following three steps

(i) $(4,4)$, $(5,4)$, and $(4,5)$,

(ii) $(4,4) \to (5,4) \to (6,4) \to \cdots \to (\infty,4)$,

(iii) (p,q).

Figure 3.1 depicts three typical lattices in the first two iteration steps ($k = 1$ and $k = 2$). The shaded p-gons represent the corresponding finite lattice made of the Boltzmann weights $\mathcal{W}_{\mathrm{B}}$ at given k. The surrounded p-gons shown in white color around the shaded ones stand for the consequent iteration steps. The spin variables σ are positioned on the vertices of the polygons, and the sides of the p-gons correspond to the constant nearest-neighbor spin coupling $J = 1$. Notice that the sizes and the shapes of the polygons are kept equal for each lattice geometry (p,q), and we display each hyperbolic lattice geometry in the Poincare disk representation [Anderson, 2005], which projects the entire hyperbolic lattice onto

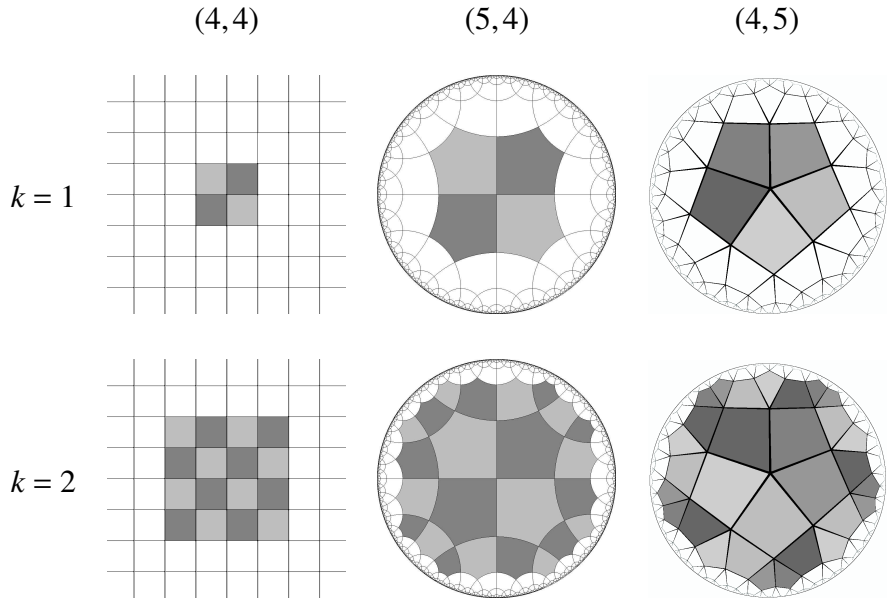

Figure 3.1: The illustration of the three selected lattice geometries (4,4), (5,4), and (4,5). The first two CTMRG iteration steps $k = 1$ (upper) and $k = 2$ (lower) show the building process of the lattices by means of the p-gonal Boltzmann weight tessellation with the uniform coordination number q. The Boltzmann weights for given k are represented by the shaded regular (congruent) p-gons.

the shown unitary circles. As the consequence of that projection, the sizes of the p-gons get deformed and shrunk from the lattice center toward the circumference of the circle. The circumference is associated with the lattice boundary in the infinity.

(i) The iterative expansion process is formulated in terms of the generalized corner transfer matrix notation (for details, see Refs. [Ueda et al., 2007, Krcmar et al., 2008, Gendiar et al., 2012, Gendiar et al., 2014]), where the corner transfer tensors C_j and the transfer tensors $\mathcal{T}_j$ expand their sizes as the iteration step (indexed by j) increases, i.e. $j = 1,2,3,\ldots,k$

$$\left.\begin{aligned} C_{j+1} &= \mathcal{W}_{\mathrm{B}}\mathcal{T}_j^2 C_j \\ \mathcal{T}_{j+1} &= \mathcal{W}_{\mathrm{B}}\mathcal{T}_j \end{aligned}\right\} \text{ for } (4,4), \tag{3.6}$$

$$\left.\begin{aligned} C_{j+1} &= \mathcal{W}_{\mathrm{B}}\mathcal{T}_j^3 C_j^2 \\ \mathcal{T}_{j+1} &= \mathcal{W}_{\mathrm{B}}\mathcal{T}_j^2 C_j \end{aligned}\right\} \text{ for } (5,4), \tag{3.7}$$

$$\left.\begin{aligned} C_{j+1} &= \mathcal{W}_{\mathrm{B}}\mathcal{T}_j^2 C_j^3 \\ \mathcal{T}_{j+1} &= \mathcal{W}_{\mathrm{B}}\mathcal{T}_j C_j \end{aligned}\right\} \text{ for } (4,5). \tag{3.8}$$

The tensors are initialized to the Boltzmann weight and $C_1 = \mathcal{T}_1 \equiv \mathcal{W}_{\mathrm{B}}$.

The recurrence relations in Eqs. (3.6)-(3.8) are written in a simplified form, it means we excluded the indexing of the lattice geometry (p,q) they depend on. Hence, we omit the lattice superscript so that $C_j^{(p,q)} \to C_j$ and $\mathcal{T}_j^{(p,q)} \to \mathcal{T}_j$. The partition function, $\mathcal{Z}_{(p,q)}^{[k]}$, in the final k^{th} iteration step is given by the configuration sum (or, equivalently, by the trace) of the product of the q corner transfer tensors, which are concentrically connected around the central spin site of the lattice [Ueda et al., 2007]

$$\mathcal{Z}_{(p,q)}^{[k]} = \mathrm{Tr}\left[e^{-\mathcal{H}_{(p,q)}/T}\right] = \mathrm{Tr}\,(\underbrace{C_k C_k \cdots C_k}_{q}) \equiv \mathrm{Tr}\,(C_k)^q. \tag{3.9}$$

The evaluation of the partition function via the product of the Boltzmann weights of the p-gonal shape can be also expressed graphically, which may serve as a visual simplification of Eq. (3.9). For instance, the size of the square lattice $(4,4)$ in the second iteration step, $k = 2$, corresponds to the evaluation of the partition function $\mathcal{Z}_{(4,4)}^{[k=2]}$. This is equivalent to the product of the sixteen Boltzmann weights in accord with the respective lattice shown in Fig. 3.1, i.e.,

$$\mathcal{Z}_{(4,4)}^{[2]} = \mathrm{Tr}\,(C_2)^4 = \mathrm{Tr}\left(\mathcal{W}_{\mathrm{B}}\mathcal{T}_1^2 C_1\right)^4 = \mathrm{Tr}\,(\mathcal{W}_{\mathrm{B}})^{16}. \tag{3.10}$$

Thus, the power of $\mathcal{W}_{\mathrm{B}}$ matches the total number of the shaded squares in Fig. 3.1 for given k. The number of the square-shaped Boltzmann weights obeys the power law $4k^2$ being the number of the squares on the $(4,4)$ lattice for given k.

The partition functions of the two hyperbolic lattices $(5,4)$ and $(4,5)$, as selected within (i), are evaluated analogously. The lattice size in the second iteration step, $k = 2$, is graphically sketched in Fig. 3.1 and is related to taking the configuration sum over the product of the shaded p-gons. For the instructive purpose, the two respective partition functions for $k = 2$ satisfy the expressions

$$\mathcal{Z}_{(5,4)}^{[2]} = \mathrm{Tr}\,(C_2)^4 = \mathrm{Tr}\left(\mathcal{W}_{\mathrm{B}}\mathcal{T}_1^3 C_1^2\right)^4 = \mathrm{Tr}\,(\mathcal{W}_{\mathrm{B}})^{24} \tag{3.11}$$

and

$$\mathcal{Z}_{(4,5)}^{[2]} = \mathrm{Tr}\,(C_2)^5 = \mathrm{Tr}\left(\mathcal{W}_{\mathrm{B}}\mathcal{T}_1^2 C_1^3\right)^5 = \mathrm{Tr}\,(\mathcal{W}_{\mathrm{B}})^{30}, \tag{3.12}$$

where the powers of $\mathcal{W}_{\mathrm{B}}$ on the right hand side of the equations count the number of the p-gonal Boltzmann weights. We recall that the total number of the Boltzmann weights grows exponentially with respect to the iteration step k. The

analytic formula of the exponential dependence of the total number of the spin sites on k is derived in the following Section, where the free energy is examined in detail.

(ii) The Ising model was recently investigated on an infinite sequence of hyperbolic lattices [Krcmar et al., 2008], for which the coordination number was fixed to $q = 4$, whereas the size of the p-gons increased $p = 4,5,6,\ldots,\infty$. The generalized recurrence relations satisfying the lattices ($p \geq 4,4$) are summarized into a more compact form

$$\begin{aligned} C_{j+1} &= \mathcal{W}_{\mathrm{B}} \mathcal{T}_j^{p-2} C_j^{p-3}, \\ \mathcal{T}_{j+1} &= \mathcal{W}_{\mathrm{B}} \mathcal{T}_j^{p-3} C_j^{p-4}. \end{aligned} \tag{3.13}$$

It was conjectured in Ref. [Krcmar et al., 2008] that the Ising model realized on the sequence of the lattices $\{(4,4),(5,4),(6,4),\ldots,(\infty,4)\}$ converges to the Bethe lattice with the coordination number $q = 4$ exponentially with the increasing p. In other words, the Bethe lattice is actually identical with the lattice geometry $(\infty,4)$. By evaluation of all the thermodynamic functions, it was shown that any lattice geometry ($p \geq 15, q = 4$) is numerically indistinguishable from the Bethe lattice with high accuracy [Krcmar et al., 2008]. In particular, having evaluated the phase transition temperature $T_{\mathrm{pt}}^{(\infty,4)}$ of the Ising model on the Bethe lattice, which had been numerically realized on the $(15,4)$ lattice geometry, the numerical accuracy of the CTMRG algorithm resulted in $T_{\mathrm{pt}} = 2.88539$. The Ising model on the Bethe lattice is an exactly solvable system with the phase transition temperature $T_{\mathrm{pt}} = 1/\ln\sqrt{2}$ as derived by Baxter [Baxter, 1982].

(iii) Now we generalize the recurrence relations by considering arbitrary p-gons $p \geq 4$ as well as the coordination number $q \geq 4$, which have never been considered yet. Having analyzed all the geometrical lattice structures (p,q) of the polygonal tailing, it straightforwardly leads to the recurrence relations

$$\begin{aligned} C_{j+1} &= \mathcal{W}_{\mathrm{B}} \mathcal{T}_j^{p-2} C_j^{(p-2)(q-3)-1}, \\ \mathcal{T}_{j+1} &= \mathcal{W}_{\mathrm{B}} \mathcal{T}_j^{p-3} C_j^{(p-3)(q-3)-1}. \end{aligned} \tag{3.14}$$

The calculation of the partition function $\mathcal{Z}$ for any (p,q) lattice geometry in the k^{th} iteration step remains identical to Eq. (3.9). Therefore, the expectation value $\langle O \rangle$ of a local observable O is evaluated directly. The typical example is the spontaneous magnetization $M = \langle \sigma_c \rangle$ measured in the center of the lattice (p,q), where the spin variable σ_c is positioned. If evaluated in the thermodynamic limit, we obtain

$$M_{(p,q)} = \langle \sigma_c \rangle = \frac{\mathrm{Tr}\left[\sigma_c \, e^{-\mathcal{H}_{(p,q)}/T}\right]}{\mathrm{Tr}\left[e^{-\mathcal{H}_{(p,q)}/T}\right]} = \frac{\mathrm{Tr}\left[\sigma_c (C_\infty)^q\right]}{\mathcal{Z}_{(p,q)}^{[\infty]}} \tag{3.15}$$

for arbitrary (p,q).

3.3 Phase Transition Analysis

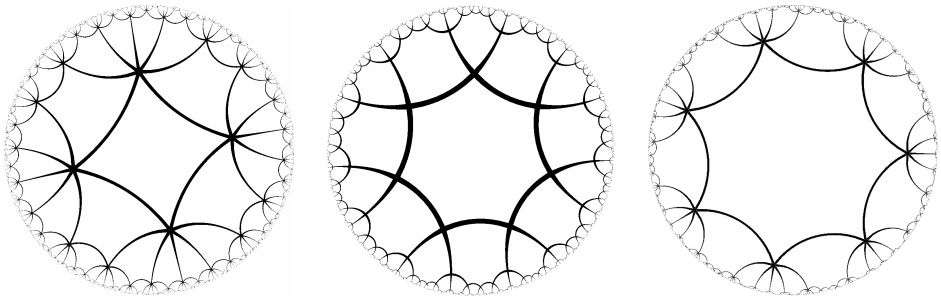

Figure 3.2: The Poincaré disk representation of the three hyperbolic lattices chosen for the analysis of the thermodynamic functions of the spin model.

For instructive reasons, we have selected the three non-trivial hyperbolic lattices $(4,7)$, $(7,4)$, and $(7,7)$, which are shown in Fig. 3.2 in the Poincare representation. We calculated the spontaneous magnetization $M_{(p,q)}$ which is plotted on the upper graph in Fig. 3.3 including the case of the Euclidean $(4,4)$ lattice, which serves as as a benchmark since this case is exactly solvable. It was shown [Krcmar et al., 2008, Gendiar et al., 2012, Gendiar et al., 2014] that the Ising model on certain types of the hyperbolic lattices belongs to the mean-field universality class. Now, we expand our analysis for arbitrary $(p \geq 4, q \geq 4)$ lattices. The spontaneous magnetization follows the scaling relation $M_{(p,q)} \propto (T_{\rm pt}^{(p,q)} - T)^{\beta}$ at the phase transition temperature $T_{\rm pt}^{(p,q)}$ yielding the mean-field magnetic exponent $\beta = \frac{1}{2}$ whenever $(p-2)(q-2) > 4$. Remind that the Ising (not the mean-field) universality class is solely reproduced for the Ising model on the Euclidean lattices; in this case, it is on the square lattice $(4,4)$, where it was confirmed that $M_{(4,4)} \propto (T_{\rm pt}^{(4,4)} - T)^{\frac{1}{8}}$. This is unambiguously manifested by the linear dependence of $M_{(4,4)}^8$ on temperature $T \leq T_{\rm pt}^{(4,4)}$ as depicted on the lower left graph in Fig. 3.3.

On the other hand, the mean-field universality class with $\beta = \frac{1}{2}$ can be read off by plotting $M_{(p,q)}^2$ for $T \leq T_{\rm pt}^{(p,q)}$, which is obvious from the linear decrease of the spontaneous magnetization approaching the phase transition temperature $T_{\rm pt}^{(p,q)}$ as shown on the two lower graphs on the right side in Fig. 3.3.

The mean-field-like feature of the spin model is always realized on the hyperbolic lattices. We point out here that such a mean-field-like behavior is not caused by an insufficient numerical accuracy. The numerical results are fully converged any the additional increase of the number of the states kept in the renormalization

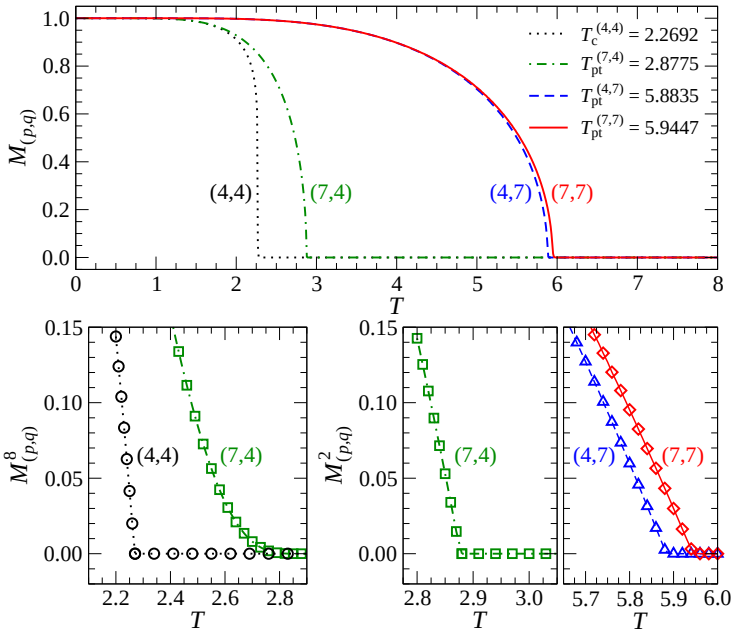

Figure 3.3: The spontaneous magnetization with respect to temperature for the Euclidean square lattice as well as for the three hyperbolic lattices depicted in Fig. 3.2.

group algorithm does not improve any of the thermodynamic functions. Therefore, the reason for the mean-field-like feature rests in the exceedance of the critical lattice dimension $d_c = 4$ because the Hausdorff dimension is infinite for all the hyperbolic lattices in the thermodynamic limit. The claim is identical to that of the exact solution of the Ising model on the Bethe lattice, where the analytically derived mean-field exponents on the Bethe lattice have nothing to do with the mean-field approximation of the model at all [Baxter, 1982]. Instead, the mean-field-like feature is caused by the hyperbolic lattice geometry, which is accompanied by the absence of the divergent correlation length at the phase transition [Gendiar et al., 2012].

3.3.1 Asymptotic Lattice Geometries

Let us investigate the phase transitions of the Ising model on the *asymptotic* lattice geometries as illustrated in Fig. 3.4. In the earlier studies, two distinct scenarios were presented: (1) the coordination number was fixed to $q = 4$ while the p-gons gradually expanded $p = 4, 5, 6, \ldots, \infty$ and (2) we formed the triangular tessellation, $p = 3$, and the coordination number varied $q = 6, 7, 8, \ldots, \infty$. In both the cases a

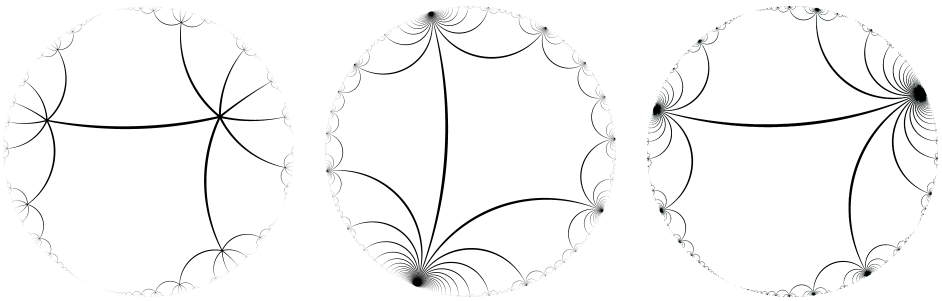

Figure 3.4: The Poincaré representation of the asymptotic hyperbolic lattices $(\infty, 7)$ on the left, $(7, \infty)$ in the middle, and (∞, ∞) on the right.

substantially different asymptotic behavior of the phase transition temperatures was observed [Krcmar et al., 2008, Gendiar et al., 2012]. In the former case, the phase transition temperature converges to the Bethe lattice phase transition $T_{\rm pt}^{(p,4)} \to \frac{2}{\ln 2}$. In the latter case, the triangular tessellation of the lattice types $(3, q \geq 3)$ led to a linear divergence of the phase transition temperature $T_{\rm pt}^{(3,q)} \propto q$. These findings remain valid for arbitrary (p, q) lattices. As examples we selected the hyperbolic lattices $(7, q)$ and $(p, 7)$ with $p, q = 4, 5, 6, \ldots, \infty$ as depicted in Fig. 3.4.

The two upper graphs in Fig. 3.5 show a fast convergence of the magnetization and the phase transition temperatures $T_{\rm pt}^{(p,7)}$ toward the Bethe lattice $(\infty, 7)$ with the coordination number seven. The fast convergence means that the phase transition temperature on the $(7, 7)$ lattice is almost indistinguishable from those on the consequent $(p > 7, 7)$ lattices. We obtained the asymptotic phase transition temperature $T_{\rm pt}^{(p\to\infty,7)} \to 5.944002$, which is in accurate agreement with the general formula for the Bethe lattice phase transition temperature [Baxter, 1982]

$$\lim_{p\to\infty} T_{\rm pt}^{(p,q)} = \frac{1}{\ln \sqrt{[q/(q-2)]}}. \tag{3.16}$$

The middle graph in Fig. 3.5 shows the spontaneous magnetization $M_{(7,q)}$ on the lattices made from septagonal $(p = 7)$ tiling for the gradually increasing coordination number $q = 4, 5, 6, \ldots, \infty$. The phase transition temperature diverges linearly. The result can be generalized, and the linear asymptotic divergence is present

$$T_{\rm pt}^{(p,q\gg 4)} \propto q \tag{3.17}$$

irrespective of p. Finally, if both lattice parameters are set to be equivalent, $p \equiv q$, the scenario with the increasing coordination number and fixed p-gon is dominant

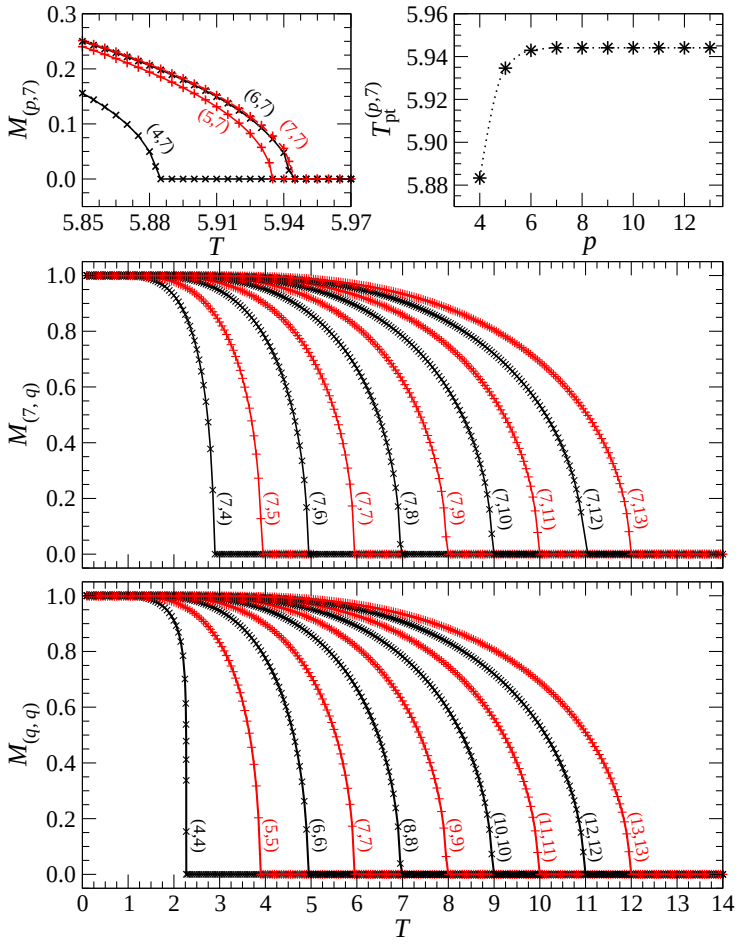

Figure 3.5: The temperature dependence of the spontaneous magnetization toward the asymptotic lattice geometries plotted in Fig. 3.4. The two upper graphs show the fast convergence of the magnetization, and the model on the lattice $(7,7)$ exhibits almost identical behavior as the lattice $(\infty,7)$. The upper and the lower graphs describe the linear increase of the phase transitions if the model is studied on the lattices $(7,q)$ for $q \geq 4$ and (q,q) for $q \geq 5$, respectively.

over that one with the fixed q and increasing p. The bottom graph in Fig. 3.5 depicts the case of the (q,q) lattices for $q = 4,5,6,\ldots,13$, which, excluding the case $q = 4$, also satisfies the linearity $T_{\rm pt}^{(q,q)} \propto q$.

The mean-field universality is induced by the hyperbolic geometry of the curved two-dimensional surface, which can be spanned only in the infinite-dimensional space in the thermodynamic limit. In order to examine the asymptotic lattice geometries shown in Fig. 3.4 in detail, we first consider the Ising model on

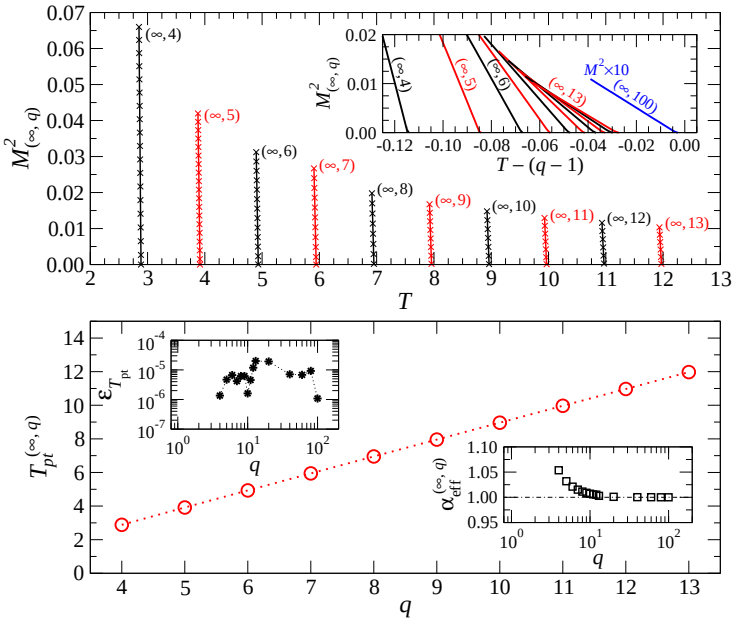

Figure 3.6: The upper graph shows the temperature dependence of a few nonzero values of the squared magnetization approaching the phase transition from the ordered phase $T \leq T_{\rm pt}^{(\infty,q)}$ for the lattices $p = 20$ and $4 \leq q \leq 13$ obtained by CTMRG which accurately reproduce the Bethe lattice. The inset shows the same data in details rescaled to temperatures $T-(q-1)$. In the lower graph, the linearity of $T_{\rm pt}^{(\infty,q)}$ on the Bethe lattice is satisfied with increasing q. The lower right inset shows the convergence of the effective exponent $\alpha_{\rm eff}^{(\infty,q)} \to 1$ in the log-lin scale. The upper left inset displays the numerical accuracy by evaluating the relative error for the phase transition temperature on the Bethe lattices.

the Bethe lattices (∞, q). The shortened linear decrease of the squared order parameters $M^2_{(\infty,q)} \propto \left(T_{\rm pt}^{(\infty,q)} - T\right)$ toward the phase transition points is plotted on the upper graph in Fig. 3.6 for $q = 4,5,6,\ldots,13$ and confirms the mean-field nature.

Now we specify the linear divergence of $T_{\rm pt}^{(\infty,q)} \propto q$ in detail. It can be easily derived in the asymptotic regime for the Ising model on the Bethe lattice if $q \gg 4$ so that

$$T_{\rm pt}^{(\infty,q\gg 4)} \to q - 1\,, \tag{3.18}$$

where we have made use of

$$T_{\rm pt}^{(\infty,q)} = \frac{1}{\ln\sqrt{\frac{q}{q-2}}} \equiv \frac{1}{\operatorname{arctanh}\left(\frac{1}{q-1}\right)} \approx q-1 \tag{3.19}$$

if $q \gg 4$. The inset of the upper graph in Fig. 3.6 shows the asymptotic behavior of

$M^2_{(\infty,q)}$ with respect to the rescaled horizontal axis $T-(q-1)$. The data in the inset fully satisfy the limit in Eq. (3.18). We support the data of the Ising model on the lattice geometry $(\infty,100)$, which tend to reach the asymptotic geometry (∞,∞) as shown in the inset since $\lim_{q\to\infty} T^{(\infty,q)}_{\rm pt}-(q-1)=0$.

The numerical data at the phase transition are also verified by the specification of the linear dependence of the transition temperatures $T^{(\infty,q)}_{\rm pt}$ on q. In general, let us assume a q-dependent effective exponent $\alpha^{(\infty,q)}_{\rm eff}$

$$1+T^{(\infty,q)}_{\rm pt}\propto q^{\alpha^{(\infty,q)}_{\rm eff}}, \tag{3.20}$$

The fast convergence of $\alpha^{(\infty,q)}_{\rm eff}\to 1$ with the increasing q is depicted in the inset on the lower right graph in Fig. 3.6, for the additional data with the coordination numbers $q=20,40,60,80$, and 100. The phase transition temperatures of the Ising model on the Bethe lattices reach the sufficiently high numerical accuracy with respect to Eq. (3.16). The relative error is as small as $\varepsilon_{T_{\rm pt}}\approx 10^{-5}$ if calculated at the phase transition temperature $T^{(\infty,q)}_{\rm pt}$ as shown in the upper left inset of Fig. 3.6. (The inset demonstrates the lowest numerical accuracy, which is known to occur at phase transitions.)

Up to this point we have verified the correctness of the recurrence relations by evaluating the phase transition points. We have compared our results with the exact solutions on the Bethe lattices and evaluated the largest numerical errors at the phase transitions. In the following, we proceed with the derivation of the free energy with respect to (p,q).

3.4 Free energy calculation

Let the free energy for any lattice geometry (p,q), cf. Eq. (3.9), be normalized per lattice spin site to avoid any divergences associated with the thermodynamic limit. The free energy per site, expressed as a function of the iteration step k, has the form

$$\mathcal{F}^{[k]}_{(p,q)}=-\frac{T}{\mathcal{N}^{[k]}_{(p,q)}}\ln\mathcal{Z}^{[k]}_{(p,q)}\equiv-\frac{T\ln{\rm Tr}\,(C_k)^q}{\mathcal{N}^{[k]}_{(p,q)}}, \tag{3.21}$$

The normalization of the free energy per spin site is given by a non-trivial integer function $\mathcal{N}^{[k]}_{(p,q)}$, which counts the total number of the spin sites with respect to given k and (p,q). The free energy per site plays a crucial role in the current analysis since one can derive all the thermodynamic functions from it in order to determine the phase transition accurately. On the contrary to the magnetization, the free energy involves the boundary effects.

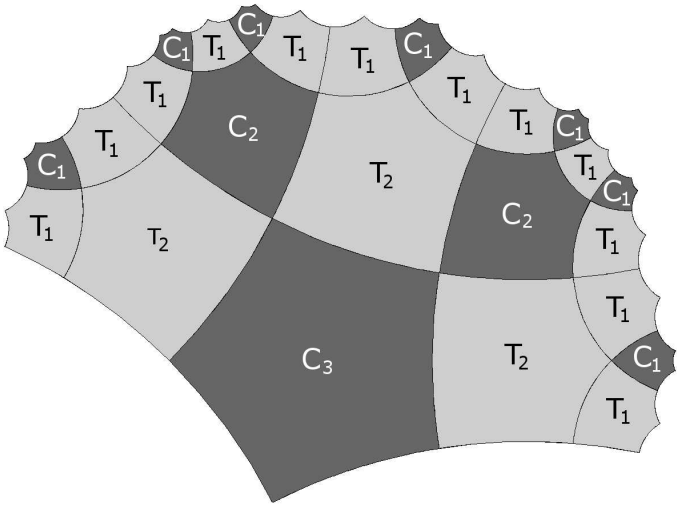

Figure 3.7: The graphical representation of the corner transfer tensor C_3 for the hyperbolic lattice $(5,4)$ on the in accord with (3.7) for $k = 3$. We use the dark and the bright shaded p-gons in order to distinguish clearly between C_k and $\mathcal{T}_k$, respectively.

A direct numerical calculation of the free energy per site in Eq. (3.21) frequently results in an extremely fast divergence of the partition function $\mathcal{F}^{[k]}_{(p,q)}$ as well as the total number of sites $\mathcal{N}^{[k]}_{(p,q)}$ on hyperbolic lattices whenever $k \gtrsim 10$. Therefore, the numerical operations with the tensors C_k and $\mathcal{T}_k$ require to consider an appropriate norm (normalization) in each iteration step k. We use the normalization introduced in Eq. (2.35), where the norm is defined as the absolute value of the largest matrix (tensor) element.

For clarity, the free energy analysis is split into three parts. First, the free energy per site on the Euclidean square lattice $(4,4)$ was derived in Section 2.2. Here, the hyperbolic lattice $(5,4)$ is considered, and a recurrence formalism of the free energy is given for $k = 3$, which is associated with a graphical description of the lattice for the direct visual comparison. Finally, we generalize the free energy calculation for any (p,q) lattice geometry.

3.4.1 Free energy on (5,4) lattice

We now consider the other example. It is instructive to express graphically the complete structure of the normalized corner tensor $\widetilde{C}_3$ on the hyperbolic lattice $(5,4)$ as depicted in Fig. 3.7 on the right. The structure agrees with the recurrence relations in Eqs. (3.7). The analogous decomposition of $\widetilde{C}_3$ into the normalization

factors c_j and t_j (for $j = 1,2,\ldots,k$) gives

$$\begin{aligned}\widetilde{C}_3 = \frac{C_3}{c_3} &= \frac{\mathcal{W}_{\mathrm{B}}\widetilde{\mathcal{T}}_2^3\widetilde{C}_2^2}{c_3} = \frac{\mathcal{W}_{\mathrm{B}}\mathcal{T}_2^3 C_2^2}{t_2^3 c_3 c_2^2} \\ &= \frac{\mathcal{W}_{\mathrm{B}}\big(\mathcal{W}_{\mathrm{B}}\widetilde{\mathcal{T}}_1^2\widetilde{C}_1\big)^3\big(\mathcal{W}_{\mathrm{B}}\widetilde{\mathcal{T}}_1^3\widetilde{C}_1^2\big)^2}{t_2^3 c_2^2 c_3} \\ &= \frac{\mathcal{W}_{\mathrm{B}}^6\mathcal{T}_1^{12}C_1^7}{t_1^{12}t_2^3 c_1^7 c_2^2 c_3} = \frac{\mathcal{W}_{\mathrm{B}}^{25}}{t_1^{12}t_2^3 t_3^0 c_1^7 c_2^2 c_3^1}\,.\end{aligned} \tag{3.22}$$

Evidently, the power in the Boltzmann weight completely reproduce the pentagonal lattice structure (5,4) shown in Fig. 3.7. The powers associated with the normalization factors also coincide with the number of the individual tensors depicted graphically.

We denote the powers in the factors c_j and t_j for $j = 1,2,\ldots,k$, respectively, by the integer exponents n_{k-j+1} and m_{k-j+1}, which are indexed in the reverse order for the later convenience of writing the expressions in a simpler form. In particular, the integer exponents in the denominator of Eq. (3.22) satisfy the ordering $t_1^{m_3}t_2^{m_2}t_3^{m_1}c_1^{n_3}c_2^{n_2}c_3^{n_1}$. They are also used in the computation of the total number of the spin sites $\mathcal{N}_{(5,4)}^{[k]}$ via the relation

$$\mathcal{N}_{(5,4)}^{[k]} = 1 + 4\sum_{j=1}^{k} 3n_j + 2m_j\,. \tag{3.23}$$

At the same time, the integer exponents n_j and m_j have to satisfy the recurrence relations

$$\begin{aligned} n_{j+1} &= 2n_j + m_j\,, \qquad & n_1 &= 1\,, \\ m_{j+1} &= 3n_j + 2m_j\,, \qquad & m_1 &= 0\,. \end{aligned} \tag{3.24}$$

Since the entire lattice (5,4) is made by tiling the four corner tensors C_k meeting at the central spin site (cf. Fig. 3.1), the number 1 and the prefactor 4 (in front of the summation) in Eq. (3.23), respectively, correspond to the central spin and the four joining tensors ($q = 4$). The remaining two prefactors 3 and 2 under the summation in Eq. (3.23) count those spin sites, which are not shared by the two attached pentagonal tensors C_j and $\mathcal{T}_j$ ($j = 1,2,\ldots,k$), respectively. (A deep analysis of the (5,4) lattice is inevitable to understand all the details.)

The free energy per site at given k on the hyperbolic lattice (5,4) can be expressed in the following generalized form

$$\mathcal{F}_{(5,4)}^{[k]} = -\frac{4T\ln\mathrm{Tr}\,\widetilde{C}_k}{\mathcal{N}_{(5,4)}^{[k]}} - \frac{4T\sum_{j=0}^{k-1}\ln c_{k-j}^{n_{j+1}} + \ln t_{k-j}^{m_{j+1}}}{\mathcal{N}_{(5,4)}^{[k]}}\,. \tag{3.25}$$

The first term converges to zero with increasing k, i.e.,

$$\lim_{k\to\infty} \frac{4T \ln \mathrm{Tr}\, \widetilde{C}_k}{\mathcal{N}^{[k]}_{(5,4)}} = 0\,, \tag{3.26}$$

since the normalized partition function $\widetilde{\mathcal{Z}}^{[\infty]}_{(p,q)} \equiv \mathrm{Tr}\, \widetilde{C}_\infty$ is bounded at any temperature in the thermodynamic limit

$$1 \le \widetilde{\mathcal{Z}}^{[\infty]}_{(p,q)} \le M \tag{3.27}$$

for an arbitrary M-state spin system. The lower and the upper bounds correspond to the limits $\lim_{T\to 0} \widetilde{\mathcal{Z}}^{[\infty]}_{(p,q)} = 1$ and $\lim_{T\to\infty} \widetilde{\mathcal{Z}}^{[\infty]}_{(p,q)} = M$, respectively. Finally, the number of spin sites in the denominator of the first term grows exponentially $\mathcal{N}^{[k]}_{(5,4)} \propto 3.7^k$ as plotted in Fig. 3.8.

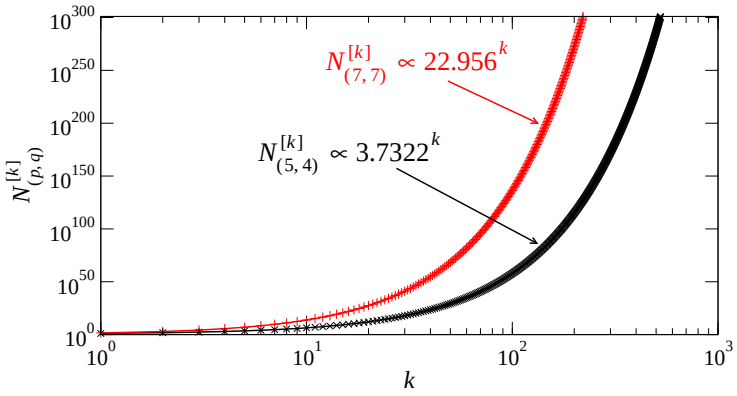

Figure 3.8: The exponential dependence of the total number of the spins on the iteration number k (the least-square fitting in the log-log plot) for the two lattices $(5,4)$ and $(7,7)$.

3.4.2 Free energy on (p,q) lattices

The generalization of the free energy calculation for any (multi-state) spin model on an arbitrary lattice geometry ($p \ge 4, q \ge 4$) is straightforward and requires a careful graphical analysis of many lattice geometries, which is beyond the scope of this work for its extensiveness. The free energy per spin for a finite k has the

generalized form

$$\begin{aligned}\mathcal{F}^{[k]}_{(p,q)} &= -\frac{qT\ln \mathrm{Tr}\,\widetilde{C}_k}{\mathcal{N}^{[k]}_{(p,q)}} - \frac{qT\sum_{j=0}^{k-1}\ln c_{k-j}^{n_{j+1}} + \ln t_{k-j}^{m_{j+1}}}{\mathcal{N}^{[k]}_{(p,q)}} \\ &\overset{k\gg 1}{=} -\frac{qT\sum_{j=0}^{k-1} n_{j+1}\ln c_{k-j} + m_{j+1}\ln t_{k-j}}{\mathcal{N}^{[k]}_{(p,q)}},\end{aligned} \tag{3.28}$$

where the total number of the spin sites is expressed as

$$\mathcal{N}^{[k]}_{(p,q)} = 1 + q\sum_{j=1}^{k}(p-2)n_j + (p-3)m_j, \tag{3.29}$$

and the integer variables n_j and m_j satisfy more complex recurrence relations

$$\begin{aligned} n_{j+1} &= [(p-2)(q-3)-1]n_j + [(p-3)(q-3)-1]m_j, \\ m_{j+1} &= (p-2)n_j + (p-3)m_j, \\ n_1 &= 1, \\ m_1 &= 0. \end{aligned} \tag{3.30}$$

The evaluation of Eq. (3.29) is carried out numerically, and a strong exponential behavior occurs with increasing p and q. Figure 3.8 shows the log-log plot of the exponential increase of the total number of the sites $\mathcal{N}^{[k]}_{(7,7)} > \mathcal{N}^{[k]}_{(5,4)}$.

The final expression for the free energy in Eqs. (3.28)-(3.30) also includes the case of the Euclidean lattice $(4,4)$. The complete equivalence with Eq. (2.42) can be easily verified if considering that $n_j = n_{j-1} = \cdots = n_1 \equiv 1$ and $m_j = 2n_{j-1} + m_{j-1} = 2(j-1) + m_1 \equiv 2j-2$, which reduce the exponential dependence of the total number of the spin sites back to the power-law behavior in Eq. (2.36)

$$\mathcal{N}^{[k]}_{(4,4)} = 1 + 4\sum_{j=1}^{k} 2n_j + m_j \equiv (2k+1)^2. \tag{3.31}$$

3.5 Results

Having defined the free energy per site for the lattice geometries (p,q), we analyze the phase transition of spin models in the thermodynamic limit on the four representative lattices $(4,4)$, $(4,7)$, $(7,4)$, and $(7,7)$ we have used earlier. We have shown that the phase transition temperatures T_{pt}, calculated by the spontaneous

magnetization $M_{(p,q)}$ at the lattice center, correctly reflected the bulk properties, and the boundary effects were eliminated. In other words, if various types of the boundary conditions (such as free and fixed ones) are imposed, the phase transition of the Ising model is not affected provided that we evaluated the expectation value $\langle \sigma_c \rangle$ in Eq. (3.15). The correctness and high numerical accuracy has been compared with the exactly solvable Ising model on Bethe lattice [Baxter, 1982].

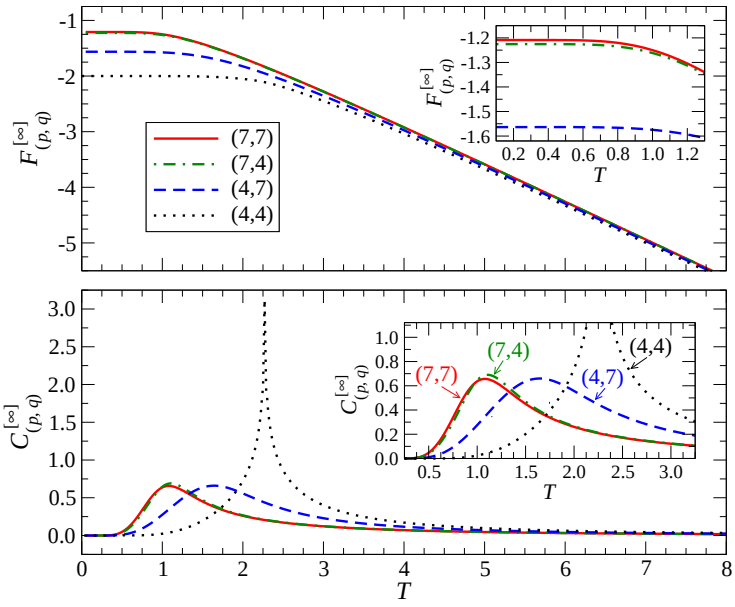

Figure 3.9: The free energy from Eq. (3.28) and the specific heat from Eq. (3.32) vs temperature on the selected lattices (4,4), (4,7), (7,4), and (7,7). The inset shows the details of the broadened specific heat maxima.

3.5.1 Absence of phase transition on non-Euclidean lattices

The upper graph of Fig. 3.9 shows the free energies on the four representative lattices, which is evaluated by Eq. (3.28). A phase transition can be associated with a singular (non-analytic) behavior of the specific heat being the second derivative of the free energy with respect to temperature

$$C^{[\infty]}_{(p,q)} = -T \frac{\partial^2}{\partial T^2} \mathcal{F}^{[\infty]}_{(p,q)} . \tag{3.32}$$

The temperature dependence of the specific heat of the Ising model on the respective four lattices is plotted on the lower graph in Fig. 3.9. Evidently, we find the non-analytic behavior on the square lattice (4,4) with the diverging peak at the

temperature, which corresponds to the exact critical temperature $T_c = 2/\ln(1+\sqrt{2})$.

However, none of the three hyperbolic lattice geometries results in an analogous non-analytic peak at the phase transition temperatures $T_{\text{pt}}^{(p,q)}$ we had calculated from the spontaneous magnetization plotted in Fig. 3.3. Instead, a broad maximum appears for the particular lattices, which does not correspond to the correct phase transition temperatures we had detected earlier.

Strong boundary effects on the hyperbolic lattices prevent the Monte Carlo (MC) simulations from the accurate analysis of phase transition phenomena on the hyperbolic lattices [Shima and Sakaniwa, 2006a, Shima and Sakaniwa, 2006b, Baek et al., 2007, Sakaniwa and Shim, 2009]. The necessity to subtract a couple of boundary site layers were performed to detect the correct bulk properties [Hasegawa et al., 2007]. If defining a ratio of the boundary sites to the total number of sites, the ratio converges to zero in the Euclidean case, whereas it goes to nonzero values on the hyperbolic lattices in the thermodynamic limit.

3.5.2 The Bulk Free Energy

In order to specify the phase transition temperature on the hyperbolic lattices correctly, the free energy has to be modified by reducing the boundary layers from the total free energy. With each next iteration step $k+1$, the CTMRG algorithm expands the lattice size by increasing and pushing the boundary sites farther from the lattice center. This expansion process can be regarded as an additional spin layer (the shell), which is composed of the tensors C_1 and $\mathcal{T}_1$ multiplying its number in accord with the recurrence relations, and the q tensors C_{k+1} are included in the center of the lattice at the same time, cf. Fig. 3.7. Hence the lattice can be thought of as a concentric system of the shells indexed by j so that the j^{th} shell contains the spin sites, which separate the spin sites in the tensors C_j and $\mathcal{T}_j$ from the spin sites in the tensors C_{j-1} and $\mathcal{T}_{j-1}$ on a given (p,q) geometry (cf. Fig. 3.7). Such a structure of the concentric shells in the k^{th} iteration step ascribes the outermost shell to $j = 1$ toward the innermost (non-trivial) shell $j = k$ (leaving the central spin site apart), which is related to the way of counting the total number of the spin sites in Eq. (3.29).

If the integer ℓ denotes the ℓ outermost shells $j = 1, 2, \ldots, \ell < k$, we can introduce a new quantity, the *bulk* free energy $\mathcal{B}_{(p,q)}^{[k,\ell]}$, which defines the free energy of the $k-\ell$ inner shells. It is given by the subtraction of the free energy contributing from the ℓ outer shells from the total free energy. In particular, the bulk free energy in the k^{th} iteration step is

$$\mathcal{B}_{(p,q)}^{[k,\ell]} = \mathcal{F}_{(p,q)}^{[k]} - \mathcal{F}_{(p,q)}^{*[k,\ell]}, \tag{3.33}$$

where the asterisk in the second term denotes the free energy of the ℓ outermost shells so that

$$\mathcal{F}^{*[k,\ell]}_{(p,q)} = -\frac{qT\sum_{j=k-\ell}^{k-1} n_{j+1}\ln c_{k-j} + m_{j+1}\ln t_{k-j}}{\mathcal{N}^{*[k,\ell]}_{(p,q)}} \tag{3.34}$$

and

$$\mathcal{N}^{*[k,\ell]}_{(p,q)} = q\sum_{j=k-\ell+1}^{k}(p-2)n_j + (p-3)m_j\,. \tag{3.35}$$

For the tutorial purpose, we set $\ell = \frac{k}{2}$ and study the thermodynamic limit $k \to \infty$. (The non-trivial dependence of the bulk free energy on ℓ is to be thoroughly studied elsewhere [Lee and Gendiar,].) Following the remarks below Eq. (3.28) and without loss of generality, we omit the first term in Eq. (3.34) as the term converges to zero after a few iterations.

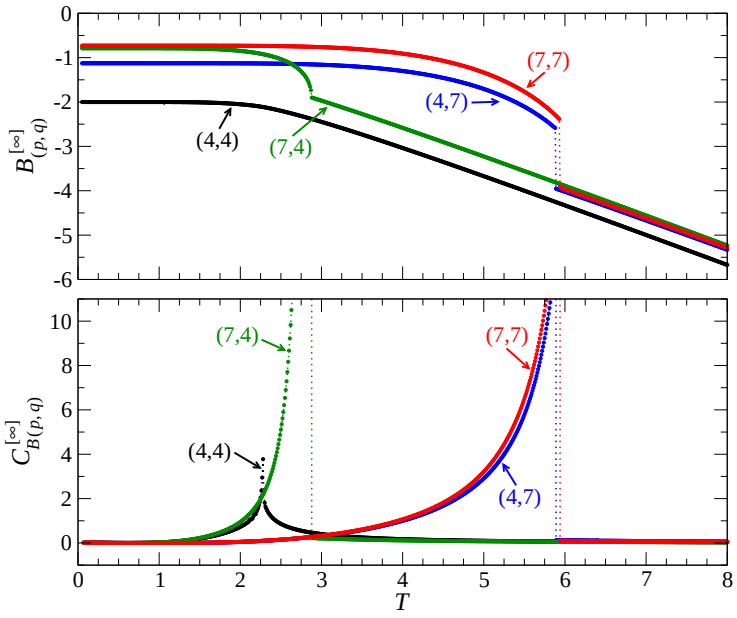

Figure 3.10: The bulk free energy (the upper graph) and the bulk specific heat (the lower graph) vs. temperature for the Ising model on the lattices $(4,4)$, $(4,7)$, $(7,4)$, and $(7,7)$. The vertical dotted lines accurately correspond to the phase transition temperatures we have obtained from the spontaneous magnetization in Fig. 3.3.

Figure 3.10 (the upper graph) shows the bulk free energy for the Ising model on the four representative lattices in the thermodynamic limit, i.e.

$$\mathcal{B}^{[\infty]}_{(p,q)} \equiv \lim_{k\to\infty} \mathcal{B}^{[k,k/2]}_{(p,q)}\,. \tag{3.36}$$

In the case of the Euclidean lattice, we get $\mathcal{B}^{[\infty]}_{(4,4)} \equiv \mathcal{F}^{[\infty]}_{(4,4)}$ since the thermodynamic properties in the bulk are not affected by the boundary conditions. However, the bulk free energy calculated on the hyperbolic lattices exhibits a remarkable singularity occurring exactly at the phase transition temperature. The typical structure of the free energy does not change irrespective of the type of the boundary conditions applied (free and fixed ones). The maxima of the bulk specific heat

$$C^{[\infty]}_{B\,(p,q)} = -T\frac{\partial^2}{\partial T^2}\mathcal{B}^{[\infty]}_{(p,q)}\,. \tag{3.37}$$

plotted in the lower graph of Fig. 3.10 accurately correspond to the phase transition temperatures $T^{(p,q)}_{\rm pt}$ we have studied in Sec. II. The discontinuous jump of the bulk specific heat is associated with the typical mean-field universality behavior [Gendiar et al., 2012, Gendiar et al., 2014], and the vertical dotted lines serve as guides for the eye to help locate the phase transition temperature. It is worth to point out the identical determination of the phase transition temperatures, as we have obtained independently by the spontaneous magnetization in Fig. 3.3.

Our definition of the bulk free energy contains lots of interesting features. For instance, the ℓ-dependence enables us to observe and explain the way how the lattice boundary affects the central bulk part of the lattice and the phase transition if an additional magnetic field is imposed on the boundary spins only. Such a study is to be published elsewhere [Lee and Gendiar,]. We do not follow the Baxter's proposal of calculating the free energy, which is defined by numerical integrating the spontaneous magnetization with respect to a magnetic field [Baxter, 1982]. Although such an approach can be numerically feasible and can be also used to reproduce all the well-known results for the Bethe lattices, it cannot reflect many aspects of the boundary effects which play the significant role on the hyperbolic (p,q) geometries.

3.5.3 Free energy versus lattice geometry

Having been motivated by the correspondence between the anti-de Sitter spaces and the conformal field theory of the quantum gravity physics, one can put the question: *"Given an arbitrary spin system on an infinite set of (p,q) geometries, which lattice geometry minimizes the free (ground-state) energy?"*. This is certainly a highly non-trivial task to be explained thoroughly. Nevertheless, we attempt to answer the question in the following for a particular set of curved lattice surfaces we have been considering. This helps us give an insight into the role of the space geometry with respect to the microscopic description of the spin interacting system. Although we currently consider the free energy of the *classical* spin lattice systems, we have been recently studying the ground-state energy of the

quantum spin systems on the lattices $(p \geq 4, 4)$, which also exhibit qualitatively identical features as studied in this work [Daniška and Gendiar, 2015, Daniška and Gendiar, 2016]. For this reason, the free energy for classical spin systems and the ground-state energy of quantum spin systems are mutually related.

The free energy per site $\mathcal{F}^{[\infty]}_{(p,q)}$ converges to a negative value $\mathcal{F}^{[\infty]}_{(p,q)} < 0$ at finite temperatures $T < \infty$ in the thermodynamic limit. Scanning the entire set of the $(p \geq 4, q \geq 4)$ geometries, we show in the following that the free energy per site reaches its minimum on the square lattice only

$$\mathcal{F}^{[\infty]}_{(4,4)} = \min_{(p\geq 4, q\geq 4)} \left\{ \mathcal{F}^{[\infty]}_{(p,q)} \right\} \tag{3.38}$$

at any fixed temperature T. Therefore, we plot the *shifted* free energy per site, $\mathcal{F}^{[\infty]}_{(p,q)} - \mathcal{F}^{[\infty]}_{(4,4)} \geq 0$, for clarity of the figures.

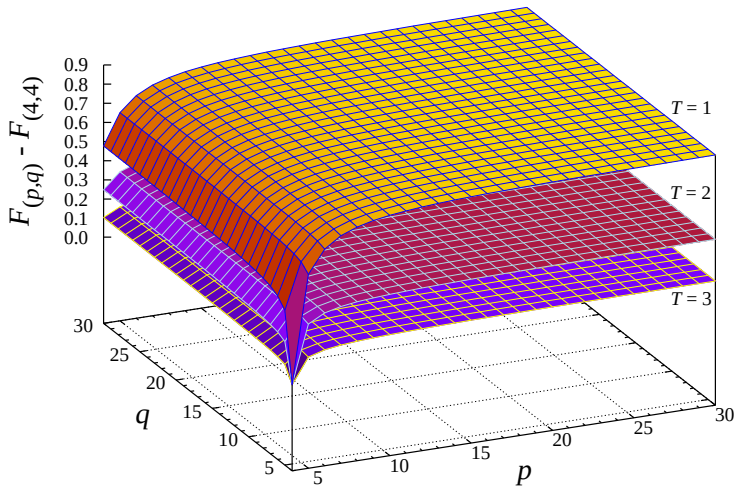

Figure 3.11: The free energy per site as a function of the lattice geometry (p, q) at the selected lower temperatures $T = 1, 2$, and 3.

Figures 3.11 and 3.12 show the shifted free energy for the Ising $(M = 2)$ model at lower and higher temperatures, respectively. These numerical calculations unambiguously identify the square lattice geometry, which minimizes the free energy per spin site. The free energy per site at fixed T becomes less sensitive for higher values of p and q. We observe a weak increasing tendency in the free energy if p increases at fixed q; it grows logarithmically as discussed later. The free energy gets saturated to a constant in the opposite case when q increases at fixed p. It is worth to mention that the presence of the phase transition does not affect the free energy minimum observed on the Euclidean square lattice. Moreover, as

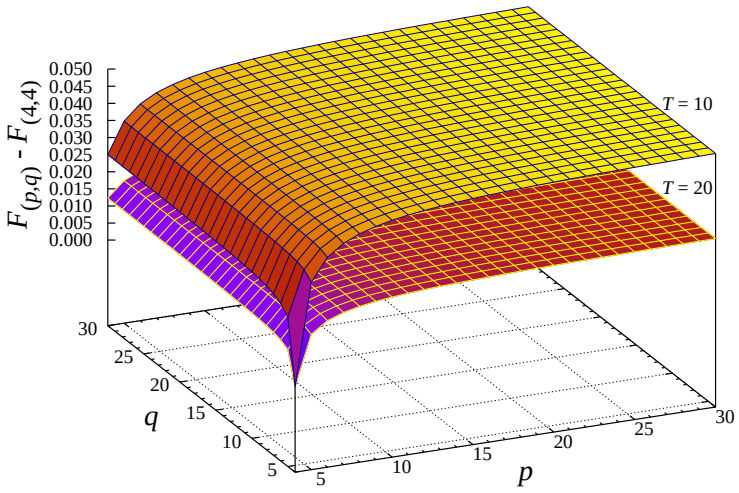

Figure 3.12: The same as in Fig. 3.11 for $T = 10$ and 20.

the temperature grows, the difference between the free energies on the square and the hyperbolic lattices weakens.

It is instructive to generalize the free energy features of the Ising model to the other spin models, the M-state clock and M-state Potts models. The high-temperature asymptotics of the free energy for the multi-state spin models on the referenced hyperbolic lattice $(7,7)$ is depicted on the upper graph of Fig. 3.13. The free energy exhibits an asymptotic behavior at higher temperatures for a fixed lattice geometry (p,q). It is a consequence of the thermodynamic limit measured deeply in the disordered phase, where $T \gtrsim T_{\rm pt}^{(p,q)} \approx q$. Then, the tensors C_∞ and $\mathcal{T}_\infty$ prefer higher symmetries (on the contrary, fewer symmetries occur in the ordered phase if the spontaneous symmetry-braking is present). The higher symmetries cause that the normalization factors $c_{k\to\infty} \to M^{p-2}$ and $t_{k\to\infty} \to M^{p-3}$ above $T \gtrsim 2q$, reminding that the exponents $p-2$ and $p-3$ are associated with the number of the summed up M-state spins in the tensors (cf. also Eq. (3.29)). Substituting $c_k = M^{p-2}$ and $t_k = M^{p-3}$ into Eq. (3.28), one obtains the high-temperature expression

$$\lim_{\substack{k\to\infty \\ T\gtrsim 2q}} \mathcal{F}_{(p,q)}^{[k]} \propto -T \ln M\,. \tag{3.39}$$

The asymptotic linearity of the free energy is examined by the entropy

$$\mathcal{S}_{(p,q)}^{[\infty]} = -\frac{\partial \mathcal{F}_{(p,q)}^{[\infty]}}{\partial T}\,, \tag{3.40}$$

which gets saturated so that $\mathcal{S}_{(p,q)}^{[\infty]} \to \ln(M)$ at $T \gtrsim 2q$. The lower graph in Figure 3.13 satisfies this condition and can be considered as an independent confir-

mation of the correct calculation of the free energy per site in Eq. (3.28). The high-temperature asymptotic behavior of the entropy is explicitly plotted to show that $\exp\left\{\mathcal{S}^{[\infty]}_{(p,q)}\right\} = M$ for the given set of the M-state spin models.

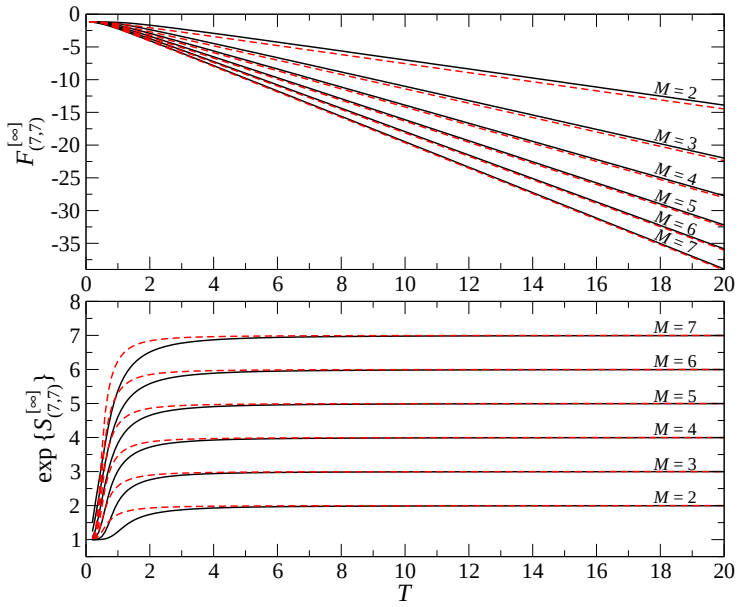

Figure 3.13: The high-temperature asymptotics of free energy per site (the top graph) and the entropy (the lower graph) applied to the lattice $(7,7)$. The full and the dashed lines correspond to the M-state clock and the M-state Potts models, respectively, where $M = 2,3,\ldots,7$.

Figure 3.14 shows the free energy per site with respect to (p,q) for the 7-state clock and the 7-state Potts models at $T = 5$. Clearly, the free energy reaches its minimum on the square lattice for the both spin models. Having scanned the multi-state spin variables $M = 2,3,\ldots,7$ (not shown) for various temperatures T, the free energy remains minimal on the square lattice $(4,4)$.

3.5.4 Relation between energy and curvature

The studied (p,q) lattices can be exactly characterized by the radius of Gaussian curvature [Mosseri and Sadoc, 1982], which has the analytical expression

$$\mathcal{R}_{(p,q)} = -\frac{1}{2\,\mathrm{arccosh}\left[\dfrac{\cos\left(\frac{\pi}{p}\right)}{\sin\left(\frac{\pi}{q}\right)}\right]}. \tag{3.41}$$

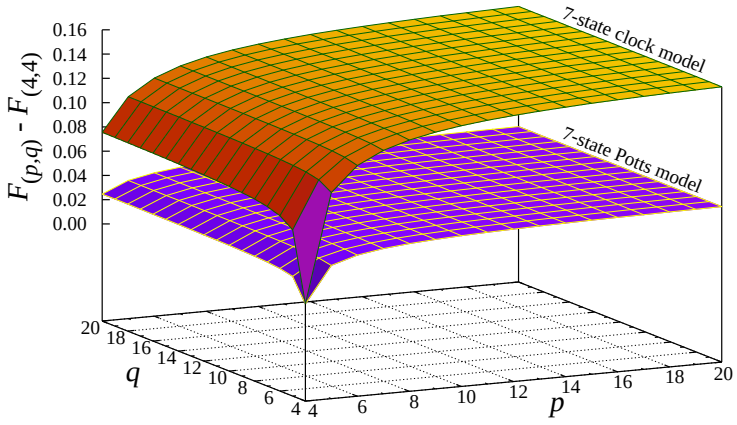

Figure 3.14: The free energy for the 7-state clock and Potts models at $T = 5$, which do not differ from the Ising model ($M = 2$) in Figs. 3.11 and 3.12 qualitatively.

For later convenience we include the negative sign in $\mathcal{R}_{(p,q)}$. The radius of curvature for the square lattice geometry $(4,4)$ diverges, $R_{(4,4)} \to -\infty$, while the remaining hyperbolic lattice geometries (p,q) are finite and non-positive. The analytical description in Eq. (3.41) results in a constant and position independent curvature at any position on the infinitely large lattices (p,q). It is a consequence of the constant distance between the lattice vertices for all geometries (p,q), which is equivalent to keeping the spin-spin coupling to be $J = 1$ in all the numerical analysis of the spin systems on the (p,q) lattices.

In Fig. 3.15 we plot the radius of curvature in the dual geometry (q,p), i.e., the roles of p and q are swapped. It is immediately evident that the surface shape of $\mathcal{R}_{(q,p)}$ exhibits a qualitative similarity if compared to the free energy per site $\mathcal{F}^{[\infty]}_{(p,q)}$ we depicted in Figs. 3.11, 3.12, and 3.14.

Such a surprising observation opens new questions about the relation between the energy at thermal equilibrium and the space (lattice) geometry, which is equivalent to the relation between the ground-state energy of quantum systems and the underlying geometry. We, therefore, focus on the low-temperature regime, $T < 1$, where the similarity is most striking, provided that the numerical computations remain reliable in order to avoid any under/overflows in the transfer tensors. For this reason, the numerical calculations require the setting of the 34 decimal digit precision.

In Fig. 3.16 we plot both the free energy per site $\mathcal{F}^{[\infty]}_{(p,q)}$ at $T = 0.5$ and the radius of curvature $\mathcal{R}_{(q,p)}$ on the dual lattice with respect to p (the upper graph) and q (the lower one) while the other associated lattice parameter is fixed. The upper graph compares the free energy per site with the radius of curvature at fixed $q^* = 4$ and $q^* = 7$ when $4 \leq p \leq 30$. On the other hand, the lower graph displays $\mathcal{F}_{(p^*,q)}$ and

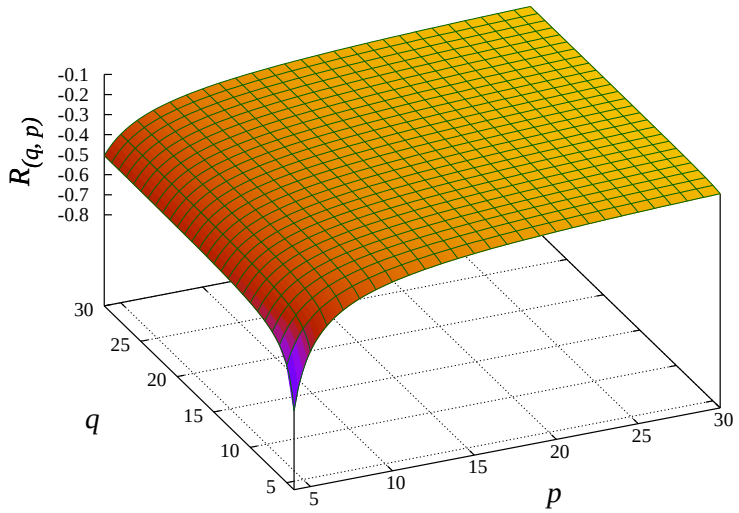

Figure 3.15: The functional dependence of the Gaussian radius of curvature $\mathcal{R}_{(q,p)}$ plotted in the dual lattice geometry (q, p).

$\mathcal{R}_{(q,p^*)}$ at fixed $p^* = 4$ and $p^* = 7$ for $4 \leq q \leq 30$. While in the former case both the functions increase with p, in the latter case the functions saturate and converge to constants.

It is instructive to inspect the asymptotic behavior of $\mathcal{R}_{(q,p)}$. If q is fixed to an arbitrary $q^* \geq 4$, the logarithmic dependence on p is present and $\mathcal{R}_{(q^*,p\gg 4)} \to -1/2 \ln[\frac{2p}{\pi}\cos(\frac{\pi}{q^*})]$. Fixing p to p^* causes that the radius of curvature converges to a constant so that for a sufficiently large p^*, the constant does not depend on q and $\mathcal{R}_{(q\gg 4,p^*)} \to -1/2 \ln[\frac{2}{\sin(\pi/p^*)} - \frac{\sin(\pi/p^*)}{2}] \approx -1/\ln(\frac{2p^*}{\pi})^2$. It is straightforward to conclude that the asymptotics of $\mathcal{R}_{(q,p)}$ is solely governed by the parameter p, i.e. $\mathcal{R}_{(q\gg 4,p\gg 4)} \to -1/2 \ln(\frac{2p}{\pi})$.

Since the seemingly similar p-dependence of the free energy plotted on the upper graph in Fig. 3.16 does not suffice to conjecture the identical logarithmic asymptotics as we have derived for $\mathcal{R}_{(q^*,p\gg 4)}$, we extended our numerical calculations of the free energy per site at larger p for the two selected coordination numbers $q^* = 4$ and $q^* = 7$. Figure 3.17 shows the asymptotic behavior of $\mathcal{F}^{[\infty]}_{(p,q^*)}$ and $\mathcal{R}_{(q^*,p)}$ for $4 \leq p \leq 1024$ at $T = 0.1$. The upper and the lower graphs show both the free energy per site and the radius of curvature in the linear scale and the log-log plot, respectively.

The least-square fitting applied to the free energy per site gives the function $\frac{1}{2-p} + \mathcal{F}^{[\infty]}_{(\infty,q^*)}$, which correctly reproduces the asymptotics of the free energy per site for both q^*. In contrast to the radius of curvature, which logarithmically converges to zero as $p \to \infty$, the free energy per site converges $\mathcal{F}^{[\infty]}_{(\infty,q^*)} = -1$ for

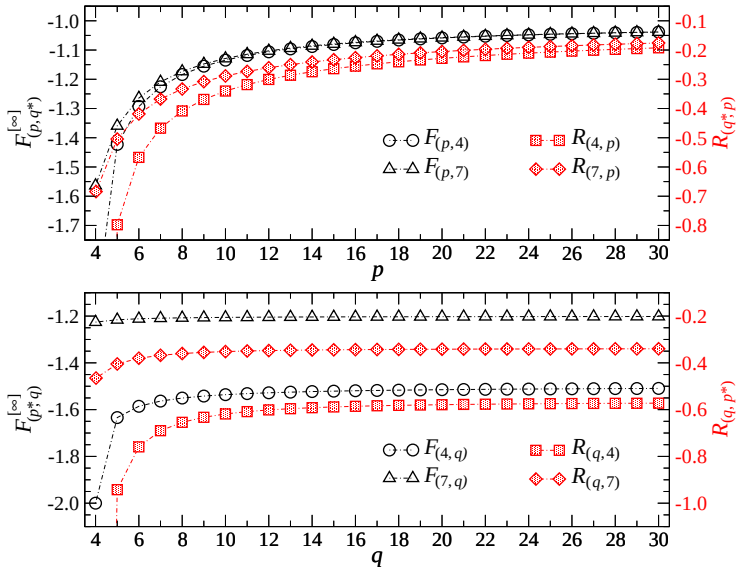

Figure 3.16: The comparison of the free energy per site for the Ising model at $T = 0.5$ with the Gaussian radius of curvature on the dual geometry. The upper graph shows the case of the two fixed coordination numbers $q^* = 4$ and $q^* = 7$, whereas the lower graph depicts the opposite case when fixing the p-gons to the sizes $p^* = 4$ and $p^* = 7$.

$T \ll 1$ and is linear in temperature $\mathcal{F}^{[\infty]}_{(\infty,q^*\lesssim T/2)} = -T\ln(M)$ for $T \gg 1$ in accord with Eq. (3.39). At $T = 0.1$ the term $\mathcal{F}^{[\infty]}_{(\infty,q^*)} = -1.00098$ for $q^* = 4$ and $q^* = 7$. The inset of the upper graph in Fig. 3.17 shows the functional dependence of the constant $\mathcal{F}^{[\infty]}_{(\infty,q^*)}$ on temperature, which is numerically feasible up to the polygonal size $p = 1024$ with the sufficient accuracy (noticing a negligible dependence on small values of q^*). The log-log plot of the lower graph clearly demonstrates the difference in the asymptotics ($p \gg 4$) between the polynomial behavior of $\mathcal{F}^{[\infty]}_{(p,q^*)} - \mathcal{F}^{[\infty]}_{(\infty,q^*)} = -\frac{1}{p}$ and the logarithmic one $\mathcal{R}^{-1}_{(q^*,p)} = -\ln(2p/\pi)^2$. The thin dotted line on the lower graph is the numerical derivative of $-\frac{1}{2}\mathcal{R}^{-1}_{(q^*,p)}$ with respect to p, which confirms the convergence to the asymptotic regime p^{-1} of the free energy per site. We, therefore, conjecture the asymptotic relation between the free energy per site and the radius of curvature on the dual lattice geometry

$$\mathcal{F}^{[\infty]}_{(p,q)} - \mathcal{F}^{[\infty]}_{(\infty,q)} \propto \frac{\partial}{\partial p}\mathcal{R}^{-1}_{(q,p)} \approx -\frac{\pi}{2}\exp\left[\frac{1}{2}\mathcal{R}^{-1}_{(q,p)}\right], \tag{3.42}$$

which is valid for any fixed $q \geq 4$ and $p \gg 4$ (typically $p \gtrsim 10^2$) at low temperatures.

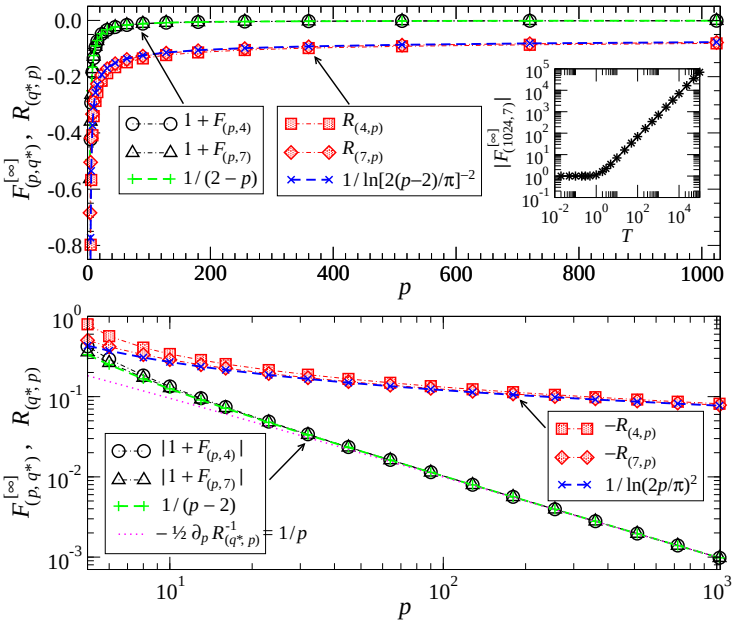

Figure 3.17: The asymptotic behavior of the free energy per site $\mathcal{F}^{[\infty]}_{(p,q^*)} - \mathcal{F}^{[\infty]}_{(\infty,q^*)}$ for the Ising model at $T = 0.1$ and the Gaussian radius of curvature $\mathcal{R}_{(q^*,p)}$ for $q^* = 4$ and $q^* = 7$. The asymptotic fitting functions for the energy decay as $-\frac{1}{p}$, where the "+" symbols connected with the dashed line fit to the free energy data (the circles and the triangles). The asymptotics $\propto 1/\ln(2p/\pi)^{-2}$ of the radius of curvature (the squares and the diamonds) is plotted by the "$*$" symbols connected with the dashed line. The inset of the upper graphs shows the temperature dependence of $\mathcal{F}^{[\infty]}_{(\infty,q^*)}$. The log-log plot in the lower graph is used to enhance the asymptotics of the upper graph.

We have shown that the free energy of various spin models (or the ground-state energy for quantum spin systems) on the non-Euclidean lattice geometries reproduces the properties of the spatial geometry as we have demonstrated on the Gaussian radius of curvature. Necessity of other studies is inevitable to support our findings. The consequences of the current work are expected to elicit further research, which can bridge the quantum physics with the general theory of relativity.

Having analyzed the phase transition temperatures $T^{(p,q)}_{\rm pt}$ of the Ising model with respect to the lattice geometries (p,q), we again find another analogous relation for the scaling of the radius of Gaussian curvature

$$-1/\ln\left[T^{(p,q)}_{\rm pt}\right]^2 \propto \mathcal{R}_{(p,q)} \tag{3.43}$$

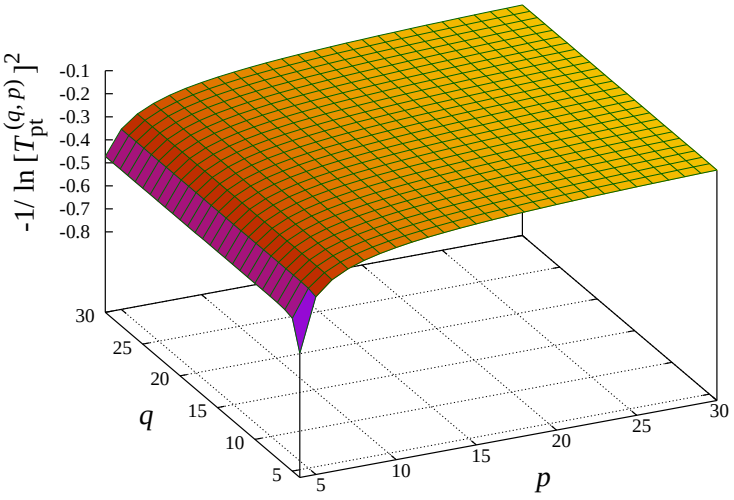

Figure 3.18: The rescaled phase transition temperatures with respect to p and q are shown in the dual geometry (q, p) to emphasize the similarity with the radius of Gaussian curvature in Fig. 3.15.

as shown in Fig. 3.18. For better visual comparison with Fig. 3.15, we plot $-1/[2\ln T_{\rm pt}^{(p,q)}]$ in the dual geometry (i.e., the meanings of p and q are swapped in the graph). Recall that the higher values of the coordination number q (for fixed p) cause that $T_{\rm pt}^{(p,q)} \propto q$, cf. Eq. (3.17), whereas if p increases (at fixed q), the fast convergence to the constant in Eq. (3.16) is achieved.

Hence, the evident mutual similarity of the functional p,q-dependence among the free energy per site (in Figs. 3.11, 3.12, 3.14), the radius of the Gaussian curvature (Fig. 3.15), and the phase transition temperature (Fig. 3.18) leads us to conjecture that a theoretical explanation should exist, which connects them all together. Or, in other words, our findings call for the necessity to formulate an appropriate theoretical explanation.

Chapter 4

Models of social behavior

4.1 Introduction

The last couple of years has witnessed an increasing interest in study of collective behavior of social systems. Social systems are composed of people (individuals), who interact with one another. These interactions influence the people engaged in them and after many interactions global properties, i.e., macro-level behavior of groups or whole societies, emerge. An essential question is how these local (microscopic) interactions lead to the global (macroscopic) properties of the system. This is a question that can be answered by tools of statistical physics, and the approach of statistical physics is used extensively in the study of collective phenomena.

One may ask, "Statistical physics is used for study of interacting particles, aren't humans astonishingly much more complicated?" And this is a valid objection! Inevitably, every modeling of social agents implies a severe simplification of the reality. The social agents are modeled by a rather limited set of variables representing their properties or state. The microscopic interaction among the agents should be defined sensibly and realistically to capture the dynamics of social behavior, which is, of course, not a trivial task. However, the concept known from statistical physics as *universality* says that the large scale phenomena do not depend on the microscopic details of the process, only on the higher level features, as symmetries, dimension or conservation laws. With this in mind, one can learn something about a system just by reproducing the most important properties of the elements and their interactions.

Study of social dynamics is a rapidly evolving area of scientific studies. It has its applications in disciplines as diverse as sociology, economics, political science, and anthropology. It is a really hard task to present the state of art in this subject. However, we found [Castellano et al., 2009] as a very useful work in this area.

Other resources will be referred to further in this part.

Major regularities can emerge spontaneously in social systems, as it is often seen in the real world. This can be understood as a disorder-order transition, and examples of such transitions are: the spontaneous formation of common language/culture, or the emergence of consensus on an issue, collective motion, a hierarchy. The drive toward the order is the tendency of agents to become alike as they interact. The term for this mechanism is *social influence* and it is analogous to ferromagnetic interaction in magnets. Ising model, briefly introduced in Subsection 1.1.1, is a model of ferromagnetic material. It can, however, be considered as a very simple model of opinion dynamics, wherein the agents are influenced by the state of the majority of their nearest neighbors.

One way of how to consider the unknown influence, or some hidden details of the social dynamics, is to introduce the noise, which corresponds to a variability in the states of the agents. A natural question arises, "Does the presence of a noise hinder the ordered state?" The role of noise in one particular model (the Axelrod model) is discussed in this Section.

Traditionally, the statistical physics deals with regular systems such as lattices, where the elements are located on the sites and interact only with the nearest neighbors, or with systems with all-to-all interactions. However, social interactions exhibit the interaction pattern which is denoted as complex networks. The role of topology is a highly studied topic in this context, nonetheless, our work is not concerned about it.

The simplest model of opinion formation is the Voter model. Each agent i in this model is endowed with a binary variable $s_i = \pm 1$. This variable represents for example the answer to the yes-no question. The interaction is defined by the following algorithm: first randomly select an agent i, choose one of his neighbors j at random, and then change the opinion of agent s_i to be equal to the opinion of selected neighbor s_j. This process mimics the homogenization of opinions, however, the convergence to a uniform state is not guaranteed, because the interactions are random and only between two agents at each step. For D-dimensional lattice, the described mechanism leads to the slow coarsening process, where spatially ordered regions grow, i.e, large regions tend to expand and "consume" the small regions, see Fig. 4.1.

The evolution of the system can be described by the density of active interfaces between ordered regions n_a. The following scaling of the evolution of Voter model was found in [Frachebourg and Krapivsky, 1996],

$$n_a(t) \sim \begin{cases} t^{-(2-d)/2} & D < 2, \\ 1/\ln(t) & D = 2, \\ a - bt^{-d/2} & D > 2. \end{cases} \tag{4.1}$$

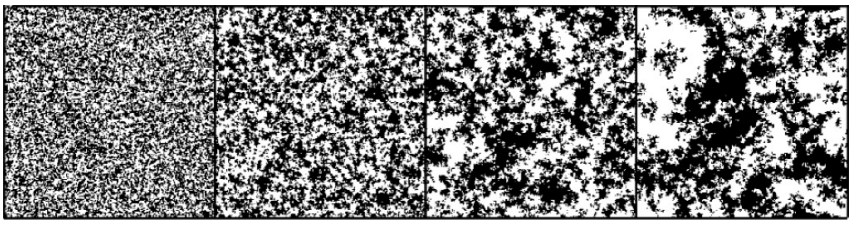

Figure 4.1: Evolution of the Voter model for agents located on the sites of a two-dimensional square lattice of linear size $L = 200$. Black dots represent opinions $+1$, while empty space represent opinions -1. From left to right the system, starting from a disordered configuration, is captured at times $t = 5, 50, 500, 1000$, where one step in time corresponds to N applications of updating rule described in the main text. (After [Dornic et al., 2001].)

For reader's orientation, some other models of opinion formation are: majority rule model, models of social impact, Sznajd model, and bounded confidence models. For more details concerning Voter model as well as the other models, see [Castellano et al., 2009] and [Barrat et al., 2008].

Besides opinion dynamics, much interest is focused on the related field of cultural dynamics. There is no sharp distinction between the two, however, in cultural dynamics each agent is described by a vector of variables instead of one scalar variable as we saw in opinion dynamics. Paradigmatic model of cultural dynamics is the Axelrod model, which we focus on in this Section.

As it should be clear from the text so far, our approach is to view the agents as adaptive instead of rational; with focus on communication rather than strategy. The latter approach is, however, also studied extensively; let us mention at least prisoner's dilemma, where agents (players) interact (play) pairwise and have two strategies which they can choose, i.e., they can either cooperate or not. For more details see the references in [Barrat et al., 2008].

Let us conclude this introduction with brief note about co-evolution of opinions and topology. So far, the topology of the network was considered to be fixed and served as a playground for a dynamical process. On the other hand, many real networks are of dynamical nature, i.e., the topology of such networks changes with time. The dynamical process taking place on the network can be coupled with the evolution of the topology. This is particularly relevant for social networks. One example is a link removal (or rewiring) between two agents with dissimilar opinions and creation of new links between two random agents, or with some preference between similar ones. There is a huge number of works concerning this topic, for references see [Barrat et al., 2008] and [Castellano et al., 2009].

4.1.1 The Axelrod model

Axelrod proposed a simple, yet ambitious, model of cultural assimilation and diversity, which is based on two mechanisms: social influence and *homophily* [Axelrod, 1997]. The former means, that after the interaction, people become more similar than before. In other words, communication reduces differences among the people. The latter is that the probability of social interaction depends on the similarity between two agents. It is based on the idea, that the more similar two people are, the easier the communication is. It might seem that this mechanism leads to homogenization of society. However, it can generate global polarization, where different cultures coexist. The mechanism of this model might be relevant for such topics as state formation, succession conflicts, transnational integration, or domestic cleavages.

Each agent has f different cultural *features*, $(\sigma_1, \sigma_2, \ldots, \sigma_f)$, and each of the feature can assume q different values (*traits*), $\sigma_\alpha = 0, 1, ..., q-1$. It means that each agent can be in one of q^f possible states. Each feature represents one of the cultural dimension, e.g., language, religion, technology, style of dress. Agents are placed on sites of a two-dimensional square lattice and can interact only with the nearest neighbors (long-range interactions are considered later). The dynamics runs in two steps as follows:

Step 1 An agent i and one of his neighbors j are selected randomly.

Step 2 The selected agents will interact with the probability proportional to the number of features for which they share the same value

$$\omega_{i,j} = \frac{1}{f} \sum_{\alpha=1}^{f} \delta(\sigma_\alpha(i), \sigma_\alpha(j)), \tag{4.2}$$

where $\delta(i, j)$ is Kronecker's delta. An interaction consists of selecting at random a feature on which the two agents differ, $\sigma_\alpha(i) \neq \sigma_\alpha(j)$, and setting this feature of the neighbor to be equal to $\sigma_\alpha(i)$.

These two steps are repeated as needed.

The described process can lead either to a global homogenization or to a fragmented state with coexistence of different homogeneous regions, see Fig. 4.2. As two agents do interact, they share more specific cultural features. More features tend to be shared over a larger area and a cultural region with all features being exactly the same can be created. Eventually, the system ends in a state where no other change is possible. The features of all neighbors are either identical or there is no match, and they do not interact. Several *stable regions* can be created; a question of interest is how many.

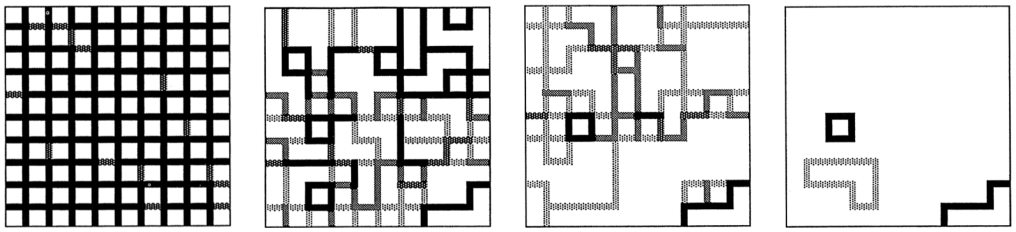

Figure 4.2: Four maps of cultural similarities. Simulation was conducted for lattice size 10×10, number of features is $f = 5$, number of possible values of each feature is $q = 10$. Cultural similarity (number of shared features) between adjacent agents is coded as black for $\omega_{ij} \leq 20\%$, dark grey for $\omega_{ij} = 40\%$, gray for $\omega_{ij} = 60\%$, light grey for $\omega_{ij} = 80\%$, and white for $\omega_{ij} = 100\%$; and t denotes the number of events (time evolution). (After [Axelrod, 1997].)

As f increases (with q being fixed) the probability of sharing at least one of the features is higher. In this case, the average number of stable regions (with respect to different runs) will decrease. On the contrary, as q increases (with f being fixed) the probability of sharing at least one of the features is smaller and thus the average number of stable regions will increase.

The long-range interactions have also been considered, i.e., interactions between second nearest neighbors, third nearest neighbors, etc. It is intuitively clear that if the agents could interact over larger distances, the process of cultural convergence would be made easier. The longer the interactions are allowed, the smaller is the average number of stable regions, as expected.

Another studied question is the dependence of the average number of stable regions on the size of the lattice (size of the territory). Axelrod provides some preliminary results which suggest that this number increases with the size of the lattice for small lattices and after certain size it decreases, see Fig. 4.3. Small lattices do not have enough space to contain many stable regions, thus it is understood this number increases as the size of the lattice increases. However, it is surprising that large lattices have fewer stable regions than moderately-sized lattices.

A detailed phase diagram of the model was studied in Ref. [Castellano et al., 2000]. The order parameter was defined as the average size of the largest stable region $\langle S_{\max} \rangle$. For fixed f, there is a critical value q_c such that $\langle S_{\max} \rangle$ increases with the system size L (number of sites is $N = L^2$) and tends to L^2 for $q < q_c$, and $\langle S_{\max} \rangle / L^2 \to 0$ for $q > q_c$. For two-dimensional lattices, the nature of this phase transitions depends on the value of f. For $f = 2$ this transition is continuous,

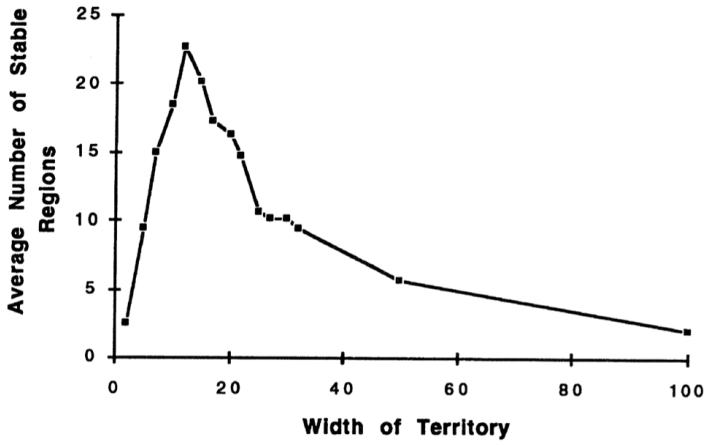

Figure 4.3: Dependence of the average number of stable regions on the size of the lattice L. $f = 5$, $q = 15$, results are averaged over 40 runs, except for lattice sizes 50×50 and 100×100, where it's only 10. (After [Axelrod, 1997].)

whereas for $f > 2$ it is discontinuous, see Fig. 4.4. For one-dimensional systems, the transition is continuous for all values of f [Klemm et al., 2003a].

Cultural drift can be modeled as a spontaneous change in a feature at a certain rate r. The order-disorder transition induced by a noise was demonstrated in [Klemm et al., 2003b]. The order-disorder transition induced by the noise depends on the value of q, with the dependence becoming weaker for larger values of q, see Fig. 4.5. For a small noise the system tends to homogeneity, because disordered configurations are unstable with respect to perturbations introduced by the noise. On the contrary, when the noise rate is large, system tends to heterogeneity, because disappearance of domains is compensated by creation of new ones.

The effect of the mass media can be modeled by an interaction of agents with a global field. In [Gonzalez-Avella et al., 2005] a global field was introduced representing a mass media cultural message as a set of f parameters, $M = (\mu_1, \mu_2, ..., \mu_f)$. Selected agent interacts with this field as if it was an agent with probability B, and with one of his actual neighbors with probability $1 - B$. Surprisingly, the global field favors the multicultural phase, in other words, q_c is smaller with addition of the global field and depends on B. For B larger than a threshold, such that $q_c(B^*) = 0$, only the disordered phase is present. A global coupling and a local non-uniform coupling were considered in [Gonzalez-Avella et al., 2006].

Social networks have complex topology; with respect to this, the Axelrod model was considered on networks with complex topological characteristics. For Watts-Strogatz two-dimensional networks, the previously defined q_c now grows as a disorder parameter increases [Klemm et al., 2002]. For random scale-free networks, q_c diverges with the size of the system as N^β (with $\beta \sim 0.4$ for Barabási-

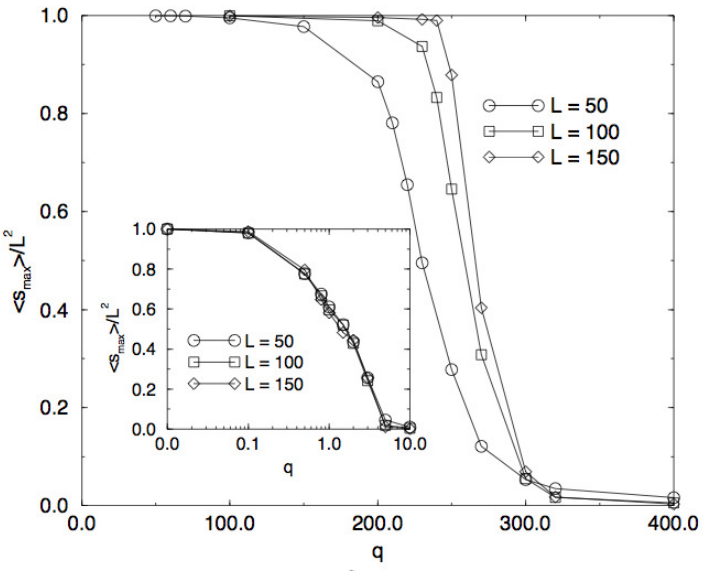

Figure 4.4: Behavior of the order parameter $\langle S_{\max} \rangle$ vs. q for three different system sizes and $f = 10$. The same quantity is reported for $f = 2$ in the inset. (After [Castellano et al., 2000].)

Albert networks), where N is the size of the network [Klemm et al., 2002].

4.1.2 Thermodynamic version of Axelrod model

In Ref. [Gandica et al., 2013], a thermodynamic version of the Axelrod model was proposed. Let us remark that the original Axelrod model is out of equilibrium, i.e, it does not satisfy equilibrium conditions as detailed balance[1] is violated. The

[1] We assume that each node i can be in one of the possible states, i.e., $\sigma_i = 1, 2, ..., \kappa$. The knowledge of the state of all nodes defines the microscopic state (microstate) $\sigma(t) = (\sigma_1(t), \sigma_2(t), \ldots, \sigma_N(t))$, where N is size of the network. Dynamical description of the system is given by the master equation. Simply, the master equation is evolution equation for probability $P(\sigma, t)$ of finding the system at time t in a microstate σ. In continuous time approximation, the master equation is

$$\partial_t P(\sigma, t) = \sum_{\sigma'} [P(\sigma', t) W(\sigma' \to \sigma) - P(\sigma, t) W(\sigma \to \sigma')], \tag{4.3}$$

where the terms $W(\sigma' \to \sigma)$ represent the transition rates from one microstate (configuration) to another. As we can see, the solution of the master equation provides only statistical information about the system evolution.

One of the interest is to find the stationary state of the system (if it exists) $\lim_{t \to +\infty} P(\sigma, t) = P_\infty(\sigma)$. Stationary distribution for equilibrium physical systems is given by well-known Boltzmann-Gibbs distribution $P_\infty(\sigma) = P_{\text{eq}}(\sigma) = \frac{\exp(-\mathcal{H}(\sigma)/k_B T)}{\mathcal{Z}}$, where $\mathcal{H}(\sigma)$ is the system's Hamiltonian. The partition function $\mathcal{Z}$ provides the proper normalization $\mathcal{Z} =$

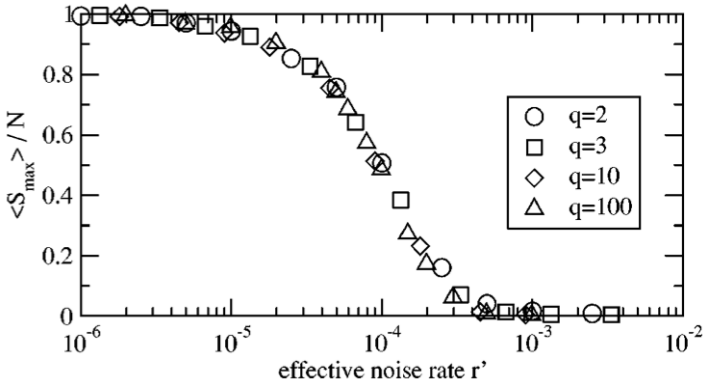

Figure 4.5: Universal scaling of the order parameter $\langle S_{\max}\rangle$ as a function of the effective noise rate $r' = r(1-1/q)$ for different values of q. Simulations have been run in systems of size $N = 50^2$ with $f = 10$. (After [Klemm et al., 2003b].)

Hamiltonian proposed by the authors is

$$\mathcal{H} = -\sum_{\alpha=1}^{f}\left[\sum_{\langle ij\rangle} J_{ij}\delta\left(\sigma_{i\alpha},\sigma_{j\alpha}\right) + h\sum_{i}\delta\left(\sigma_{i\alpha},h_{\alpha}\right)\right] \tag{4.4}$$

with the interaction factor

$$J_{ij} = \sum_{\alpha=1}^{f} J\delta(\sigma_{i\alpha},\sigma_{j\alpha}). \tag{4.5}$$

The index α denotes features, the indices i and j label the lattice sites where the agents are localized, and a cultural feature α of an agent i can take q values, $\sigma_{i\alpha} = 0,1,2,\ldots,q-1$. Here, h_α is the applied magnetic field with q values ($h_\alpha = 0,1,2,\ldots,q-1$), h is the magnitude of that field. The meaning of the interaction factor J_{ij} is such that it defines the number of shared features between two agents i and j multiplied by a constant J.

$\sum_\sigma \exp(-\mathcal{H}(\sigma)/k_{\mathrm{B}}T)$. The stationary distribution for the equilibrium system may be obtained by the system Hamiltonian and in this case we do not need to solve the master equation.

At equilibrium, each elementary process should be equilibrated by its reverse process. This is what the so-called *detailed balance condition* states

$$P_{\mathrm{eq}}(\sigma)W(\sigma\to\sigma') = P_{\mathrm{eq}}(\sigma')W(\sigma'\to\sigma).$$

One can see that this condition gives zero contribution for each pair on the right hand side of the master equation (4.3). The detailed balance is not necessary to fulfill $\partial_t P(t) = 0$, i.e., non-equilibrium systems can also reach stationary state but with more complicated cancellation relations in the master equation. Most of the real systems are actually non-equilibrium and we thus cannot use the equilibrium thermodynamic formulations.

The Hamiltonian (4.4) is inspired by the Potts model, however, the interaction factor J_{ij} depends on the global state of the f variables $(\sigma_{i1}, \sigma_{i2}, \ldots, \sigma_{if})$. Thermodynamic and critical properties were calculated analytically for one-dimensional case, where an order-disorder phase transition occurred at $T = 0$ regardless of f and q, in agreement with the one-dimensional Ising model [Baxter, 1982].

As we mentioned earlier, the Axelrod model was also studied with the addition of a noise (which represents cultural drift). It was shown, that for the noise rate $r < r_c$, the system converges to a monocultural state, whereas for $r > r_c$ the system converges to a multicultural state, where r_c is a certain critical value of the noise rate and depends on the system size, not on q [Klemm et al., 2005, Klemm et al., 2003b, Toral and Tessone, 2007]. In the one-dimensional case, r_c scales as $r_c \sim 1/N^2$ with the size of the system, and, of course, in the thermodynamic limit $(N \to \infty)$ there is no phase transition, and for any positive r the system converges to a multicultural state. In this sense, the noise rate r corresponds to temperature T.

4.2 Thermodynamic model of social influence

In this Section, we consider a classical multi-spin model of a social system treated from the point of view of the statistical mechanics. We focus our attention on behavior of a model of a large society in equilibrium. The society is represented by individuals who mutually interact via communication channels (e.g. sharing interests) with the nearest neighbors only. The society is subject to special rules given by a model of the statistical mechanics we have introduced for this purpose. A noise plays an important role in this study. The noise interferes with the communication channels. If it increases, the communicating individuals get less correlated on larger distances. In this way, the noise acts against the formation of larger clusters of the individuals with a particular character, i.e., a set of shared features. In such a cluster, the individuals share a similar social background. The size of the clusters can be quantified by calculations of an appropriate order parameter, correlation length, etc., which are commonly used in the statistical physics. If a phase transition point exists in a given statistical model, this point separates an ordered phase from the disordered. The two phases can be determined by the order parameter being nonzero within the ordered phase or zero in the disordered, provided that the system is infinitely (sufficiently) large, and the spontaneous symmetry-breaking mechanism occurred below the transition point. The noise can be also regarded as random perturbations (cultural drift) realized as a spontaneous change in a trait [Klemm et al., 2003b] and can play a significant constructive role in the out-of-equilibrium Axelrod model. On the other hand, the effect of the noise for such non-linear dynamical systems is found to be

size-dependent [Toral and Tessone, 2007].

We, therefore, propose a multi-state spin model on the two-dimensional regular square lattice of the infinite size. Each vertex of the lattice contains a multi-state spin variable (being an individual with a certain cultural setting). We define special nearest-neighbor interactions among the spins representing a conditional communication among individuals. The statistical Gibbs distribution introduces thermal fluctuations into our model with a multi-spin Hamiltonian. Here, the temperature can be identified as the noise we introduced above. Imposing a constant magnetic field on given spin states makes the spins align accordingly, which might have had a similar effect as, for instance, the mass media or advertisement. Having calculated the effects of the magnetic field, we observed a typical paramagnetic response in our model only, and no phase transition was observed.

The model describes thermodynamic features of social influence studied by the well-known Axelrod model [Axelrod, 1997], which is explained in Subsection 4.1.1 earlier in this Chapter. Gandica *et al.* [Gandica et al., 2013] have recently studied such thermodynamics features in the coupled Potts models in one-dimensional lattices, where the phase transition occurs at zero temperature in accord with a thermodynamic one-dimensional interacting multi-state spin system as summarized in Subsection 4.1.2. Our studies go beyond this thermodynamic Axelrod model conjectures since we intend to study phase transitions on social systems at nonzero temperature, where number of the individuals is infinite. Therefore, the spontaneous symmetry-breaking mechanism selects a certain preferred cultural character resulting in a large cluster formation, which is characterized by a nonzero order parameter.

This task is certainly nontrivial since our model has not been known to have an analytical solution. Therefore, we apply the CTMRG algorithm [Nishino and Okunishi, 1996], which is a powerful numerical tool in the statistical mechanics, see Section 2.2. The CTMRG calculates all thermodynamic functions to a high accuracy and enables to analyze the phase transitions as well as to control the spontaneous symmetry breaking. The phase transition temperature decreases with increasing number of traits q as discussed later. We intend to investigate the asymptotic case in this work, i.e., the case when the number of the traits q of each individual is infinite. Then, we estimate the phase transition point in order to find out whether the ordered phase is permanently present or not. In other words, the phase transition point T_t is found to remain nonzero. Throughout this work we consider the case of $f = 2$ only.

4.2.1 Lattice model

Hamiltonian

A classical spin lattice model is considered on the regular two-dimensional square lattice, where the nearest-neighbor multi-state spins placed on the lattice vertices interact. Let $\sigma_{i,j} = 0, 1, \ldots, n-1$ be a generalized multi-spin with integer degrees of freedom n. The subscript indices i and j denote the position of each lattice vertex, where the spins are placed within the X and Y coordinate system on the underlying lattice, i.e., $-\infty < i, j < \infty$. We start with the n-state clock (vector) model [Gendiar et al., 2008] for this purpose with the Hamiltonian

$$\mathcal{H} = -J \sum_{i=-\infty}^{\infty} \sum_{j=-\infty}^{\infty} \sum_{k=0}^{1} \cos(\theta_{i,j} - \theta_{i+k,j-k+1}) \,. \tag{4.6}$$

The interaction term J acts between the nearest-neighbor vector spins $\theta_{i,j} = \dfrac{2\pi}{n}\sigma_{i,j}$. The k summation includes the horizontal and the vertical directions on the square lattice.

Let us generalize the spin clock model so that the interaction term J contains a special attribute, i.e., extra spins are added. We, therefore, introduce additional degrees of freedom to each vertex. The Hamiltonian in Eq. (4.6) can be further modified into the form $\mathcal{H} = \sum_{ijk} J_{ijk} \cos(\theta_{i,j} - \theta_{i+k,j-k+1})$. The position dependent term J_{ijk} describes the spin interactions J of the n-state clock model controlled by additional q-state Potts model δ-interactions [Wu, 1982]. The total number of the spin degrees of the freedom is nq on each vertex i, j. We study the simplified case when $q \equiv n$ starting from the case of $q = 2$ up to $q = 6$ which is still computationally feasible. (In more general case when $q \neq n$, we do not expect substantially different physical consequences as those studied in this work.)

Hence, our multi-state spin model contains two q-state spins on the same vertex, i.e., $\sigma^{(1)}_{i,j} = 0, 1, 2, \ldots, q-1$ and $\sigma^{(2)}_{i,j} = 0, 1, 2, \ldots, q-1$, which are distinguished by the superscripts (1) and (2). It is instructive to introduce a q^2-variable $\xi_{i,j} = q\sigma^{(1)}_{i,j} + \sigma^{(2)}_{i,j} = 0, 1, \ldots, q^2 - 1$. The Hamiltonian of our model has its final form

$$\mathcal{H} = \sum_{i,j=-\infty}^{\infty} \sum_{k=0}^{1} \left\{ J^{(1)}_{ijk} \cos\left[\theta^{(2)}_{i,j} - \theta^{(2)}_{i+k,j-k+1}\right] + J^{(2)}_{ijk} \cos\left[\theta^{(1)}_{i,j} - \theta^{(1)}_{i+k,j-k+1}\right] \right\}, \tag{4.7}$$

noticing that $\theta^{(\alpha)}_{i,j} = 2\pi\sigma^{(\alpha)}_{i,j}/q$, where

$$J^{(\alpha)}_{ijk} = -J\delta\left(\sigma^{(\alpha)}_{i,j}, \sigma^{(\alpha)}_{i+k,j-k+1}\right) \equiv \begin{cases} -J, & \text{if } \sigma^{(\alpha)}_{i,j} = \sigma^{(\alpha)}_{i+k,j-k+1}, \\ 0, & \text{otherwise.} \end{cases} \tag{4.8}$$

The superscript (α) can take only two values as mentioned above. The Potts-like interaction $J^{(\alpha)}_{ijk}$ is represented by a diagonal $q \times q$ matrix with the elements $-J$ on the diagonal.

Thus defined model can also describe conditionally communicating (interacting) individuals of a society. The society is modeled by individuals $(\xi_{i,j})$ and each individual has two distinguished features $\sigma^{(1)}$ and $\sigma^{(2)}$. Each feature assumes q different values (traits). In particular, an individual positioned on $\{i, j\}$ vertex of the square lattice communicates with a nearest neighbor, say $\{i+1, j\}$, by comparing the spin values of the first feature $\sigma^{(1)}$. This comparison is carried out by means of the q-state Potts interaction. If the Potts interaction is nonzero, the individuals communicate via the q-state clock interaction of the other feature with $\alpha = 2$. The cosine enables a broader communication spectrum than the Potts term. Since we require symmetry in the *Potts-clock* conditional communication, we include the other term in the Hamiltonian, which exchanges the role of the features (1) and (2) in our model. In particular, the Potts-like communication first compares the feature $J^{(2)}_{ijk}$ followed by the cosine term with the feature $\alpha = 1$. (Enabling extra interactions between the two features within each individual and/or the cross-interactions of the two adjacent individuals is to be studied elsewhere.) The total number of all the individuals is considered to be infinite in order to detect and analyze the phase transition when the spontaneous symmetry breaking is present.

In the framework of the statistical mechanics, we investigate a combined q-state Potts and q-state clock model which is abbreviated as the q^2-state spin model. As an example, one can interpret the case of $q = 3$ in the following: the feature $\sigma^{(1)}$ can be chosen to represent *leisure-time interests* while the other feature $\sigma^{(2)}$ can involve *working duties*. In the former case, one could list three properties such as reading books, listening to music, and hiking, whereas the latter feature could consist of manual activities, intellectual activities, and creative activities, as the example. The thermal fluctuations, induced by the thermodynamic temperature T of the Gibbs distribution, are meant to describe a noise hindering the communication. The higher the noise, the stronger suppression of the communication is resulted.

Density matrix

We classify the phase transitions of our model by numerical calculation of the partition function $\mathcal{Z}$

$$\mathcal{Z} = \sum_{\{\sigma\}} \exp\left(-\frac{\mathcal{H}}{k_B T}\right), \tag{4.9}$$

especially, by its derivatives. The sum has to be taken through all multi-spin configurations $\{\sigma\}$ on the infinite lattice. The partition function is evaluated numerically by the CTMRG algorithm.

A typical formulation of an observable (an averaged thermodynamic function) $\langle \hat{X} \rangle$ obeys the standard expression

$$\langle \hat{X} \rangle = \mathcal{Z}^{-1} \sum_{\{\sigma\}} \hat{X} \exp\left(-\frac{\mathcal{H}\{\sigma\}}{k_B T}\right) \equiv \mathrm{Tr}_s \left(\hat{X}\hat{\rho}_s\right), \tag{4.10}$$

where the matrix $\hat{\rho}_s$ is introduced being commonly called the *reduced density matrix*

$$\hat{\rho}_s = \mathcal{Z}^{-1} \sum_{\{\sigma_e\}} \exp\left(-\frac{\mathcal{H}\{\sigma\}}{k_B T}\right). \tag{4.11}$$

It is a classical counterpart of the one-dimensional quantum reduced density matrix in DMRG defined for a subsystem s in contact with an environment e. The reduced density matrix is defined on a line of the spins $\{\sigma_s\}$ (forming the subsystem s) between any of the two adjacent corner transfer matrices, whereas all the remaining spins variables form the environment e. The configuration sum is taken over all spins within the environment $\{\sigma_e\}$ except those of the subsystem $\{\sigma_s\}$. Notice the normalization $\mathrm{Tr}_s \hat{\rho}_s = 1$. Its meaning is the partition function $\mathcal{Z}$ within the classical statistical physics and is normalized to unity, compare with the definitions in Section 2.2.

An important thermodynamic function to be calculated is the *entanglement von Neumann entropy* S_v. It follows the standard quantum-mechanical definition

$$S_v = -\mathrm{Tr}_s \left(\hat{\rho}_s \log_2 \hat{\rho}_s\right). \tag{4.12}$$

This quantity reflects the correlation effects, which are maximal at the phase transition point.

Our model can be thought of as a system with two non-trivially coupled sublattices, where either sub-lattice is composed of the q-state variables with the given feature α.

Order parameters

The order parameter $\langle O \rangle$ can be evaluated via the reduced density matrix in Eq. (4.11) being either nonzero within an ordered spin phase or zero in the disordered. A continuous transition usually leads to the second-order phase transition, and the discontinuous behavior signals the first-order phase transition. However, a detailed analysis of the free energy and other thermodynamic functions is usually necessary to distinguish the order of the phase transition.

Let us define a *sub-site* order parameter for a given feature α

$$\langle O_\alpha \rangle = \mathrm{Tr}_s \left(\hat{O}_s^{(\alpha)} \hat{\rho}_s \right) = \mathrm{Tr}_s \left[\cos\left(\frac{2\pi \sigma_{i,j}^{(\alpha)}}{q} \right) \hat{\rho}_s \right], \tag{4.13}$$

where the sub-site order parameter $\hat{O}_s^{(\alpha)}$ is measured. For simplicity, we excluded the subscripts i, j from the order parameter notation. Another useful definition of the order parameter, measuring both of the spins at the same vertex, is a *complete* order parameter

$$\langle O \rangle = \mathrm{Tr}_s \left(\hat{O}_s \hat{\rho}_s \right) = \mathrm{Tr}_s \left[\cos\left(2\pi \frac{\xi_{i,j} - \phi}{q^2} \right) \hat{\rho}_s \right]. \tag{4.14}$$

Again, we simplified the expression into $\xi = q\sigma^{(1)} + \sigma^{(2)}$. We also extended the definition of the complete order parameter by introducing a q^2-state fixed parameter ϕ. This parameter ϕ specifies the alignment of $\langle O \rangle$ towards a reference spin level, where the multi-state spin projections are measured. Unless stated explicitly in the text, we often consider the parameter $\phi = 0$.

If the magnetic field h is set to be nonzero, the thermodynamic functions are always analytic within all temperature range, and no phase transition point is detected. Figure 4.6 shows this case for $h = 0$ and $h = 0.1$ if we applied CTMRG to the model Hamiltonian studied in Ref. [Gandica et al., 2013] on the two-dimensional square lattice. It is evident that for zero field the dashed ($q = 2$) and the full ($q = 3$) lines exhibit the continuous phase transitions with the critical temperatures and exponents $T_c = 3.0012, \beta \approx \frac{1}{10}$ and $T_c = 2.5676, \beta \approx \frac{1}{20}$, respectively. Applying the magnetic field $h = 0.1$, the phase transition is not present, and the model responds in the standard paramagnetic way for $q = 2$ (dotted line) and $q = 3$ (the dashed-dotted line). Since we are interested in the phase transition analysis of our model, we exclude detailed analysis with nonzero magnetic field in our model.

4.2.2 Numerical results

The phase transitions in the classical spin systems are induced by the thermal fluctuations by varying the temperature T in Eq. (4.9). We use dimensionless units, in which $J = k_\mathrm{B} = 1$. This corresponds to the ferromagnetic spin ordering. We begin with the simplest non-trivial case of $q = 2$. Figure 4.7 shows the sub-site order parameter $\langle O_\alpha \rangle$ with respect to temperature T which is identical for both $\alpha = 1$ and $\alpha = 2$. The second order phase transition is resulted at the critical temperature $T_c = 2.1973$. The associated universality scaling $\langle O_\alpha \rangle \propto (T - T_c)^\beta$ results in the common critical exponent $\beta \approx 0.1113$. The inset shows nearly linear behavior

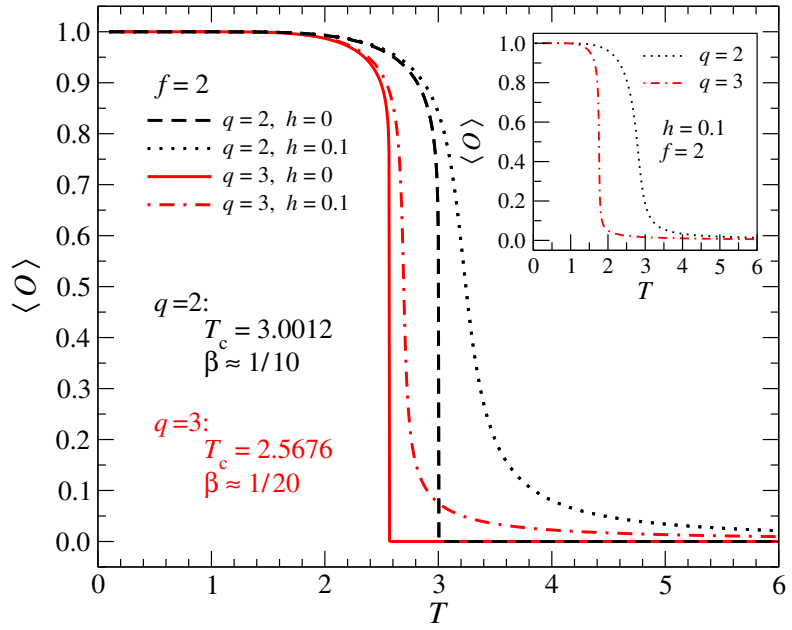

Figure 4.6: The temperature dependence of the complete order parameter $\langle O \rangle$ on the two-dimensional square lattice of the thermodynamic version of the Axelrod model studied in Ref. [Gandica et al., 2013] in the case of $f = 2$. A typical response of the model on the magnetic field h is shown for $q = 2$ and $q = 3$. (The inset depicts supplemental information on our model Hamiltonian in Eq.(4.7) if the magnetic field $h = 0.1$ is imposed.)

of $\langle O_\alpha \rangle^{1/\beta}$ when approaching the critical temperature T from the ferromagnetic phase. The critical exponent of our model at $q = 2$ is very close to the 3-state Potts model universality class [Wu, 1982], where $\beta = \frac{1}{9}$. This model analogy is non-trivial and requires further clarification. Notice that the exponent $\beta \approx 0.1113$ differs from the well-known Ising (2-state clock) universality, where $\beta = \frac{1}{8}$. It belongs neither to the 4-state Potts nor the 4-state clock model universality classes.

The sub-site order parameter $\langle O_\alpha \rangle$ for $q = 3$, 4, and 5 is depicted in Fig. 4.8. It gradually decreases with increasing temperature, but at certain temperature it discontinuously jumps to zero. Such behavior usually suggests the first order phase transition. To confirm this statement, the normalized Helmholtz free energy $F = -k_B T \ln \mathcal{Z}$ per spin is plotted with respect to T for two different boundary conditions (BCs). The fixed (open) BCs are imposed at the very beginning of the iterative CTMRG scheme in order to enhance (suppress) spontaneous symmetry breaking resulting in the ordered (disordered) phase in a small vicinity of the phase transition point. In particular, if the fixed BCs are applied, the spontaneous symmetry-breaking mechanism selects one of q^2 free energy minima as specified

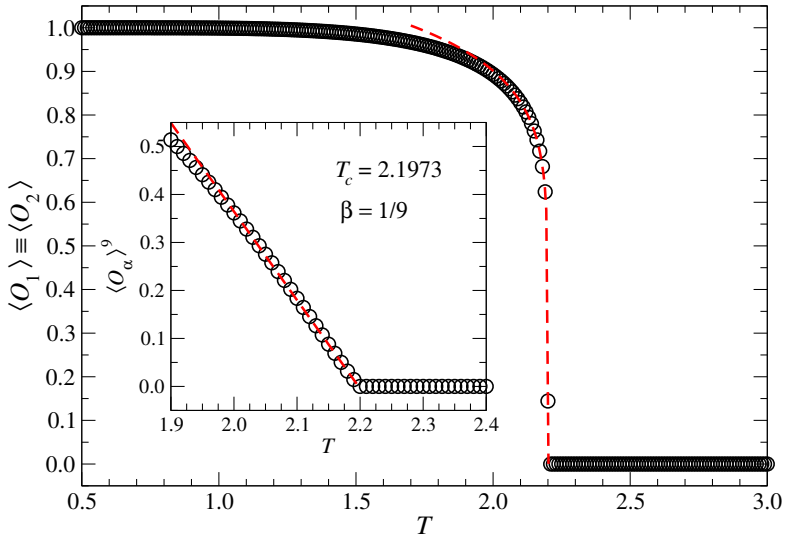

Figure 4.7: The temperature dependence of the sub-site order parameter $\langle O_\alpha \rangle$ (black circles) for $f = 2$ and $q = 2$ remains unchanged for both $\alpha = 1, 2$. The red dashed line corresponds to the scaling relation with the critical exponent $\beta \approx 0.1113$. The inset depicts the ninth power of $\langle O_\alpha \rangle$ with the expected linearity below T_c.

by the fixed BCs. On the contrary, the open BCs prevent the spontaneous symmetry breaking from falling into a minimum and makes the system be in a metastable state below the phase transition. Since the first-order phase transition is known to exhibit the coexistence of two phases in a small temperature interval around the phase transition, such an analysis with the two different BCs is inevitable to locate the phase transition accurately. The insets for the three cases, $q = 3, 4, 5$, show the normalized Helmholtz free energy around the transition temperature. The red and blue symbols of the free energy correspond to the fixed and the open BCs, respectively. The temperature interval, in which two distinguishable converged free energy are measured according to BCs set, is the region, where the ordered and disordered phases can coexist. The true phase transition point $T_t(q)$ is located at the free energy crossover, and the equilibrium free energy is shown by the thick dashed line corresponding to the lower free energy. In this case, the free energy is a non-analytical at $T_t(q > 2)$ and exhibits a kink typical for the first-order phase transition (further details on the first order analysis are can be found in Ref. [Gendiar and Nishino, 2002]). Taking the derivatives of F with respect to T, a discontinuity of the thermodynamic functions in Eqs. (1.6) and (1.7) is resulted. (We remark here that the free energy is not sensitive to the different BCs if a critical second-order phase transition is present, i.e., if $q = 2$.)

The phase transition temperatures for $q > 2$ are calculated within a high ac-

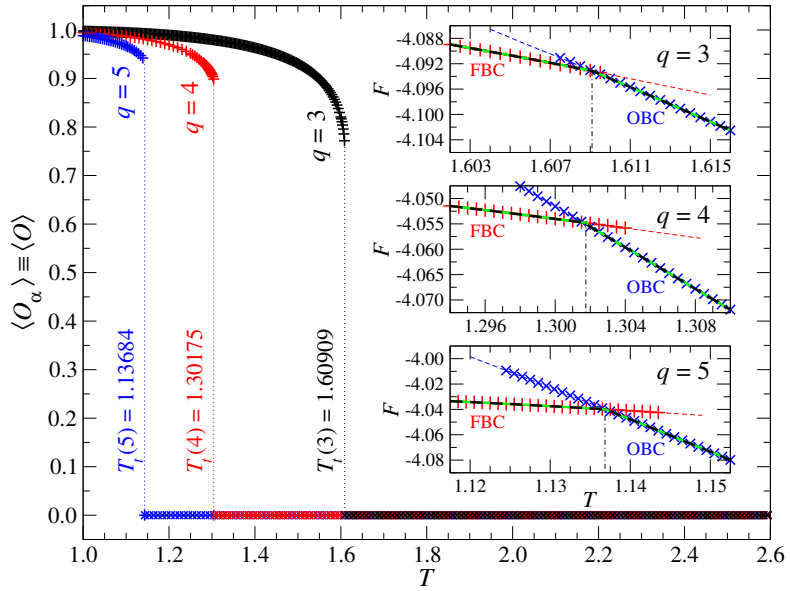

Figure 4.8: The order parameter $\langle O_\alpha \rangle$ is discontinuous for $q \geq 3$ ($f = 2$) and reflects the first order phase transition in all three cases when $3 \leq q \leq 5$. The free energy F is depicted in the respective three insets. We compare F for the fixed BCs (red symbols) and for the open BCs (blue symbols) around the transition temperature.

curacy resulting $T_t(3) = 1.60909$, $T_t(4) = 1.30175$, $T_t(5) = 1.12684$, and $T_t(6) = 1.03234$ (not plotted) at the crossing point of the free energy. It is obvious that $T_t(q)$ gradually decreases with increasing q, and later we study the asymptotic case when $q \to \infty$. It is also worth to mention that the first-order phase transition is not critical in sense of the non-diverging correlation length at the phase transition temperature (not shown) in contrast to the second order phase transition, when the correlation length diverges. For this reason, we reserve the term *critical* temperature, $T_c(q)$, for the second-order phase transition only, which is resulted in our model only if $q = 2$. Otherwise, we use the notation *transition* temperature $T_t(q)$.

The entanglement von Neumann entropy S_v when $q = 2$ is plotted in Fig. 4.9. Evidently, our calculations of S_v result in two maxima, not only a single maximum as expected for the single phase transition observed in Fig. 4.7. Hence, the entanglement entropy can indicate the existence of another phase transition, which could not be detected by the sub-site order parameter $\langle O_\alpha \rangle$. The phase transition at lower temperature, $T_{c,1}(q = 2) = 2.1973$, coincides with the one plotted in Fig. 4.7, whereas the higher-temperature phase transition appears at $T_{c,2}(q = 2) = 2.57$. To support this result obtained by S_v, we also calculated the specific heat C, as shown

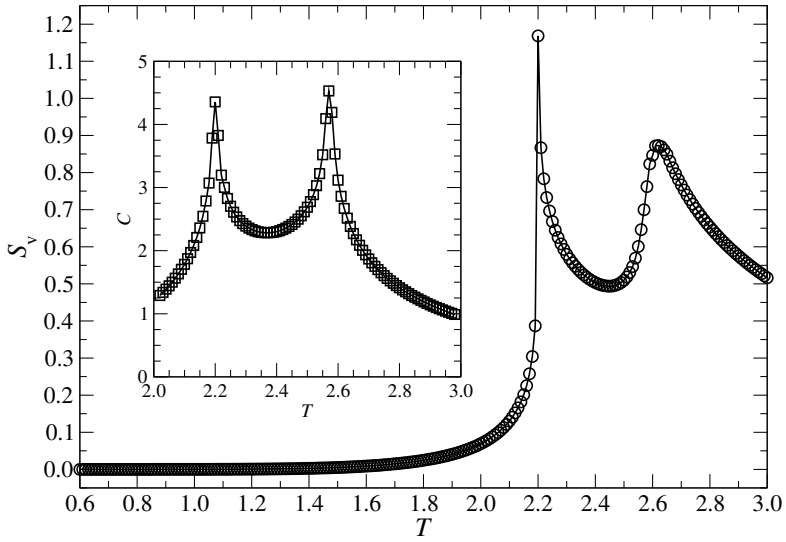

Figure 4.9: The temperature dependence of the entanglement entropy S_v for $q = 2$ and $f = 2$. The first maximum in S_v coincides with the critical temperature $T_{c,1}(2)$ plotted in Fig. 4.7, and the second transition appears at $T_{c,2}(2) = 2.57$. The specific heat, plotted in the inset, reveals two maxima corresponding to the phase transition temperatures $T_{c,1}(2)$ and $T_{c,2}(2)$.

in the inset. There are two evident maxima in C, which remain present in our model at the identical critical temperatures $T_{c,1}(2)$ and $T_{c,2}(2)$. The sub-site order parameter $\langle O_\alpha \rangle$ in Fig. 4.7 has not reflected the higher-temperature phase transition at all. Thus, we have achieved a new phase transition point, which is likely pointing to a topological ordering. A second-order transition has been found in the out-of-equilibrium Axelrod model [Radillo-Díaz et al., 2009]. In addition, the existence of modulated order parameter with two different phase transition temperatures has been reported earlier, often being associated with experimental measurements of the magnetization in crystal alloys [Ito et al., 1988, Sakon et al., 2013].

The entanglement entropy S_v exhibits a single maximum for any $q > 2$ as seen in Fig. 4.10. The discontinuity of S_v at the phase transition temperature $T_t(q)$ is characteristic for the first order phase transition. The three insets display the specific heat with the single maximum for each $q > 2$ at the transition temperature, which is in full agreement with the sub-site order parameter. Therefore, we conclude the existence of the single phase transition point of the first order if $q > 2$.

Figure 4.11 shows the complete order parameter when $q = 2$ as defined in Eq. (4.14). Obviously, the non-analytic behavior of $\langle O \rangle$ points to the two distinguishable critical temperatures $T_{c,1}(2)$ and $T_{c,2}(2)$, which completely coincide with the critical temperatures depicted in Fig. 4.9. Since the q^2-state spin ξ has

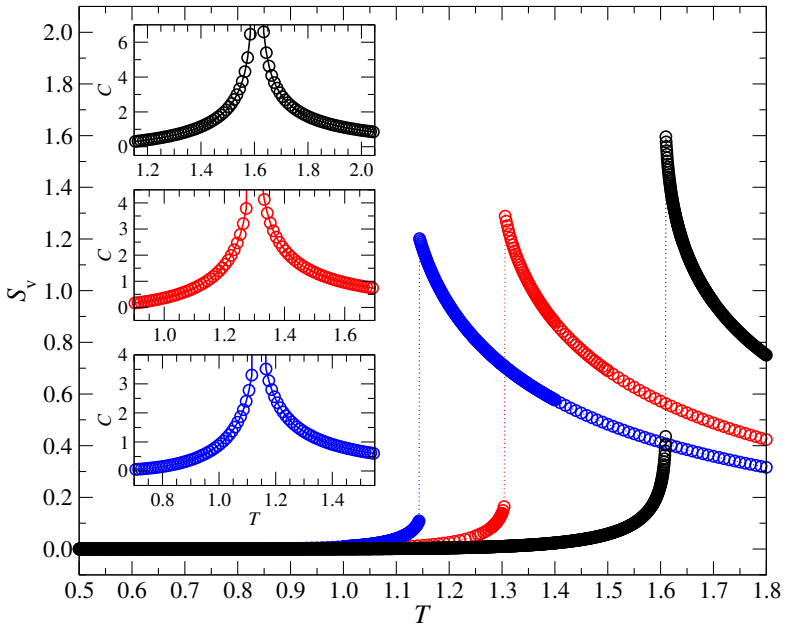

Figure 4.10: The entanglement von Neumann entropy for $q = 3$ (black), $q = 4$ (red), and $q = 5$ (blue) shows a single maximum when $f = 2$. Inset: the specific heat C also reflects the single (first-order) phase transition temperature.

four degrees of freedom, by targeting the parameters $\phi = 0, 1, 2, 3$ separately, the complete order parameter is explicitly evaluated. It satisfies the condition that the sum of all four complete order parameters at any temperature has to be zero. The mechanism of the spontaneous symmetry breaking at low temperatures causes that the free energy is four-fold degenerate at most. This is related to the four equivalent free energy minima with respect to the complete order parameter. Accessing any of the four free energy minima is numerically feasible by targeting the reference spin state ϕ.

Let us denote the four spin state at the vertex by the notation $|\sigma^{(1)}\sigma^{(2)}\rangle$. There are four possible scenarios for the order parameter $\langle O\rangle$ as shown in Fig. 4.11. These scenarios are depicted by the black circles ($\phi = 0$), the red diamonds ($\phi = 1$), the blue squares ($\phi = 2$), and the green triangles ($\phi = 3$), which correspond to the following vertex configurations $|\uparrow\uparrow\rangle$, $|\uparrow\downarrow\rangle$, $|\downarrow\uparrow\rangle$, and $|\downarrow\downarrow\rangle$, respectively.

At zero temperature there are three minima of the free energy leading to the three different complete order parameters $\langle O\rangle$ being -1, 0, and $+1$. There are four minima of the free energy if $0 < T < T_{c,1}(2)$ so that the order parameter has four different values $\langle O\rangle = -1 + \varepsilon$, $-\varepsilon$, $+\varepsilon$, and $+1 - \varepsilon$ with the condition $0 < \varepsilon \leq \frac{1}{2}$. It means the two states share the same free energy minimum when the order parameter is zero at $T = 0$ and $\varepsilon = 0$. In the temperature interval $T_{c,1}(2) \leq$

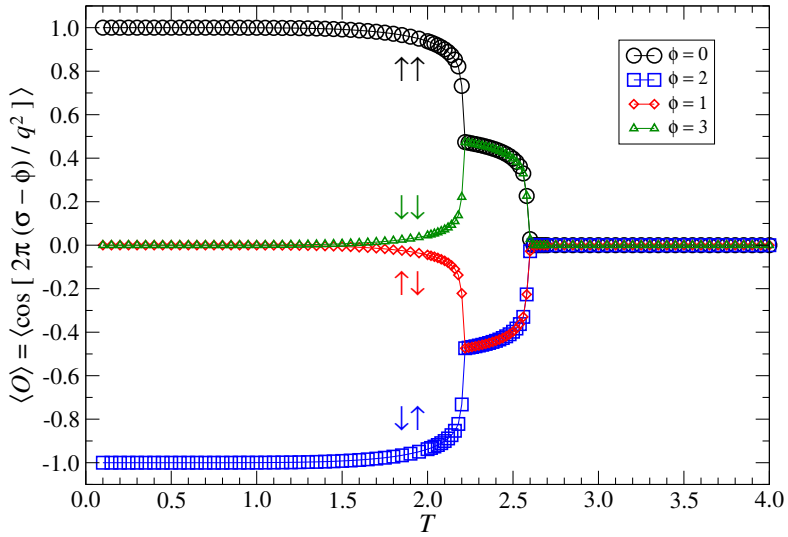

Figure 4.11: The complete order parameter acting on the q^2-state variable ξ exhibits the presence of the two phase transition temperatures if $q = 2$ and $f = 2$. All of the four reference spin levels (labeled by ϕ) are displayed after the spontaneous symmetry breaking occurs.

$T < T_{c,2}(2)$, there are only two free energy minima present and the order parameter pair for $\phi = 0$ and $\phi = 3$ becomes identical as well as the pair for $\phi = 1$ and $\phi = 2$. The only single free energy minimum is resulted at $T \geq T_{c,2}(2)$ when the order parameter is zero, which is typical for the disordered phase.

Let us stress that at the temperatures in between $T_{c,1}(2)$ and $T_{c,2}(2)$, the pair of the site configurations $|\uparrow\uparrow\rangle$ and $|\downarrow\downarrow\rangle$ is indistinguishable by the complete order parameter (i.e. the black and green symbols coincide), and the same topological uniformity happens for the pair of the site configurations $|\uparrow\downarrow\rangle$ and $|\downarrow\uparrow\rangle$. In other words, the anti-parallel alignments between the spins $\sigma^{(1)}$ and $\sigma^{(2)}$ are preferable in the temperature region $T_{c,1}(2) \leq T < T_{c,2}(2)$.

Notice that if the critical exponent β of the complete order parameter is calculated at the critical temperatures $T_{c,1}(2)$ and $T_{c,2}(2)$, we found out that $\beta \approx \frac{1}{18}$ if $T \to T_{c,1}(2)$, whereas the other exponent remains identical as discussed earlier, in particular, $\beta \approx \frac{1}{9}$ if $T \to T_{c,2}(2)$.

In the same analogy, we plotted the complete order parameter for $q = 3$ in Fig. 4.12. The free energy is five-fold degenerated at zero temperature unless the symmetry breaking mechanism (enhanced by ϕ) selects one of them. This mechanism results in the five distinguishable order parameters within $0 \leq \phi \leq 8$, which decouple into nine different order parameters when $0 < T < T_t(3)$. Just a single free energy minimum is characteristic in the disordered phase at $T \geq T_t(3)$ exhibiting a uniform $\langle O \rangle = 0$. In order to compare the main differences of

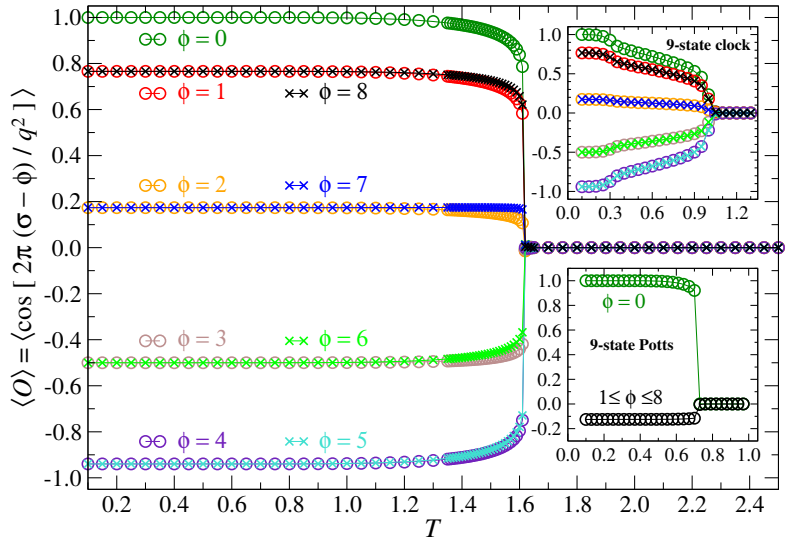

Figure 4.12: The complete order parameter acting on the q^2-state spin ξ for $q = 3$ if plotted with respect to the nine reference levels $\phi = 0, 1, ..., 8$ ($f = 2$). For comparison, the two insets show the order parameter of the standard 9-state clock model (the upper panel) and the standard 9-state Potts model (the lower panel) indexed by the reference levels ϕ.

the complete order parameter between our model and the standard 9-state clock model or the 9-state Potts models, we plotted the respective order parameter in the insets of Fig. 4.12. In the former case (the clock model) there are always five distinguishable order parameters originating in the five-fold degeneracy of the free energy, and the order parameters in our model and the 9-state clock model are identical at $T = 0$ only. However, the five-fold degeneracy remains within the interval $0 < T < T_t(3)$. (We remark that the BKT phase transitions [Kosterlitz and Thouless, 1973, Kosterlitz, 1974] of the infinite order is present in the $q \geq 5$-state clock models [Tobochnik, 1982].) In the latter case (the Potts model), there are only two distinguishable order parameters out of nine below the phase transition point. (Recall that the total sum of $\langle O \rangle$ over all ϕ is always zero. The discontinuity in the complete order parameter at $T_t(3)$ in our model and the 9-state Potts model reflects the first-order phase transition [Wu, 1982].

If the number of the spin degrees of freedom q is extrapolated toward the asymptotic limit, $q \to \infty$, a nonzero phase transition temperature $T_t(\infty)$ is resulted. We carried out the three independent extrapolations as depicted in Fig. 4.13 by means of the least square fitting. In particular, the power-law $T_t(q) = T_t(\infty) + a_0\, q^{-a_1}$, the exponential $T_t(q) = T_t(\infty) + a_0(1 - e^{-a_1/q})$, and the inverse proportional $T_t(q) = T_t(\infty) + a_0\, q^{-1}$ fitting functions were used to obtain $T_t(\infty)$, a_0, and a_1 parameters. All of them yielded the nonzero transition temperature $T_t(\infty) \approx 0.5$.

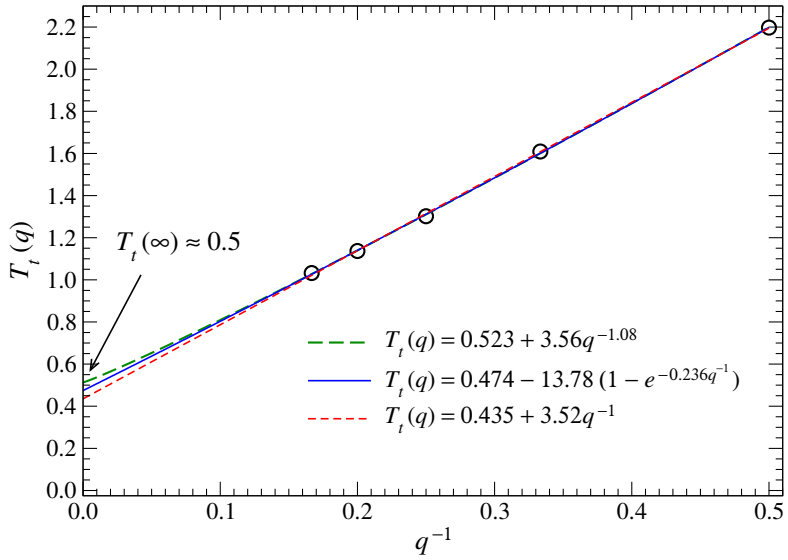

Figure 4.13: The there variants of the extrapolated transition temperature $T_t(q \to \infty)$ by the power-law fitting (the green long-dashed line), the exponential fitting (the blue full line), and the inverse proportionality (the red short-dashed line).

Out of these findings, we conjecture the existence of the ordered phase, i.e., the nonzero phase transition temperature $T_t(q)$ persists for any $q \geq 2$.

Chapter 5

Fractal geometries

A fractal is a geometric structure which exhibits the property of *self-similarity* at every scale, i.e., as we zoom in (or zoom out), the same (self-similar) pattern is repeated. Let us demonstrate this concept on the Sierpinski gasket, see Fig. 5.1. Each triangle can be decomposed into the three smaller triangles, which are the exact replicas of the original. For instance, zooming to the lower-left triangle (red), we obtain the triangle we have started with (for simplicity, only the six levels of the Sierpinski gasket are depicted).

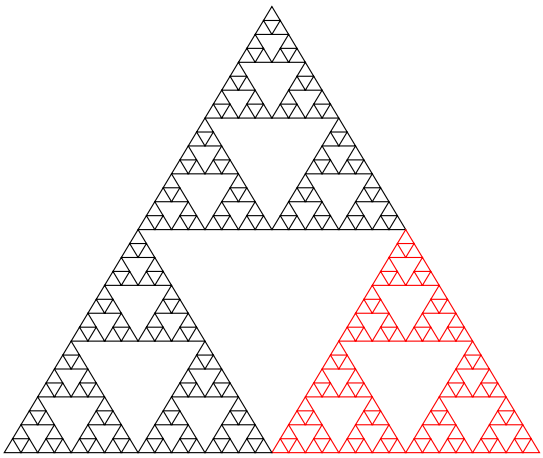

Figure 5.1: The Sierpinski gasket.

Another important property of the fractal is its fractional dimension. The Hausdorff dimension $d^{(\mathrm{H})}$ can be understood in terms of the relation

$$N = L^{d^{(\mathrm{H})}}, \tag{5.1}$$

where L is the linear dimension (i.e. the magnification factor) and N is the number of copies (i.e. the self-similar pieces). For example, doubling a line segment gives two copies of the original line (one dimensional case, $2 = 2^1$), doubling both the length and the width of a square gives four copies of the original square (two dimensional case, $4 = 2^2$), or doubling the all three linear dimensions of a cube gives eight copies of the original cube (three dimensional case, $8 = 2^3$), all in accord with Eq. (5.1). In the case of the Sierpinski gasket, doubling the linear dimension gives three copies of the original triangle, therefore $d^{(\mathrm{H})} = \ln 3 / \ln 2 \approx 1.585$.

The dimension can be also introduced in an alternative way, which may be even more relevant in the context of this work. It is reasonable to ask about the scaling of the size of the boundary M with respect to the linear dimension L

$$M = L^{d-1} . \tag{5.2}$$

Again, for example, doubling a line segment does not change the size of the boundary (which always consists of two points, thus $d = 1$), doubling the linear dimensions of a square increases the size of the boundary by a factor of two ($d = 2$), and doubling the linear dimensions of a cube increases the area of the cube by a factor of four ($d = 3$). Considering the lattices, the size of the boundary M naturally represents the number of outgoing bonds. Doubling the linear dimension of the Sierpinski gasket does not change the number of outgoing bonds, thus $d = 1$.

In this Chapter, the phase transition of the Ising model is investigated on a planar lattice that has a fractal structure. On the lattice, the number of bonds that cross the border of a finite area is doubled when the linear size of the area is extended by a factor of four. The free energy and the spontaneous magnetization of the system are obtained by means of the HOTRG method. Our modification of the HOTRG method used in the study is explained in Section 5.2. As shown in Section 5.3, the system exhibits an order-disorder phase transition, where the critical indices are different from those of the square-lattice Ising model. An exponential decay is observed in the density matrix spectrum even at the critical point. It is possible to interpret the system as being less entangled because of the fractal geometry.

5.1 Introduction

The phase transitions and critical phenomena have been one of the central issues in statistical analyses of the condensed matter physics [Domb et al., 2001]. When the second-order phase transition is observed, thermodynamic functions, such as

the free energy, the internal energy, and the magnetization, show non-trivial behavior around the transition temperature T_c [Fisher, 1974, Stanley, 1971], see also Section 1.1. This critical singularity reflects the absence of any scale length at T_c, and the power-law behavior of the thermodynamic functions around the transition can be explained by the concept of the renormalization group [Kadanoff, 1966, Efrati et al., 2014, Wilson and Kogut, 1974, Domb et al., 2001].

An analytic investigation of the renormalization group flow in φ^4-model shows that the Ising model exhibits a phase transition when the lattice dimension is larger than one, which is the lower critical dimension [Wilson and Kogut, 1974, Zinn-Justin, 1996]. In certain sense, the one-dimensional Ising model shows rescaled critical phenomena around $T_c = 0$. When the lattice dimension is larger than four, which is the upper critical dimension, and provided that the system is uniform, then the classical Ising model on regular lattices exhibits mean-field-like critical behavior.

Compared with the critical phenomena on regular lattices, much less is known on fractal lattices. Renormalization flow is investigated by Gefen et al., [Gefen et al., 1980, Gefen et al., 1983b, Gefen et al., 1983a, Gefen et al., 1984a] where correspondence between lattice structure and the values of critical indices is not fully understood in a quantitative manner. For example, the Ising model on the Sierpinski gasket does not exhibit any phase transition at any finite temperature, although the Hausdorff dimension of the lattice, $d^{(\mathrm{H})} = \ln 3/\ln 2 \approx 1.585$, is larger than one [Gefen et al., 1984b, Luscombe and Desai, 1985]. The absence of the phase transition could be explained by the fact that the number of interfaces, i.e. the outgoing bonds from a finite area, does not increase when the size of the area is doubled on the gasket. A non-trivial feature of this system is that there is a logarithmic scaling behavior in the internal energy toward zero temperature [Stošić et al., 1996]. The effect of anisotropy has been considered recently [Wang et al., 2013b]. In case of the Ising model on the Sierpinski carpet, presence of the phase transition is proved [Vezzani, 2003], and its critical indices were roughly estimated by Monte Carlo simulations [Carmona et al., 1998]. It should be noted that it is not easy to collect sufficient number of data points for finite-size scaling [Burkhardt and van Leeuwen, 1982] on such fractal lattices by means of Monte Carlo simulations, because of the exponential blow-up of the number of sites in a unit of fractal.

In this study, we investigate the Ising model on a planar fractal lattice, shown in Fig. 5.2. The lattice consists of vertices around the lattice points, which are denoted by the empty dots in the figure, where the Ising spins are positioned. The whole lattice is constructed by recursive extension processes, where the linear size of the system increases by the factor of four in each step. If the lattice is a regular square one, $4 \times 4 = 16$ units are connected in the extension process, whereas only 12 units are connected on this fractal lattice; 4 units are missing in the corners.

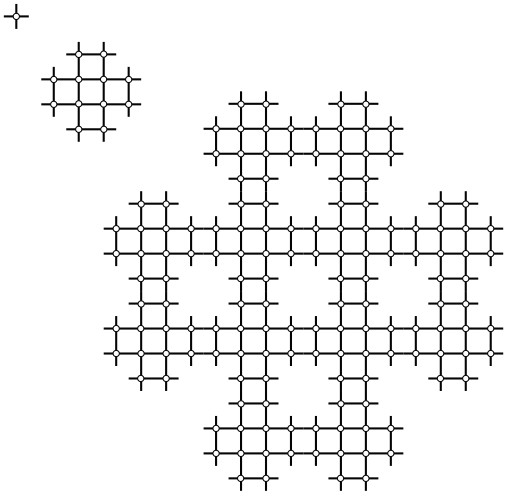

Figure 5.2: Composition of the fractal lattice. Upper left: a local vertex around an Ising spin shown by the empty dot in the zeroth iteration step $n = 0$. Middle: the basic cluster which contains $N_{n=1} = 12$ vertices in the first iteration step. Lower right: the extended cluster which contains $N_{n=2} = 12^2$ vertices at the second iteration step. In each step n of the system extension, the linear size of the system increases by the factor of 4, where only 12 units are linked, and where 4 units at the corners are missing, if it is compared with a 4 by 4 square cluster.

As a result, the number of sites contained in a cluster after n extensions is $N_n = 12^n$, and the Hausdorff dimension of this lattice is $d^{(\mathrm{H})} = \ln 12/\ln 4 \approx 1.792$. The number of outgoing bonds from a cluster is only doubled in each extension process since the sites and the bonds at each corner are missing. If we evaluate the lattice dimension from the second relation Eq. (5.2) between the linear dimension L and the number of outgoing bonds M, we get $d = 1.5$, since M is proportional to $\sqrt{L}$ on the fractal. Remark that the value is different from $d^{(\mathrm{H})} \approx 1.792$

5.2 Fractal meets HOTRG

The partition function of the Ising model defined on the fractal lattice can be represented as a tensor network state with three (four) types of the local tensors T, P ($P_{[\mathrm{Y}]}$ and $P_{[\mathrm{X}]}$), and Q (see Fig. 5.3),

$$T_{x_i x_i' y_i y_i'} = \sum_{\sigma} W_{\sigma x_i} W_{\sigma x_i'} W_{\sigma y_i} W_{\sigma y_i'}, \tag{5.3}$$

$$P_{[\mathrm{Y}]x_i x_i' s_i} = \sum_{\sigma} W_{\sigma x_i} W_{\sigma x_i'} W_{\sigma s_i}\,, \tag{5.4}$$

$$P_{[\mathrm{X}]y_i y_i' s_i} = \sum_{\sigma} W_{\sigma y_i} W_{\sigma y_i'} W_{\sigma s_i}\,, \tag{5.5}$$

$$Q_{x_i y_i} = \sum_{\sigma} W_{\sigma x_i} W_{\sigma y_i}\,, \tag{5.6}$$

where W is a 2×2 matrix determined by the bond weight factorization[1]. For instance, let's choose the asymmetric factorization

$$W = \begin{pmatrix} \sqrt{\cosh(1/T)}, & \sqrt{\sinh(1/T)} \\ \sqrt{\cosh(1/T)}, & -\sqrt{\sinh(1/T)} \end{pmatrix}.$$

The absent legs in the tensors P and Q are graphically indicated by the carets "∧" and "<", this notation becomes clear from the coarse-graining procedure explained in this Section.

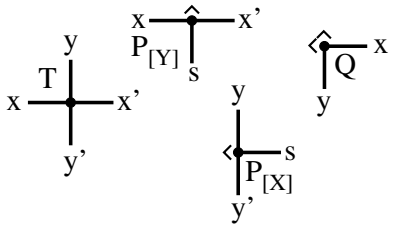

Figure 5.3: Four types of local tensors. A tensor network state can be decomposed into the local tensors T, P ($P_{[\mathrm{Y}]}$ and $P_{[\mathrm{X}]}$), and Q. The missing legs are indicated by the carets "∧" and "<".

In order to calculate the partition function, we adapted the coarse-graining renormalization procedure from [Xie et al., 2012], which is explained in Section 2.3. However, the construction of the fractal lattice is slightly more intricate, so we explain our adapted procedure in more depth in the following.

At each iterative step n, the new tensors $T^{(n+1)}$, $P^{(n+1)}$, and $Q^{(n+1)}$ are created from the preceding tensors $T^{(n)}$, $P^{(n)}$, and $Q^{(n)}$ (see Fig. 5.4). Practically, this is achieved in several steps. Firstly, two tensors $T^{(n)}$ are contracted and renormalized along the y axis. Subsequently, the resulted tensor is contracted and renormalized along the x axis. At this stage, the central tensor $S^{(n)}$ and the unitary matrices $U^{(n)}_{[\mathrm{Y}]}$ and $U^{(n)}_{[\mathrm{X}]}$ have been created. The unitary matrices $U^{(n)}_{[\mathrm{Y}]}$ and $U^{(n)}_{[\mathrm{X}]}$ are calculated in the process of HOSVD of the tensors contracted along the y axis and x

[1] See the explanation of the tensor-network representation in Subsection 2.3.1.

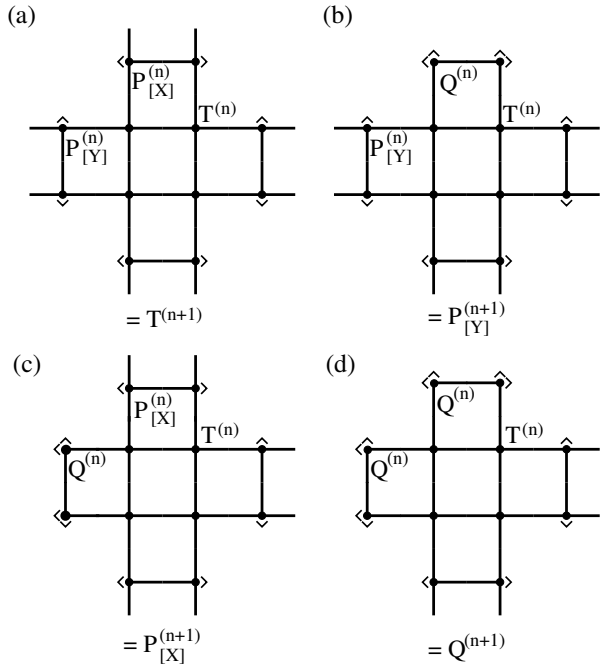

Figure 5.4: Composition of new tensors: (a) A new tensor $T^{(n+1)}$ is created from four tensors $T^{(n)}$, four tensors $P^{(n)}_{[\mathrm{Y}]}$, and four tensors $P^{(n)}_{[\mathrm{X}]}$. (b) A new tensor $P^{(n+1)}_{[\mathrm{Y}]}$ is created from four tensors $T^{(n)}$, four tensors $P^{(n)}_{[\mathrm{Y}]}$, two $P^{(n)}_{[\mathrm{X}]}$, and two $Q^{(n)}$. (c) A new tensor $P^{(n+1)}_{[\mathrm{X}]}$ is created from four $T^{(n)}$, two $Q^{(n)}$, two $P^{(n)}_{[\mathrm{Y}]}$, and four $P^{(n)}_{[\mathrm{X}]}$. (d) A new tensor $Q^{(n+1)}$ is created from four $T^{(n)}$, four $Q^{(n)}$, two $P^{(n)}_{[\mathrm{Y}]}$, and two $P^{(n)}_{[\mathrm{X}]}$.

axis, respectively. Notice that the central tensor $S^{(n)}$ is composed of four tensors $T^{(n)}$ and can be found in the centre of the new tensors $T^{(n+1)}$, $P^{(n+1)}$, and $Q^{(n+1)}$. Depending on what type of tensor is constructed, different legs ($L_{[\mathrm{Y}]}$ or $L_{[\mathrm{X}]}$) or carets ($C_{[\mathrm{Y}]}$ or ($C_{[\mathrm{X}]}$) are attached to the central tensor (see Fig. 5.8). By repeating this procedure, one can construct a lattice structure as large as required (e.g. the next iterative step yields to a tensor $T^{(n+2)}$ as depicted in Fig. 5.5).

Central tensor construction The central tensor $S^{(n)}$ is constructed in two steps: contraction and renormalization along the y axis followed by the same procedure along the x axis on the resulted tensor (see Fig. 5.6).

First, by contraction of two tensors $T^{(n)}$ along the y axis, we define

$$M^{(n)}_{[\mathrm{Y}]xx'yy'} = \sum_i T^{(n)}_{x_1 x'_1 y i} T^{(n)}_{x_2 x'_2 i y}, \tag{5.7}$$

where $x = x_1 \otimes x_2$ and $x' = x'_1 \otimes x'_2$. To truncate the tensor $M^{(n)}_{[\mathrm{Y}]}$ by HOSVD, two

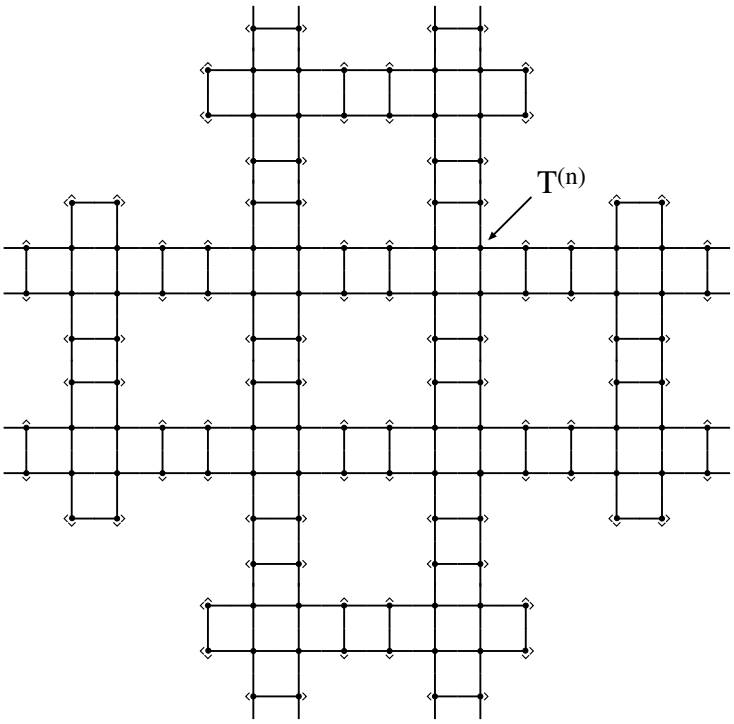

Figure 5.5: Structure of a tensor $T^{(n+2)}$. For clarity, one tensor $T^{(n)}$ is denoted in the picture.

matrix unfoldings are prepared

$$M_{[\mathrm{Y}](1)x,x'yy'} = M_{[\mathrm{Y}]xx'yy'}\,, \tag{5.8}$$

and

$$M_{[\mathrm{Y}](2)x',yy'x} = M_{[\mathrm{Y}]xx'yy'}\,. \tag{5.9}$$

Then, a SVD for these two matrices is performed

$$M_{[\mathrm{Y}](1)} = U_{[\mathrm{Y}](1)}\Sigma_{[\mathrm{Y}](1)}V^{\dagger}_{[\mathrm{Y}](1)}\,, \tag{5.10}$$

$$M_{[\mathrm{Y}](2)} = U_{[\mathrm{Y}](2)}\Sigma_{[\mathrm{Y}](2)}V^{\dagger}_{[\mathrm{Y}](2)}\,, \tag{5.11}$$

where $U_{[\mathrm{Y}](1)}$, $V_{[\mathrm{Y}](1)}$, $U_{[\mathrm{Y}](2)}$, and $V_{[\mathrm{Y}](2)}$ are unitary matrices of respective index dimensions, and $\Sigma_{[\mathrm{Y}](1)}$ and $\Sigma_{[\mathrm{Y}](2)}$ are matrices with singular values as its diagonal entries

$$\Sigma_{[\mathrm{Y}](.)} = \mathrm{diag}(\sigma_{(.)1}, \sigma_{(.)2}, \dots)\,. \tag{5.12}$$

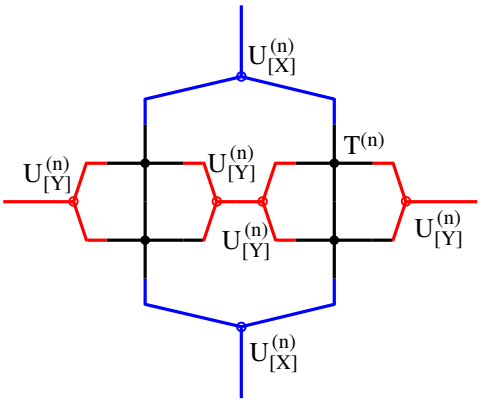

Figure 5.6: Structure of a central tensor $S^{(n)}$. Tensors are contracted and renormalized along the y axis by the unitary matrix $U^{(n)}_{[\mathrm{Y}]}$ (red colour), and along the x axis by $U^{(n)}_{[\mathrm{X}]}$ (blue colour).

The singular values are ordered in decreasing order by convention. To obtain the best approximation of the tensor $M^{(n)}_{[\mathrm{Y}]}$, the two errors

$$\varepsilon_1 = \sum_{i>D} \sigma^2_{(1)i} \tag{5.13}$$

and

$$\varepsilon_2 = \sum_{i>D} \sigma^2_{(2)i} \tag{5.14}$$

are calculated and compared. If $\varepsilon_1 < \varepsilon_2$, we truncate the second index dimension of $U_{[\mathrm{Y}](1)}$ down to D and set $U_{[\mathrm{Y}]} = U_{[\mathrm{Y}](1)}$. Otherwise, the second index dimension of $U_{[\mathrm{Y}](2)}$ is truncated and $U_{[\mathrm{Y}]} = U_{[\mathrm{Y}](2)}$.

After the truncation, we can create a new tensor

$$T^{(n)}_{[\mathrm{Y}]xx'yy'} = \sum_{ij} U^{(n)}_{[\mathrm{Y}]ix} M^{(n)}_{[\mathrm{Y}]ijyy'} U^{(n)}_{[\mathrm{Y}]jx'} \,. \tag{5.15}$$

The contraction and the renormalization along the x axis is performed identically. By the contraction of two tensors $T^{(n)}_{[\mathrm{Y}]}$ along the x axis, we define

$$M^{(n)}_{[\mathrm{X}]xx'yy'} = \sum_{i} T^{(n)}_{[\mathrm{Y}]xiy_1y'_1} T^{(n)}_{[\mathrm{Y}]ix'y_2y'_2} \,, \tag{5.16}$$

where $y = y_1 \otimes y_2$ and $y' = y'_1 \otimes y'_2$. Analogously, the matrix unfoldings are prepared

$$M_{[\mathrm{X}](3)y,y'xx'} = M_{[\mathrm{X}]xx'yy'} \,, \tag{5.17}$$

$$M_{[\mathrm{X}](4)y',xx'y} = M_{[\mathrm{X}]xx'yy'}\,, \tag{5.18}$$

on which SVD is performed again. As before, the errors ε_3 and ε_4 are compared and the chosen unitary matrix (associated with the smaller error ε) is truncated and set to $U_{[\mathrm{X}]}$. Finally, we can define the central tensor as

$$S^{(n)}_{xx'yy'} = \sum_{kl} U^{(n)}_{[\mathrm{X}]ky} M^{(n)}_{[\mathrm{X}]xx'kl} U^{(n)}_{[\mathrm{X}]ly'}\,. \tag{5.19}$$

Legs and carets construction The legs and the carets are auxiliary objects used in updating the local tensors. These objects are composed of the tensors P or Q contracted with the unitary matrices $U_{[\mathrm{Y}]}$ or $U_{[\mathrm{X}]}$ (see Fig. 5.7).

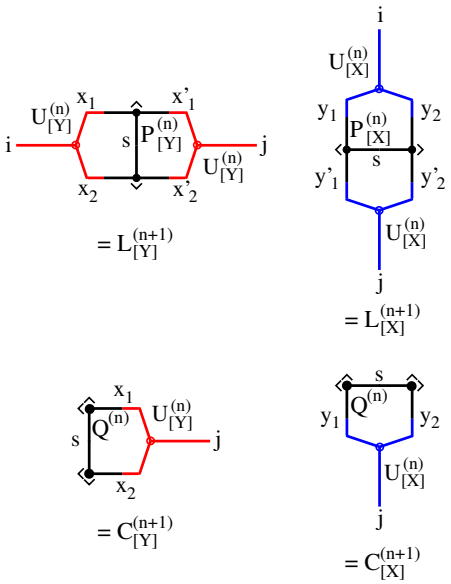

Figure 5.7: Composition of the legs and the carets (auxiliary objects).

Let us begin with the preparation of the leg $L^{(n)}_{[\mathrm{Y}]}$

$$L^{(n)}_{[\mathrm{Y}]ij} = \sum_{sx_1x_2x'_1x'_2} U^{(n)}_{[\mathrm{Y}]x_1\otimes x_2 i} P^{(n)}_{[\mathrm{Y}]x_1x'_1s} P^{(n)}_{[\mathrm{Y}]x'_2x_2s} U^{(n)}_{[\mathrm{Y}]x'_1\otimes x'_2 j}\,. \tag{5.20}$$

Note that the $P_{[\mathrm{Y}]}$ tensors are symmetric, i. e., $P^{(n)}_{[\mathrm{Y}]xx's} = P^{(n)}_{[\mathrm{Y}]x'xs}$. Hence, in this way, the calculation does not depend on the order of the first two indices of $P_{[\mathrm{Y}]}$ (similar remark holds for $P_{[\mathrm{X}]}$).

The $L^{(n)}_{[\mathrm{X}]}$ leg is constructed as

$$L^{(n)}_{[\mathrm{X}]ij} = \sum_{sy_1y_2y'_1y'_2} U^{(n)}_{[\mathrm{X}]y_1\otimes y_2 i} P^{(n)}_{[\mathrm{X}]y_1y'_1 s} P^{(n)}_{[\mathrm{X}]y'_2y_2 s} U^{(n)}_{[\mathrm{X}]y'_1\otimes y'_2 j}. \tag{5.21}$$

Let us now proceed with the creation of the carets. The carets $C^{(n)}_{[\mathrm{Y}]}$ and $C^{(n)}_{[\mathrm{X}]}$ are defined as

$$C^{(n)}_{[\mathrm{Y}]j} = \sum_{sx_1x_2} Q^{(n)}_{x_1 s} Q^{(n)}_{x_2 s} U^{(n)}_{[\mathrm{Y}]x_1\otimes x_2 j}, \tag{5.22}$$

$$C^{(n)}_{[\mathrm{X}]j} = \sum_{sy_1y_2} Q^{(n)}_{sy_1} Q^{(n)}_{sy_2} U^{(n)}_{[\mathrm{X}]y_1\otimes y_2 j}, \tag{5.23}$$

respectively. Note that carets are just vectors (they have only single index j).

Update of local tensors With all auxiliary objects prepared (central tensor, legs and carets), we are ready to create the new tensors $T^{(n+1)}$, $P^{(n+1)}_{[\mathrm{Y}]}$, $P^{(n+1)}_{[\mathrm{X}]}$, $Q^{(n+1)}$ for the next iteration step $n+1$. The local tensors are updated as follows (see Fig. 5.8):

- creation of $T^{(n+1)}$

$$T^{(n+1)}_{xx'yy'} = \sum_{abcd} S^{(n)}_{abcd} L^{(n)}_{[\mathrm{Y}]xa} L^{(n)}_{[\mathrm{Y}]bx'} L^{(n)}_{[\mathrm{X}]yc} L^{(n)}_{[\mathrm{X}]dy'} \tag{5.24}$$

- creation of $P^{(n+1)}_{[\mathrm{Y}]}$

$$P^{(n+1)}_{[\mathrm{Y}]xx's} = \sum_{abcd} S^{(n)}_{abcd} L^{(n)}_{[\mathrm{Y}]xa} L^{(n)}_{[\mathrm{Y}]bx'} C^{(n)}_{[\mathrm{X}]c} L^{(n)}_{[\mathrm{X}]ds} \tag{5.25}$$

- creation of $P^{(n+1)}_{[\mathrm{X}]}$

$$P^{(n+1)}_{[\mathrm{X}]yy's} = \sum_{abcd} S^{(n)}_{abcd} C^{(n)}_{[\mathrm{Y}]a} L^{(n)}_{[\mathrm{Y}]bs} L^{(n)}_{[\mathrm{X}]yc} L^{(n)}_{[\mathrm{X}]dy'} \tag{5.26}$$

- creation of $Q^{(n+1)}$

$$Q^{(n+1)}_{xy} = \sum_{abcd} S^{(n)}_{abcd} C^{(n)}_{[\mathrm{Y}]a} L^{(n)}_{[\mathrm{Y}]bx} C^{(n)}_{[\mathrm{X}]c} L^{(n)}_{[\mathrm{X}]dy}. \tag{5.27}$$

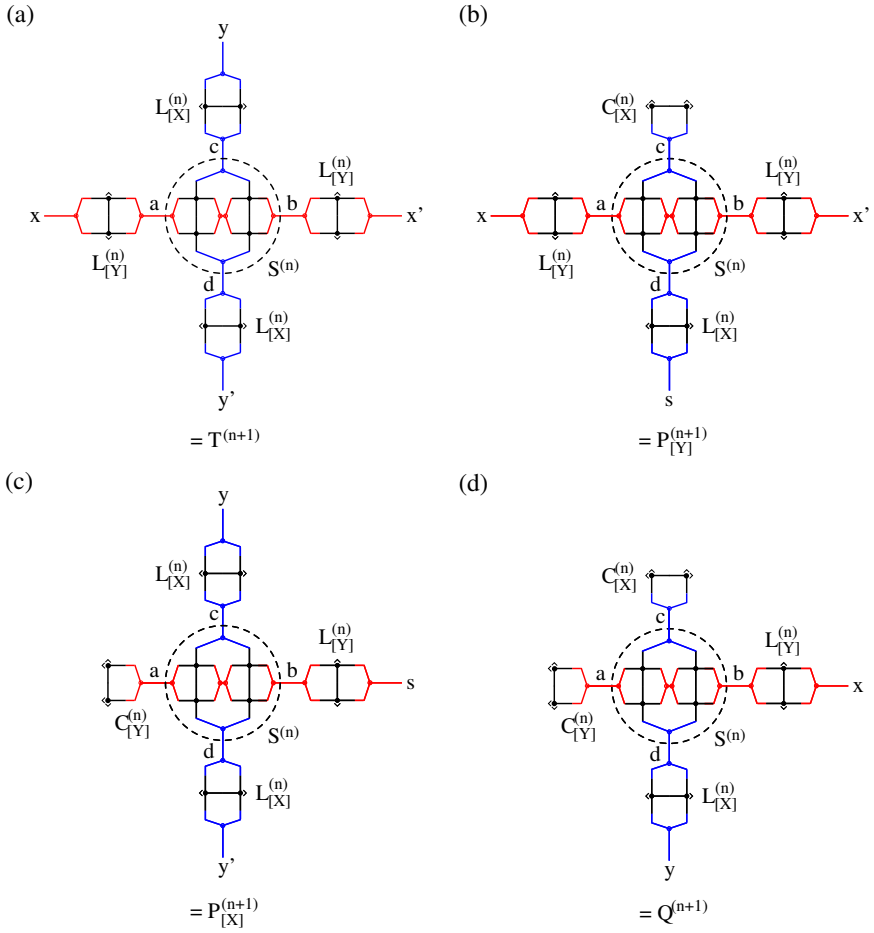

Figure 5.8: Update of local tensors.

5.3 Numerical Results

Throughout the numerical analysis, we use dimensionless units by setting $J = k_{\mathrm{B}} = 1$, and thus we have $K = 1/T$. In the numerical calculation by means of HOTRG, we keep $D = 24$ states at most for the auxiliary variables. We have verified that the choice $D = 24$ is sufficient for obtaining the converged free energy normalized per spin site

$$F_n(T) = -\frac{k_{\mathrm{B}}T}{N_n} \ln \mathcal{Z}_n(T)$$

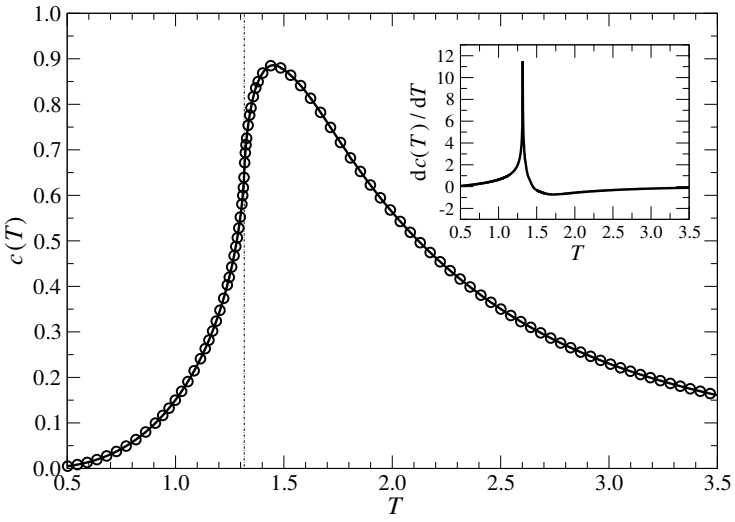

Figure 5.9: The specific heat $c(T)$ per site. Inset: numerical derivative of $c(T)$ with respect to temperature; a sharp peak is observed at $T_c \approx 1.317$.

in the entire temperature region [2]. We treat the free energy per site in the thermodynamic limit

$$f(T) = \lim_{n\to\infty} F_n(T),$$

where the r.h.s. converges completely already for $n \lesssim 30$.

Figure 5.9 shows the temperature dependence of the specific heat per site

$$c(T) = \frac{\partial}{\partial T} u(T),$$

where $u(T)$ is the internal energy per site

$$u(T) = -T^2 \frac{\partial}{\partial T} \frac{f(T)}{T}.$$

The temperature derivatives are performed numerically. Surprisingly, there is no singularity in $c(T)$ around its maximum located at $T \approx 1.45$. One might find a weak non-analytic behavior at $T_c \approx 1.317$, which is marked by the dotted line in the figure; the numerical derivative of $c(T)$ with respect to temperature (plotted in the inset) has a sharp peak at the correct critical temperature T_c. It is, however, difficult to determine the critical exponent α from the scaling $c(T) \propto |T - T_c|^{-\alpha}$, because of the weakness in the singularity; as shown in the figure, $c(T)$ around T_c is almost linear in T, and therefore α is nearly zero.

[2] Larger values of D are necessary if small density-matrix eigenvalues are required for the purpose of accurate analyzing their asymptotic decay.

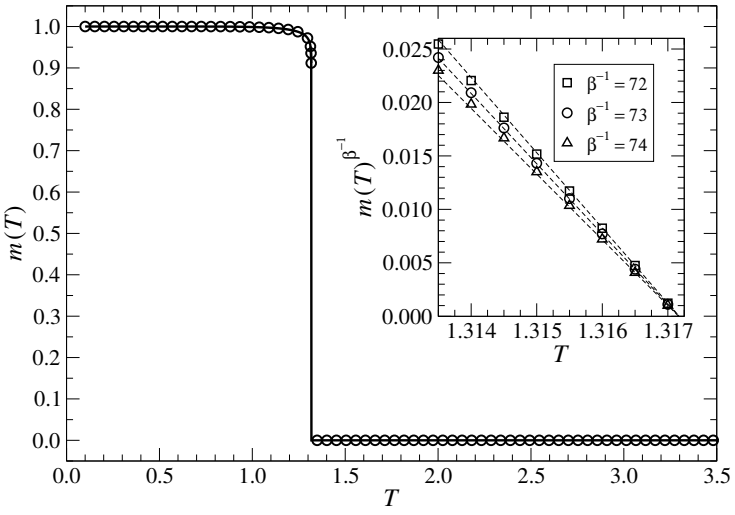

Figure 5.10: The spontaneous magnetization per site $m(T)$. Inset: the power-law behavior below $T_c = 1.31716$.

Figure 5.10 shows the spontaneous magnetization per site $m(T)$, which is obtained by inserting a σ-dependent local tensor into the system like in Eq. (2.85). Since the fractal lattice is inhomogeneous, the value is weakly dependent on the location of the observation site, but the critical behavior is not affected by the location; we choose a site from the four sites that are in the middle of the 12-site cluster shown in Fig. 5.2. The numerical calculation by HOTRG captures the spontaneous magnetization $m(T)$ below T_c since any tiny round-off error is sufficient for breaking the symmetry inside the low-temperature ordered state. Around the transition temperature, the magnetization satisfies a power-law behavior (see Eq. (1.18))

$$m(T) \propto |T_c - T|^{0.0137}, \tag{5.28}$$

where the precision of the exponent is around 2%, which can be read out from the inset of Fig. 5.10 as the most linear behavior out of a tiny deviation from the linear dependence (the dashed lines) in $m(T)^{1/\beta}$ near T_c.

As a byproduct of the numerical HOTRG calculation, we can roughly observe the entanglement spectrum [3], which is the distribution of the eigenvalue ω_i of the density matrix that is created for the purpose of obtaining the renormalization transformation. Since the effect of *environment* is not considered in our implemen-

[3]It is possible to identify the system boundary of a finite area of two-dimensional classical lattice models as "a wave function" of a certain one-dimensional quantum system. In this manner, one naturally finds the quantum-classical correspondence, and can introduce the notion of entanglement in classical lattice models.

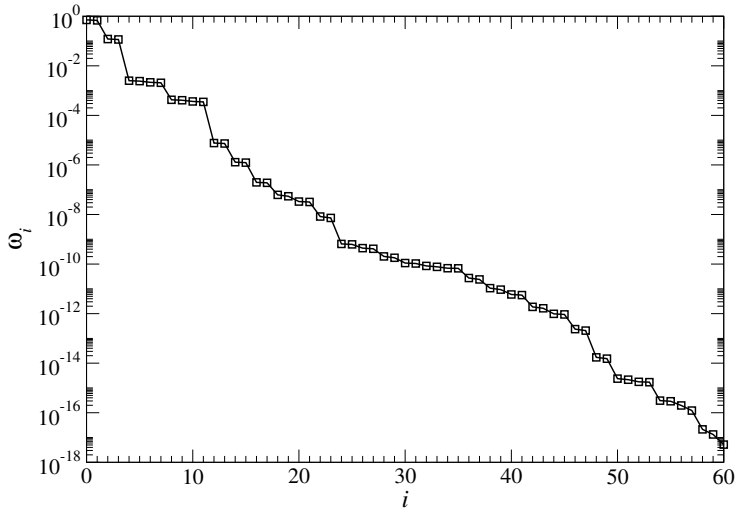

Figure 5.11: Decay of the singular values after $n = 8$ extensions.

tation of the HOTRG method, the eigenvalue $\omega_i = \lambda_i^2$ is obtained as the square of the singular values λ_i in the higher-order singular value decomposition applied to the extended tensors. Figure 5.11 shows ω_i at $T = T_c$ in the decreasing order. The decay is rapid, and therefore further increase of the number of block-spin state from $D = 24$ to a larger number does not significantly improve the precision in the partition function $\mathcal{Z}_n$; the difference in $f(T_c)$ between $D = 8$ and $D = 16$ is already of the order of 10^{-6}. It should be noted that the eigenvalues are not distributed equidistantly in logarithmic scale; the corner double line structure is absent [Gu and Wen, 2009, Ueda et al., 2014].

5.4 Outlook

This Section proposes several possible paths of our future work. Our preliminary data, which are to be further improved, extended, and later published, are presented in the following.

Hyperscaling hypothesis for fractals A first interesting task is to verify the validity of the scaling relations Eq. (1.25)–Eq. (1.29) numerically in the case of the fractional dimension. For this purpose, we obtained $\delta \approx 206$ by analysis of the field response in the fractal-lattice Ising model (for $D = 12$) [4], see Fig. 5.12.

[4] For $D = 16$ (data not presented here), we have obtained $\delta \approx 205$, which is a good verification of the achieved accuracy.

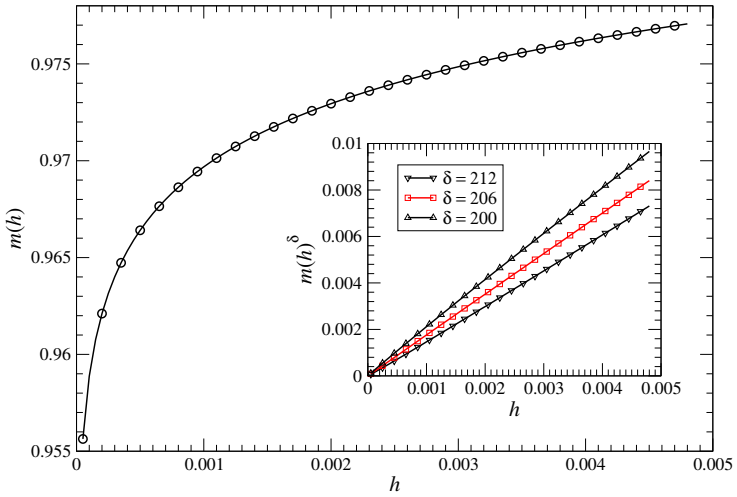

Figure 5.12: The magnetic field response of the spontaneous magnetization at the temperature $T = T_c$ for the fractal-lattice Ising model studied earlier in this Chapter (for $D = 12$).

Using the previously obtained exponents $\alpha = 0$ and $\beta = 1/73$ and the dimension of the lattice $d = 3/2$, we can derive from the scaling relations Eq. (1.25)-Eq. (1.29) following output

$$\gamma = 144/73\,, \tag{5.29}$$

$$\delta = 145\,, \tag{5.30}$$

$$\nu = 4/3\,. \tag{5.31}$$

Or, alternatively, by taking the dimension $d = d^{(\mathrm{H})} = 1.792$ we have $\nu = 1.116$.

Note that our numerical analysis yielded $\delta \approx 206$, not $\delta = 145$ as implied from the scaling hypothesis. This discrepancy will be analyzed and explained in our future study. One possible explanation is that the scaling hypothesis cannot be applied to fractal lattices. Another possibility is that the HOTRG is not yet accurate enough to be used for the determination of the exponent δ. Notice that the calculation of δ (via the scaling relation) has nothing to do with the lattice dimension d.

Another question of high interest is to estimate the exponent ν numerically, which apperars in the hyperscaling relation Eq. (1.29). It is not clear if the exponent ν is well-defined in the case of the fractal-lattice Ising model as we have observed exponentially decaying spectrum of the singular values at the phase transition temperature; it means there is no power-law decay as it is characteristic at

the phase transitions on Euclidean lattices. The power-law decay is connected to the algebraical decay of the correlation function, out of which one can calculate the critical exponent ν. Since we have observed the exponential decay of the singular values with respect to tensor entanglement, the associated exponential decay of the correlation function at T_c is expected, which cannot be used to obtain ν (as for mean-field models). However, we keep in mind that these are all very preliminary conjectures and we are still at the beginning of the study on the fractal geometries.

Legs extension It is also in our interest to generalize the original fractal lattice in a way to be able to tune the lattice dimension. We propose an infinite series of fractal lattices, whose fractal dimensions $\{d_L\}_{i=0}^{\infty}$, $d_0 \equiv 2 > d_1 > d_2 > \ldots d_\infty \equiv 1$, converge to the one-dimensional lattice monotonously. A simple way to decrease the dimension is by extension of the legs, see Fig. 5.13. The resulted extended legs (and carets) are connected to the central tensor ("body") in the same way as explained in the update of local tensors in the case of the original fractal lattice, cf. Fig. 5.8.

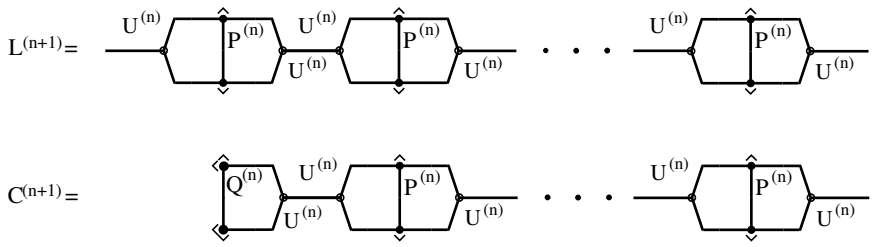

Figure 5.13: Composition of the legs $L^{(n)}$ and the carets $C^{(n)}$. The leg is just L times the leg of the original fractal as depicted in upper half of Fig. 5.7. The carret is composed of the original carret (lower half of Fig. 5.7) attached to the $L-1$ copies of the original leg.

For the better understanding, the lattice extension process in the case of $L = 2$ is graphically represented in Fig. 5.14. The number of sites grows as $(4+8L)^n$ with the iteration step n. One can easily find out that the Hausdorff dimension $d_L^{(H)}$ depends on L as

$$d_L^{(H)} = \frac{\log(4+8L)}{\log(2+2L)}, \qquad L = 0,1,2,\ldots,\infty, \tag{5.32}$$

whereas the other dimension d_L is

$$d_L = 1 + \frac{\log(2)}{\log(2+2L)}. \tag{5.33}$$

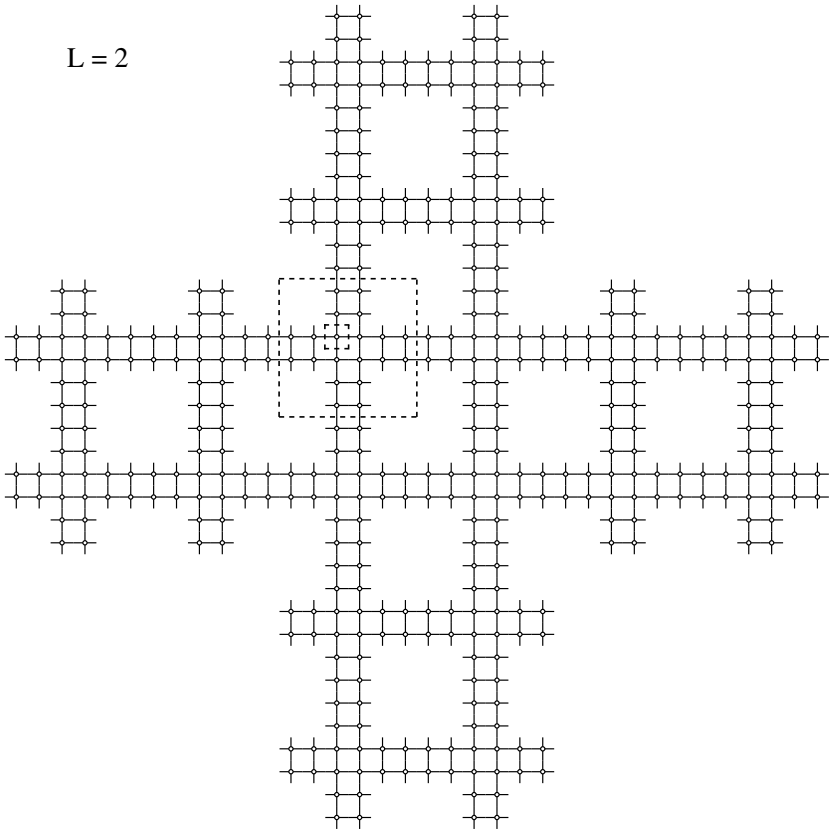

Figure 5.14: Composition of the fractal lattice in the case of $L = 2$. The smallest dashed square: a local tensor with the single spin site in the zeroth iteration step $n = 0$. The bigger dashed square: basic cluster with 20 spin sites in the first iteration step $n = 1$. The entire picture: extended cluster in the second iteration step $n = 2$. The number of sites is 20^n in the n^{th} iteration step.

Therefore, such defined infinite series of fractal lattices allows us to study the thermodynamic properties of the spin models with respect to its (fractional) dimension. So far, we have calculated the free energy and the spontaneous magnetization for different values of L, as shown in Figs. 5.15 and 5.16. It is immediately evident from the Fig. 5.16 that the expected critical temperature decreases as L increases. Note that according the Eq. (5.32) and Eq. (5.33), both dimensions $d_L^{(H)}$ and d_L converge to 1 as L goes to infinity (i.e. $\lim_{L\to\infty} d_L^{(H)} = \lim_{L\to\infty} d_L = 1$). Further details and rigorous results will be published elsewhere.

Body extension: 6 by 6 fractal Next step in generalization of the fractal lattice is to increase the size of the fractal "body". This approach is meant to propose

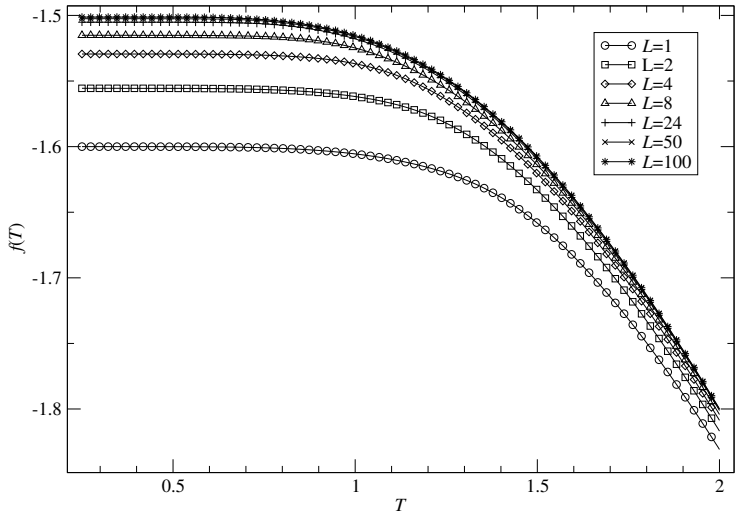

Figure 5.15: The free energy for the fractal-lattice Ising model for different values of the length of the legs L.

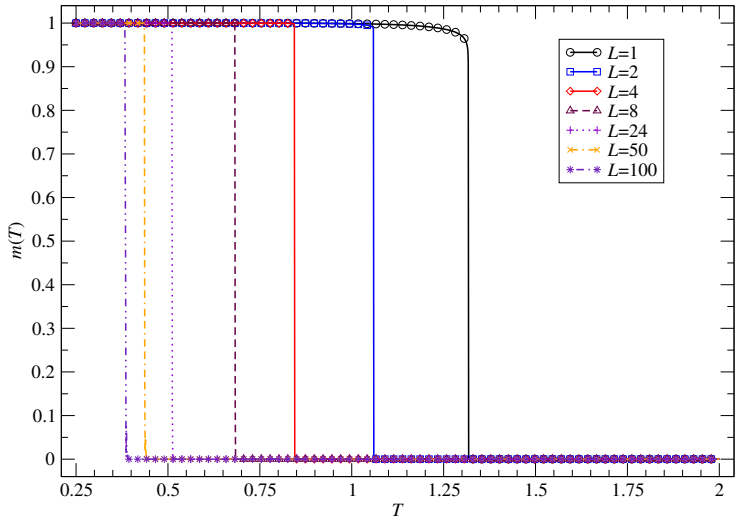

Figure 5.16: The magnetization for the fractal-lattice Ising model for different values of the lengths of legs L.

a complementary infinite series of fractal lattices of fractal dimensions $\{d_K\}_{K=1}^{\infty}$ such that $d_1 < d_2 < \ldots d_\infty \equiv 2$. In other words, the fractal dimensions d_K converge monotonously to the two-dimensional square lattice. Let us return to the original fractal lattice and recall that it is composed of 4 by 4 spin blocks with the four corners removed. By repeating the coarse graining procedure in the process of

creation of the central part, it is possible to construct the generalized series of the fractal lattices of the size (2^K+2) by (2^K+2), where 2^K is the linear dimension of the square-shaped body part of the lattice (i.e., without the legs). For instance, if $K = 1$, we reproduce the original fractal lattice and for $K = 2$ we define the following 6 by 6 lattice (see Fig. 5.17), with the four missing corner spin sites.

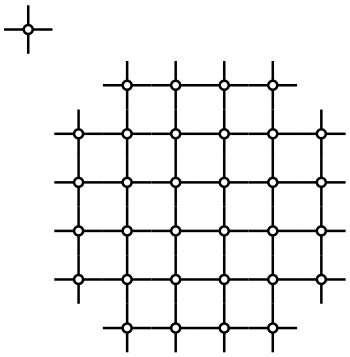

Figure 5.17: The 6×6 fractal lattice.

This generalization leads to the following dimensions

$$d_K^{(H)} = \frac{\log\left[\left(2^K+2\right)^2-4\right]}{\log\left(2^K+2\right)}, \qquad d_K = 1+\frac{\log\left(2^K\right)}{\log\left(2^K+2\right)}. \tag{5.34}$$

Thus, for the 6 by 6 fractal lattice we get $d_{K=2}^{(\mathrm{H})} \approx 1.934$ and $d_{K=2} \approx 1.774$. We estimated the critical temperature from the magnetization in this case to be $T \approx 1.96376$ and the critical exponent $\beta \approx 0.0658652 \approx 1/15$ (for $D = 16$), see Fig. 5.18. However, the accuracy in determining the critical temperature as well as in the critical exponent β can be further improved by taking larger values of D. We have observed a sharp peak in the specific heat at $T_c \approx 1.96376$, see Fig. 5.19.

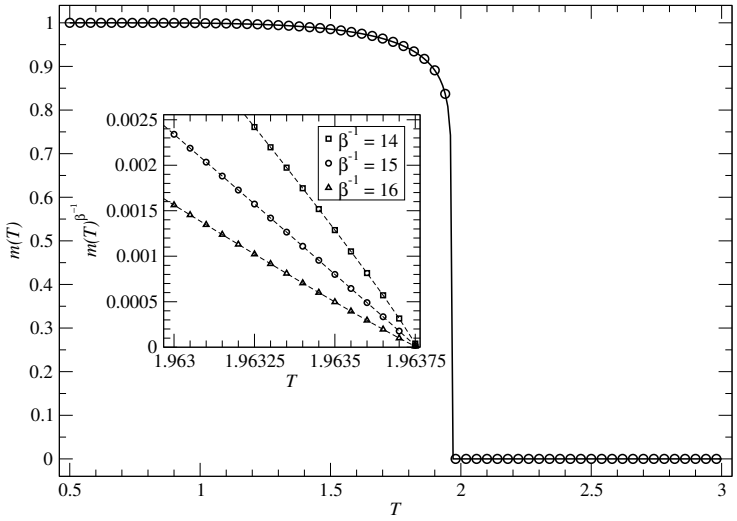

Figure 5.18: The spontaneous magnetization $m(T)$ for the 6 by 6 fractal lattice (for $D = 16$). Inset: the linear behavior of $[m(T)]^{1/\beta}$ below $T_c \approx 1.96376$.

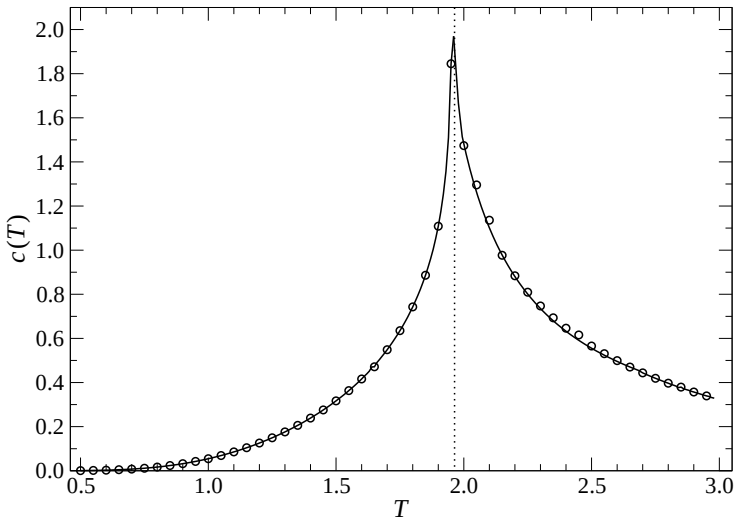

Figure 5.19: The specific heat $c(T)$. The sharp singularity at $T_c \approx 1.96376$ corresponds to the second order phase transition of the Ising model on the fractal lattice with $K = 2$ (for $D = 16$).

Conclusions and outlook

The main research focus of this work was to explore the phase transitions of various spin systems on the non-Euclidean lattice geometries. This was not a trivial task, due to its high complexity, which required considering non-standard mathematical approaches as well as non-straightforward generalizations of the tensor product state ansatz. For this purpose, we have chosen the two methods, CTMRG and HOTRG, which were found to be suitable for treating the critical phenomena of the multistate spin systems on the hyperbolic and fractal lattices, respectively.

We have been motivated by the two tensor-network-based algorithms in order to extend their applicability to the multistate spin system on the non-Euclidean geometries, which are exclusively specified by the topological structure of the spin interaction of a Hamiltonian. Such missing results have been demanding, as they are considered to be the key for understanding various complex systems, such as neural networks, social behavior analysis, as well as the general theory of relativity, where the Euclidean geometry cannot reproduce the real systems. Let us make another remark that none of these tasks has been known to be exactly solvable. Additionally, the standard numerical methods, such as Monte Carlo simulations, exact diagonalization, Density Matrix Renormalization Group, etc., are also not applicable at all.

The concluding remarks of our research are grouped into the three work-packages (and discussed separately in the following order):

(1) The unique free-energy analysis of the multistate spin systems on an infinite set of hyperbolic geometries with respect to the radius of Gaussian curvature;

(2) The application of the CTMRG method on a multistate model of social behavior, which originates in the statistical physics;

(3) The development of the algorithm (based on HOTRG), which can be used to classify the phase transitions on fractal geometries.

(1) We have analyzed the free energy per site of the multistate models with respect to the underlying lattice geometries ($p \geq 4, q \geq 4$). For this purpose, we derived an analytic expression for the free energy per site. It is a set of recurrence relations, which are required when calculating the free energy by the generalized CTMRG algorithm for the regular non-Euclidean geometries. The derived free energy per site applies to any spin model, and we studied the M-state clock and Potts models for $M \geq 2$. The numerical results yielded high numerical accuracy with respect to the exact solutions of the Ising models on the square and Bethe lattices at phase transition. Minimizing the free energy with respect to the underlying geometry (p,q), the minimal bulk free energy per site resulted in any multistate spin model on the Euclidean square lattice for an arbitrary temperature.

The free energy contains complete information and incorporates the boundary structure of the complex hyperbolic geometry. This is the essential feature when describing the AdS space. There is a relation between solid-state physics and the general theory of relativity if classifying the regular AdS spaces. In particular, this relation lies in a direct calculation of the entanglement entropy by CTMRG of a subsystem $\mathcal{A}$ in the quantum Heisenberg model on $(4, q \geq 4)$ lattice geometries. We intend to prove a concept of the so-called holographic entanglement entropy [Ryu and Takayanagi, 2006]. It states that a non-gravitational theory can live on the subsystem boundary $\partial\mathcal{A}$ of $(d+1)$-dimensional hyperbolic spaces. Hence, the entanglement entropy $S_{\mathcal{A}}$, which is associated with a reduced density matrix of the subsystem $\mathcal{A}$, provides the correct measure of the information contained in the AdS-CFT correspondence. The entanglement entropy $S_{\mathcal{A}}$ is related to a surface region $\partial\mathcal{A}$ (also known as the minimal area surface) in the AdS space. Moreover, the entanglement entropy $S_{\mathcal{A}}$ is proportional to the corresponding d-dimensional region $\mathcal{A}$ defined in CFT. Our aim is to obtain the von Neumann entanglement entropy of the quantum spin systems with respect to the underlying AdS lattice geometry.

Our results have revealed a surprising feature: there exists an inherited physical similarity between the ground-state energy of microscopic multispin models and the Gaussian curvature. Such an achievement certainly deserves a better understanding supported by theoretical reasoning in the future. Our current numerical findings cannot unambiguously justify the incomplete conjectures of this work. In the future, we plan to broaden our results to explain how the intrinsic structure of the space lattice geometry (being mapped onto the microscopic spin-interaction networks) may affect the lowest energy of the system. Let us note that the energy inherits information about the geometry of the entire system. We, therefore, conjecture that the free energy analysis of the multistate systems intrinsically contains the underlying regular hyperbolic structure being proportional to the radius of curvature. We prepare a paper on the complete set of lattices ($p \geq 3, q \geq 3$), where all regular spherical and Euclidean geometries are taken into account.

(2) Having been motivated by the Axelrod model known for its applicability to mimic social behavior, we have proposed a multistate thermodynamic spin model. Our model was defined on the two-dimensional $(4,4)$ lattice in the thermodynamic limit (whereas the original Axelrod model was considered on a square-shaped lattice of a rather limited size.) The thermodynamic model was analyzed numerically with the aim to obtain equilibrial properties over our social model. We have focused on the phase transition analysis.

We have considered a simplified case restricted to two ($f = 2$) cultural features only, where each feature can assume q different cultural traits ($2 \leq q \leq 6$). Such constraints of our model have significantly affected the thermodynamic properties resulting in the q-dependent phase transition point being associated with the critical noise. The value of the critical noise was found to decrease with the increasing number of traits per feature q. We have thus proposed a thermodynamic analog of the Axelrod model in two dimensions, in which we do not consider the Potts-like interactions only, but we allowed a higher variability by incorporating the clock-like interactions leading to a substantially richer communication structure (which has an analog with the multistate spin interactions). Such a multispin model could be again mapped onto mutually communicating individuals subject to external noise. The noise prevents the mutual communication among the individuals. If the noise increases gradually, the formation of larger clusters of the individuals is suppressed because they do not share the same cultural features (e.g. interests) any longer. The size of the clusters was quantified by the order parameter in our model. If the noise increases, the correlations are suppressed at longer distances. The noise has the analogous character as the thermal fluctuations have in the multistate spin model.

We have identified two phase transitions in our social system for $q = 2$. The language of the social systems can be used to interpret our results in the following example: let the first feature to represent *leisure-time interests* taking two values: 'reading books' and 'listening to music', and let the second feature to represent *working duties* with the two values: 'manual activity' and 'intellectual activity'. Both of the phase transitions are continuous separating three phases, which are classified into (i) the low-noise regime, (ii) the medium-noise regime, and (iii) the high-noise regime.

(i) In the low-noise regime, the individuals tend to form a single dominant cluster, where the associated complete order parameter can possess four values (restricted to three only in the limit of zero noise), see Fig. 4.11. The statistical probability of forming the dominant clusters is proportional to the evaluation of the complete order parameter $\langle O \rangle$. By increasing the noise towards the phase transition between the low- and the medium-noise regimes, the complete order parameter does not drop to zero. Instead, it

becomes $\langle O \rangle = \frac{1}{2}$.

(ii) Within the medium-noise regime, a new topological phase reveals, so that two equally likely traits of the individuals are formed. In the social terms, the pairing of the cultural settings coincides with two cases. The first: (1a) the equal mixture of those individuals who 'read books' and 'do manual activity' and (1b) the individuals who 'listen to music' and 'do intellectual activity'. The second: (2a) the equal mixture of those who 'listen to music' and 'do manual activity' and (2b) those who 'read books' and 'do intellectual activity'.

(iii) In the high-noise regime, the clusters of common interests become less relevant, i.e., the correlation between the individuals weakens with the increasing noise. As the consequence, the individuals behave in a completely uncorrelated way.

The further results, associated with the only discontinuous phase transition between the low- and high-noise regime, are present if the trait number is larger than two, i.e., for $q > 2$. Larger clusters of individuals possessing q^2 cultural setting are formed inside the low-noise regime. Again, the order parameter $\langle O \rangle$ measures the proportionality with the selected cultural setting of the dominant cluster sizes. Therefore, this region corresponds to the ordered multistate spin phase right below the phase transition noise $T_t(q)$. The high-noise regime characterizes the uncorrelated individuals (the disordered phase) above the phase transition noise. The low-noise regime is separated from the high-noise regime by the discontinuity of the cluster size, in particular, the complete order parameter exhibits the jump in agreement with the phase transition of the first order.

It is worth mentioning that the phase transition noise is found to be nonzero in the asymptotic limit of the trait number $q \to \infty$, in particular, $T_t(\infty) \approx \frac{1}{2}$. We, therefore, conjecture the permanent existence of the correlated clusters of individuals below the nonzero phase transition noise $T_t(\infty)$.

Recently, we have also studied the thermodynamic properties of the extended social influence on the non-Euclidean and fractal communication geometries for any $f \geq 2$ and $q \geq 2$. The properties of the hyperbolic geometries with the infinite dimensionality d resemble the so-called *small-world* effect, which is the basic property of the many real-world networks, including the social systems [Barrat et al., 2008]. At the opposite spectrum, the fractal structure allows us to study the social model in a range of fractional dimensions $1 \leq d \leq 2$, which might provide additional insight into the character of the robustness of our model. We have found interesting features, which will be published soon.

(3) Finally, we have investigated the Ising model on the fractal lattice (as depicted in Fig. 5.2) by means of the HOTRG algorithm. Although there is no evident singularity in the specific heat, our deeper analysis suggests that the model exhibits the second order phase transition. Qualitatively, such an unusual presence of the weak singularity in the specific heat agrees with the result of the ε-expansion, which shows the increasing nature of the critical exponent in the specific heat with respect to the space dimension d [Wilson and Kogut, 1974]. At the same time, the spontaneous magnetization also reveals the features of the second order phase transition, for which we have calculated the critical exponent $\beta_{\text{fractal}} \approx 0.0137$. Notice that the exponent is smaller by one order of magnitude than the Ising model critical exponent $\beta_{\text{square}} = 1/8 = 0.125$ on the square lattice.

The fractal structure of the lattice caused that the spectrum of the entanglement entropy differs from that on the square lattice, as explained by the corner double line picture [Gu and Wen, 2009, Ueda et al., 2014]. The process of the renormalization group transformation results in the absorption of the short-range entanglement; it originates in the missing four corners of the basic tensor cell, which forms the fractal structure of the lattice, cf. Fig. 5.2. For this reason, only a few degrees of freedom suffice for the renormalized tensors. The situation is similar to the entanglement structure, as reported in the tensor renormalization [Evenbly and Vidal, 2015a, Evenbly and Vidal, 2015b, Evenbly, 2015, Evenbly and Vidal, 2016, Hauru et al., 2015, Yang et al., 2015].

One can also create a variety of fractal lattice geometries by an appropriate modification of the basic tensor cell. We considered a few ways of proposing an infinite series of the fractal lattices in Section 5.4.

(i) The first process can be carried out by a gradual extension of the length of the connecting legs. We have thus specified the infinite series of the fractal lattices with the monotonously decreasing dimensions $\{d_L\}_{L=0}^{\infty}$, which converge to the one-dimensional lattice, i.e., $d_0 \equiv 2 > d_1 > d_2 > \ldots d_\infty \equiv 1$;

(ii) Rather than considering the leg extensions, we can also expand the body size of the basic tensor cells. This leads to a different infinite series of the fractal lattices with the fractal dimensions $\{d_K\}_{K=1}^{\infty}$, which satisfy the monotonous increasing sequence of dimensions $d_1 < d_2 < \ldots d_\infty \equiv 2$ converging to the two-dimensional square lattice.

(iii) Furthermore, a combination of the two strategies is also available. Such a process is useful to construct fractal lattices of the desired dimension.

The justification for considering such specific processes rests in the long-lasting open problem of verifying the validity of the scaling hypotheses for the fractional systems. Numerical analyses of quantum spin systems on a variety of

the fractal lattices is another challenging extension [Voigt et al., 2001, Voigt et al., 2004]. These studies will help in clarifying the role of the entanglement in the universality of the phase transition in both the regular and the fractal lattices.

Bibliography

[Anderson, 2005] Anderson, J. W. (2005). *Hyperbolic Geometry*. Springer, 2nd edition.

[Anderson, 2013] Anderson, P. W. (2013). *Physics Today*, 66(4):9.

[Axelrod, 1997] Axelrod, R. (1997). *The Journal of Conflict Resolution*, 42:203.

[Baek et al., 2007] Baek, S. K., Minnhagen, P., and Kim, B. J. (2007). *EPL*, 79:26002.

[Barrat et al., 2008] Barrat, A., Barthélemy, M., and Vespignani, A. (2008). *Dynamical Processes on Complex Networks*. Cambridge University Press.

[Baxter, 1982] Baxter, R. J. (1982). *Exactly Solved Models in Statistical Mechanics*. Academic Press, London.

[Burkhardt and van Leeuwen, 1982] Burkhardt, T. W. and van Leeuwen, J. M. J., editors (1982). *Real-Space Renormalization*, volume 30 of *Topics in Current Physics*. Springer, Berlin. And references therein.

[Cabot et al., 2009] Cabot, A., Alivisatos, A. P., Puntes, V. F., Balcells, L., Iglesias, O., and Labarta, A. (2009). *Phys. Rev. B*, 79:094419.

[Carmona et al., 1998] Carmona, J. M., Marini, U., Marconi, B., Ruiz-Lorenzo, J. J., and Tarancon, A. (1998). *Phys. Rev. B*, 58:14387.

[Castellano et al., 2009] Castellano, C., Fortunato, S., and Loreto, V. (2009). *Rev. Mod. Phys.*, 81:591.

[Castellano et al., 2000] Castellano, C., Marsili, M., and Vespignani, A. (2000). *Phys. Rev. Lett.*, 85:3536–3539.

[Daniška and Gendiar, 2015] Daniška, M. and Gendiar, A. (2015). *J. Phys. A: Math. Theor.*, 48:435002.

[Daniška and Gendiar, 2016] Daniška, M. and Gendiar, A. (2016). *J. Phys. A: Math. Theor.*, 49:145003.

[de Lathauwer et al., 2000] de Lathauwer, L., de Moor, B., and Vandewalle, J. (2000). *SIAM J. Matrix Anal. Appl.*, 21:1324.

[Domb et al., 2001] Domb, C., Green, M. S., and Lebowitz, J., editors (1972–2001). *Phase Transitions and Critical Phenomena*, volume 1–20. Academic, New York.

[Dornic et al., 2001] Dornic, I., Chaté, H., Chave, J., and Hinrichsen, H. (2001). *Phys. Rev. Lett.*, 87:045701.

[Efrati et al., 2014] Efrati, E., Wang, Z., Kolan, A., and Kadanoff, L. P. (2014). *Rev. Mod. Phys.*, 86:647.

[Evenbly, 2015] Evenbly, G. (2015). arXiv:1509.07484.

[Evenbly and Vidal, 2015a] Evenbly, G. and Vidal, G. (2015a). *Phys. Rev. Lett.*, 115:180405.

[Evenbly and Vidal, 2015b] Evenbly, G. and Vidal, G. (2015b). *Phys. Rev. Lett.*, 115:200401.

[Evenbly and Vidal, 2016] Evenbly, G. and Vidal, G. (2016). *Phys. Rev. Lett.*, 116:040401.

[Fisher, 1960] Fisher, M. E. (1960). In *Proc. Roy. Soc. London*, volume 254 of *A*, page 66.

[Fisher, 1974] Fisher, M. E. (1974). *Rev. Mod. Phys.*, 46:597. And references therein.

[Frachebourg and Krapivsky, 1996] Frachebourg, L. and Krapivsky, P. L. (1996). *Phys. Rev.*, 53:R3009.

[Gandica et al., 2013] Gandica, Y., Medina, E., and Bondale, I. (2013). *Physica A*, 392:6561.

[Gefen et al., 1983a] Gefen, Y., Aharony, A., and Mandelbrot, B. B. (1983a). *J. Phys. A: Math. Gen.*, 16:1267–1278.

[Gefen et al., 1984a] Gefen, Y., Aharony, A., and Mandelbrot, B. B. (1984a). *J. Phys. A: Math. Gen.*, 17:1277–1289.

[Gefen et al., 1984b] Gefen, Y., Aharony, A., Shapir, Y., and Mandelbrot, B. B. (1984b). *J. Phys. A*, 17:435.

[Gefen et al., 1980] Gefen, Y., Mandelbrot, B. B., and Aharony, A. (1980). *Phys. Rev. Lett.*, 45:855–858.

[Gefen et al., 1983b] Gefen, Y., Meir, Y., Mandelbrot, B. B., and Aharony, A. (1983b). *Phys. Rev. Lett.*, 50:145–148.

[Gendiar et al., 2014] Gendiar, A., Daniška, M., Krcmar, R., and Nishino, T. (2014). *Phys. Rev. E*, 90:012122.

[Gendiar et al., 2012] Gendiar, A., Krcmar, R., Andergassen, S., Daniška, M., and Nishino, T. (2012). *Phys. Rev. E*, 86:021105.

[Gendiar et al., 2008] Gendiar, A., Krcmar, R., Ueda, K., and Nishino, T. (2008). *Phys. Rev. E*, 77:041123.

[Gendiar and Nishino, 2002] Gendiar, A. and Nishino, T. (2002). *Phys. Rev. E*, 65:046702.

[Genzor, 2016a] Genzor, J. (2016a). CTMRG. Available at `https://github.com/josephinius/CTMRG`.

[Genzor, 2016b] Genzor, J. (2016b). HoTRG. Available at `https://github.com/josephinius/HoTRG`.

[Genzor, 2016c] Genzor, J. (2016c). iTEBD. Available at `https://github.com/josephinius/iTEBD`.

[Genzor et al., 2015] Genzor, J., Bužek, V., and Gendiar, A. (2015). *Physica A*, 420:200.

[Genzor et al.,] Genzor, J., Gendiar, A., and Nishino, T. In preparation.

[Genzor et al., 2016] Genzor, J., Gendiar, A., and Nishino, T. (2016). *Phys. Rev. E*, 93:012141.

[Gonzalez-Avella et al., 2005] Gonzalez-Avella, J. C., Cosenza, M. G., and Tucci, K. (2005). *Phys. Rev. E*, 72:065102.

[Gonzalez-Avella et al., 2006] Gonzalez-Avella, J. C., Eguiluz, V. M., and Cosenza, M. G. (2006). *Phys. Rev. E*, 73:046119.

[Gu and Wen, 2009] Gu, Z. C. and Wen, X. G. (2009). *Phys. Rev. B*, 80:155131.

[Hasegawa et al., 2007] Hasegawa, I., Sakaniwa, Y., and Shima, H. (2007). *Surf. Sci.*, 601:5232.

[Hauru et al., 2015] Hauru, M., Evenbly, G., Ho, W. W., Gaiotto, D., and Vidal, G. (2015). arXiv:1512.03846.

[Holm and Janke, 1996] Holm, C. and Janke, W. (1996). *Phys. Lett. B*, 375:69.

[Ito et al., 1988] Ito, T., Mizuno, K., Ito, K., and Beaudry, B. J. (1988). *J. de Physique*, C8:343.

[Kadanoff, 1966] Kadanoff, L. P. (1966). *Physics*, 2:263.

[Kazakov, 1986] Kazakov, V. A. (1986). *Phys. Lett. A*, 119:140.

[Klemm et al., 2002] Klemm, K., Equíluz, V. M., Toral, R., and Miguel, M. S. (2002). *Phys. Rev. E*, 67:026120.

[Klemm et al., 2003a] Klemm, K., Equíluz, V. M., Toral, R., and Miguel, M. S. (2003a). *Physica A*, 327:1.

[Klemm et al., 2003b] Klemm, K., Equíluz, V. M., Toral, R., and Miguel, M. S. (2003b). *Phys. Rev. E*, 67:045101.

[Klemm et al., 2005] Klemm, K., Equíluz, V. M., Toral, R., and Miguel, M. S. (2005). *J. Ecom. Dynam. Comntrol*, 29:321–334.

[Kosterlitz, 1974] Kosterlitz, J. M. (1974). *J. Phys. C*, 7:1046.

[Kosterlitz and Thouless, 1973] Kosterlitz, J. M. and Thouless, D. J. (1973). *J. Phys. C*, 6:1181.

[Krcmar et al., 2008] Krcmar, R., Gendiar, A., Ueda, K., and Nishino, T. (2008). *J. Phys. A*, 41:125001.

[Krioukov et al., 2010] Krioukov, D., Papadopoulos, F., Kitsak, M., Vahdat, A., and nà, M. B. (2010). *Phys. Rev. E*, 82:036106.

[Krioukov et al., 2009] Krioukov, D., Papadopoulos, F., Vahdat, A., and nà, M. B. (2009). *Phys. Rev. E*, 80:035101.

[Lee and Gendiar,] Lee, Y. and Gendiar, F. V. A. In preparation.

[Liang et al., 2006] Liang, F., Guo, L., Zhong, Q. P., Wen, X. G., Chen, C. P., Zhang, N. N., and Chu, W. G. (2006). *Appl. Phys. Lett.*, 89:103105.

[Luscombe and Desai, 1985] Luscombe, J. H. and Desai, R. C. (1985). *Phys. Rev. B*, 32:1614.

[Maldacena, 1998] Maldacena, J. (1998). *Adv. Theor. Math. Phys.*, 2:231.

[Maldacena, 1999] Maldacena, J. (1999). *Int. J. Theor. Phys.*, 38:1113.

[Mattis and Pan, 1988] Mattis, D. C. and Pan, C. Y. (1988). *Phys. Rev. Lett.*, 61:463. And references therein.

[Mosseri and Sadoc, 1982] Mosseri, R. and Sadoc, J. F. (1982). *J. Physique - Lettres*, 43:L249.

[Moura-Melo et al., 2007] Moura-Melo, W. A., Pereira, A. R., Mol, L. A. S., and Pires, A. S. T. (2007). *Phys. Lett. A*, 360:472.

[Nishino and Okunishi, 1996] Nishino, T. and Okunishi, K. (1996). *J. Phys. Soc. Jpn.*, 65:891.

[Nishino and Okunishi, 1997] Nishino, T. and Okunishi, K. (1997). *J. Phys. Soc. Jpn.*, 66:3040.

[Onsager, 1944] Onsager, L. (1944). *Phys. Rev.*, 65:117.

[Radillo-Díaz et al., 2009] Radillo-Díaz, A., Pérez, L. A., and del Castillo-Mussot, M. (2009). *Phys. Rev. E*, 80:066107.

[Ryu and Takayanagi, 2006] Ryu, S. and Takayanagi, T. (2006). *Phys. Rev. Lett.*, 96:181602.

[Sakaniwa and Shim, 2009] Sakaniwa, Y. and Shim, H. (2009). *Phys. Rev. E*, 80:021103.

[Sakon et al., 2013] Sakon, T., Nagashio, H., Sasaki, K., Susuga, S., Numakura, D., Abe, M., Endo, K., Yamashita, S., Nojiri, H., and Kanomata, T. (2013). *InTech*.

[Schollwöck, 2005] Schollwöck, U. (2005). *Rev. Mod. Phys.*, 77:259.

[Serina et al., 2016] Serina, M., Genzor, J., Lee, Y., and Gendiar, A. (2016). *Phys. Rev. E*, 93:042123.

[Shima and Sakaniwa, 2006a] Shima, H. and Sakaniwa, Y. (2006a). *J. Stat. Mech.*, page P08017.

[Shima and Sakaniwa, 2006b] Shima, H. and Sakaniwa, Y. (2006b). *J. Phys. A: Math. Gen.*, 39:4921.

[Stanley, 1971] Stanley, H. E. (1971). *Introduction to Phase Transitions and Critical Phenomena*. Oxford University Press, Oxford, U.K.

[Stošić et al., 1996] Stošić, T., Stošić, B. D., Milošević, S., and Stanley, H. E. (1996). *Physica A*, 233:31.

[Tobochnik, 1982] Tobochnik, J. (1982). *Phys. Rev. B*, 26:6201.

[Toral and Tessone, 2007] Toral, R. and Tessone, C. J. (2007). *Commun. Comput. Phys.*, 2:177.

[Ueda et al., 2014] Ueda, H., Okunishi, K., and Nishino, T. (2014). *Phys. Rev. B*, 89:075116.

[Ueda et al., 2007] Ueda, K., Krcmar, R., Gendiar, A., and Nishino, T. (2007). *J. Phys. Soc. Jpn*, 76:084004.

[Vezzani, 2003] Vezzani, A. (2003). *J. Phys. A: Mathe. Gen.*, 36:1593.

[Vidal, 2007] Vidal, G. (2007). *Phys. Rev. Lett.*, 98:070201.

[Voigt et al., 2001] Voigt, A., Richter, J., and Tomczak, P. (2001). *Physica A*, 299:461.

[Voigt et al., 2004] Voigt, A., Wenzel, W., Richter, J., and Tomczak, P. (2004). *Eur. Phys. J. B*, 38:49.

[Šamaj, 2010] Šamaj, L. (2010). *Acta Physica Slovaca*, 60:155–257. And references therein.

[Wang et al., 2013a] Wang, C., Qin, S.-M., and Zhou, H.-J. (2013a). arXiv:1311.6577.

[Wang et al., 2013b] Wang, M., Ran, S. J., Liu, T., Zhao, Y., Zheng, Q. R., and Su, G. (2013b). arXiv:1311.1502.

[White, 1992] White, S. R. (1992). *Phys. Rev. Lett.*, 69:2863.

[Wilson and Kogut, 1974] Wilson, K. G. and Kogut, J. (1974). *Phys. Rep.*, 12:75.

[Wu, 1982] Wu, F. W. (1982). *Rev. Mod. Phys.*, 54:235.

[Xie et al., 2012] Xie, Z. Y., Chen, J., Qin, M. P., Zhu, J. W., Yang, L. P., and Xiang, T. (2012). *Phys. Rev. B*, 86:045139.

[Yang et al., 2015] Yang, S., Gu, Z. C., and Wen, X. G. (2015). arXiv:1512.04938.

[Yeomans, 1992] Yeomans, J. M. (1992). *Statistical mechanics of phase transitions*. Oxford University Press, New York.

[Yoshikawa et al., 2004] Yoshikawa, H., Hayashida, K., Kozuka, Y., Horiguchi, A., and Agawa, K. (2004). *Appl. Phys. Lett.*, 85:5287.

[Zinn-Justin, 1996] Zinn-Justin, J. (1996). *Quantum Field Theory and Critical Phenomena*. Oxford University Press, Oxford, U.K.